Comparison of optical trapping between gold and silver nanostructures

by

Layla Haddad
Bachelor of Arts and Sciences, Quest University, 2020

A Thesis Submitted in Partial Fulfillment of the
Requirements for the Degree of

MASTER OF SCIENCE

in the Department of Physics and Astronomy

Comparison of optical trapping between gold and silver nanostructures

by

Layla Haddad
Bachelor of Arts and Sciences, Quest University, 2020

Supervisory Committee

Dr. Reuven Gordon, Supervisor
(Department of Physics and Astronomy)

Dr. Alexandre G. Brolo, Departmental Member
(Department of Physics and Astronomy)

Dr. Arthur Blackburn, Departmental Member
(Department of Physics and Astronomy)

Abstract

This thesis explores the optical trapping capabilities of silver (Ag) and gold (Au) nanostructures. Double nanohole (DNH) apertures with a gap size of ≈ 32 nm were fabricated in each nanostructure to trap 20 nm polystyrene (PS) nanospheres. The surfaces of each metal were either modified using an aqueous solution of 5 mM monodisperse thiol polyethylene glycol (mPEG) (the "experiment" group), or immersed in deionized (DI) water only (the "control" group). A solution containing the PS nanospheres was then transferred and confined to a chamber spacer attached to the modified surface (for the "experiment" group) or the unmodified surface (for the "control" group). To evaluate the trapping performance of each group, the trapped data was acquired as a function of time. The power spectrum density (PSD) of the trapping signal was analyzed using the Brownian motion theory of trapped beads, and the data was fitted with a Lorentzian function to extract the corner frequency and time constant. The trap stiffness (force constant) of the optical trap was also determined.

The results indicated that increasing the trapping power led to higher trap stiffness for silver DNHs compared to gold in the DI water environment, suggesting a stronger force holding the nanoparticles in the trap. The surrounding medium significantly impacted the trapping performance, with the mPEG-thiol monolayer reducing the trap stiffness for both silver and gold DNHs. Additionally, a linear dependence of trap stiffness and time constant on laser power was observed, confirming that increasing power enhances trapping strength and reduces the time for the nanoparticle to fall into the trap. This research provides nuanced insights into the comparative effectiveness of silver and gold nanostructures in optical trapping and demonstrates the influence of the surrounding medium on trapping performance. These results provide pathways for future advancements in aperture-based trapping.

Table of Contents

List of Tables

List of Figures

Acknowledgements

I would like to thank: my supervisor and supervisory committee (Reuven Gordon, Alexandre Brolo, and Arthur Blackburn) for their support, encouragement and feedback. The Centre for Advanced Materials and Related Technology (CAMTEC), for providing me with training (SEM, sputtering deposition, plasma cleaners, etc). Special thanks to Dr. Elaine Humphrey and Andrew MacDonald. The staff at the Graduate Student's Society (GSS) and the Grad House Restaurant for feeding and caffeinating me throughout my degree. My friends (Shoshannah, Charlie, Maheyer, Caleb, Omar, Jono, Bryn, Sanker, Anne, Josh) and the HEP tea folks for their feedback and time.

Last but not least thanks to not my cat (Scout), not my dog (Exa), and to Star Trek for supporting me in the low moments.

"I canna' change the laws of physics, Captain!"
Scotty, Chief Engineer in STAR TREK.

Dedication

To all the dogs and cats in my neighborhood that made my day worthwhile!

Chapter 1

Introduction

1.1 Principles of Optical Trapping

In 1967, Arthur Ashkin hypothesized that atoms and molecules could be accelerated and trapped using laser light tuned to specific optical transitions. He demonstrated that micron-sized particles could be accelerated and held in stable optical traps solely through the radiation pressure from a continuous laser [1].

In subsequent experiments [2–4], Ashkin discovered that radiation pressure comprises two fundamental force components affecting the particle. One is the longitudinal component, known as the scattering force which acts along the direction of the beam, while the other is the transverse component, called the gradient force, acts in the direction of the beam's intensity gradient.

Later, in 1986, Ashkin demonstrated for the first time the optical trapping of dielectric particles using a single-beam gradient force trap [5]. This allowed the use of the new traps extending the size range of macroscopic particles accessible to optical trapping and manipulation well into the full spectrum of Mie and Rayleigh particles.

Figure 1.1 shows the radiation pressure acting on a colloidal particle in an electromagnetic field resulting in gradient and scattering forces.

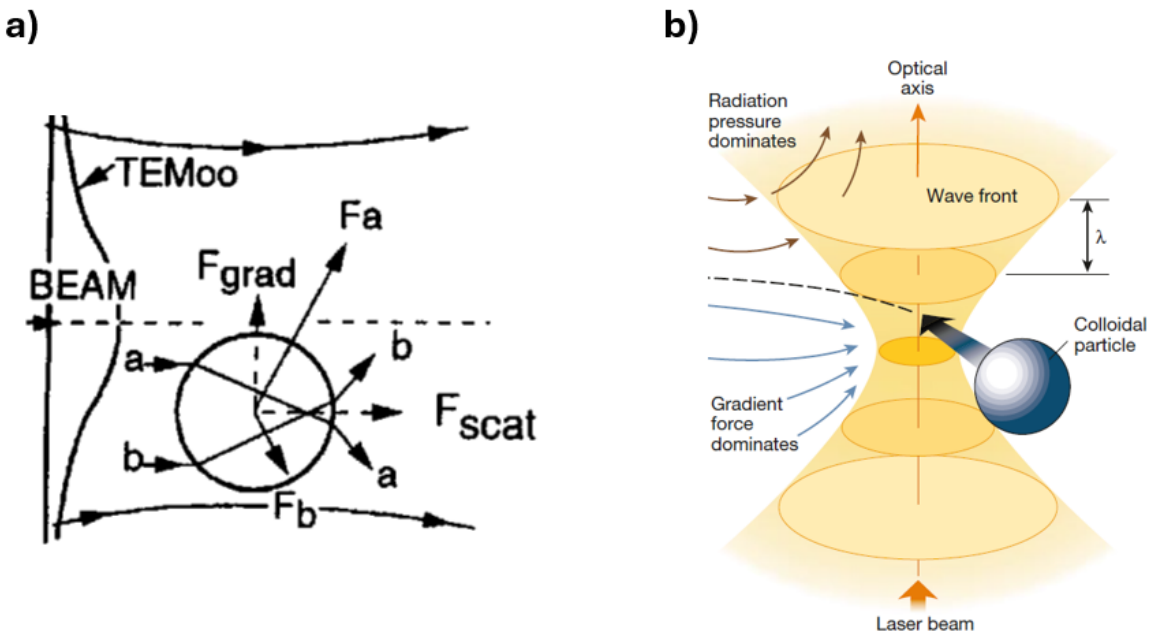

Figure 1.1: (a) The gradient and scattering forces acting on a dielectric particle displaced from the centre of a Gaussian laser beam. The curved lines at the top and bottom illustrate the shape of the laser beam, while the Gaussian curve represents the intensity profile. Two light rays from the laser beam, labeled a and b, show how the refraction of light by the particle alters the photons' momentum, leading to the forces F_a and F_b. Reproduced from reference [6]. (b) Conventional optical tweezers use a strong focused beam of light to trap atoms or nanoparticles. The intensity gradient draws the particle toward the focus, whereas the radiation pressure from the beam pushes the particle along the optical axis. The stronger gradient forces compared to the scattering forces from radiation pressure lead to the creation of a stable three-dimensional trap. Reproduced from reference [7].

This thesis focuses on Rayleigh particles. When the diameter of a trapped particle is much smaller than the wavelength of light, the conditions for Rayleigh scattering ($r \ll \lambda$) are met, and the particle can be approximated as a point dipole within an inhomogeneous electromagnetic field [5, 8]. The dipole moment is defined as [9]

$$\mathbf{p} = \alpha \mathbf{E} \tag{1.1}$$

where $\mathbf{p}$ is the dipole moment, $\mathbf{E}$ is the electric field, and α is the particle's polarizability.

The force exerted on a single charge within an electromagnetic field is the Lorentz force.

$$F = (\mathbf{p} \cdot \Delta)\mathbf{E} + \frac{d\mathbf{p}}{d\mathbf{t}} \times \mathbf{B}, \tag{1.2}$$

where $\mathbf{F}$ is the force, $\mathbf{E}$ is the electric field, $\mathbf{B}$ is the magnetic field, and $\mathbf{p}$ is the dipole moment.

Assuming a spherical particle with radius r, refractive index n_p and background medium n_m. The polarizability α can be written as

$$\alpha = \left(\frac{n_b^2 - n_m^2}{n_p^2 + 2n_m^2} \right) n_m^2 r^3 \tag{1.3}$$

The gradient force F_{grad} acting on a particle in the Rayleigh regime depends on its polarizability as well as the gradient of the electromagnetic field intensity

$$F_{\text{grad}} = \frac{1}{2} \alpha \Delta E^2 \tag{1.4}$$

where E^2 indicates the intensity of the photons from the laser, meaning that the strongest force will be at the location of highest photon intensity, which is at the beam's focal point. Consequently, the particle is drawn toward the center of the beam.

Substitute for α in Equation 1.4,

$$F_{\text{grad}} = -\frac{n_b}{2} \alpha \Delta E^2 = -\frac{n_b^3 r^3}{2} \left(\frac{n_m^2 - 1}{n_m^2 - 2} \right) \Delta E^2 \tag{1.5}$$

Therefore, the gradient force scales as the third power of the particles size

$$|\mathbf{F}_{\text{grad}}| \propto r^3 \tag{1.6}$$

The scattering force F_{scat} arising from the dipole moment of the particle and acts in the direction of the incident radiation. For a Rayleigh particle in a medium of index n_b, the scattering force in the direction of the incident power is

$$F_{\text{scat}} = \frac{n_b P_{\text{scat}}}{c}, \tag{1.7}$$

where P_{scat} is the power scattered. The beam intensity is

$$I = \frac{n_m c}{2} |E|^2 \tag{1.8}$$

The optical power scattered by the particle can be approximated by the radiation of an electric dipole [10] by

$$P_{\text{scat}} = \frac{16}{3} \frac{\pi^4 c}{\lambda^4} |\mathbf{p}|^2 \tag{1.9}$$

In terms of intensity I_0 and effective index n_m, the scattering force can be re-written as

$$F_{\text{scat}} = \frac{I_0}{c}\frac{128\pi^5 r^6}{3\lambda^4}\left(\frac{n_m^2-1}{n_m^2+2}\right)^2 n_b \tag{1.10}$$

Hence, the scattering force scales directly as the ratio of the sixth power of the particles size to the fourth power of the wavelength

$$|\mathbf{F}_{\text{scat}}| \propto \frac{r^6}{\lambda^4} \tag{1.11}$$

For a Gaussian beam of focal spot size w_0 that occurs at an axial position $z = \pi w_0^2/\sqrt{3}\lambda$,

$$R = \frac{F_{\text{grad}}}{F_{\text{scat}}} = \frac{3\sqrt{3}}{64\pi^5}\frac{n_b^2}{\left(\frac{n_m^2-1}{n_m^2+2}\right)}\frac{\lambda^5}{r^3\omega_0^2} \geq 1 \tag{1.12}$$

where λ is the wavelength in the medium. This condition applies only in the Rayleigh regime where the particle diameter is less than the wavelength of light, $2r \leq \lambda$ [5].

Ashkin was awarded a Noble Prize in Physics for his invention of "optical tweezers" (2018) and its application to manipulate atoms, molecules, and biological cells.

1.2 Nanoaperture Optical Trapping

Particles suspended in fluid experience random Brownian motion, resulting in high thermal kinetic energy of the particle [11]. To create a stable trap, the potential well of the trapping force should be significantly stronger than the kinetic energy of the particle. The potential energy is given by [12, 13]

$$U \gg k_B T \tag{1.13}$$

where k_B is the Boltzmann constant and T is the temperature. The trapping potential of a dielectric sphere in an electromagnetic field is expressed as [14]

$$U = -p \cdot E = \frac{2\pi n_m r^3 \left(\frac{n_p}{n_m}\right)^2 - 1}{c\left(\frac{n_p}{n_m}\right)^2 + 2} I_0 \tag{1.14}$$

Equation 1.14 reveals a key limitation of using optical tweezers lies in the third power dependence of the trapping potential. When the particle is one order of magnitude smaller, the beam intensity must be increased by three orders of magnitudes. Hence, stable trapping requires higher powers which could result in damaging particles and biological cells.

1.2.1 Bethe's Theory

In 1944, Hans Bethe studied the diffraction of electromagnetic waves by a small hole in an infinite conducting screen [15]. Figure 1.2 shows two cavities α and β coupled by a small hole.

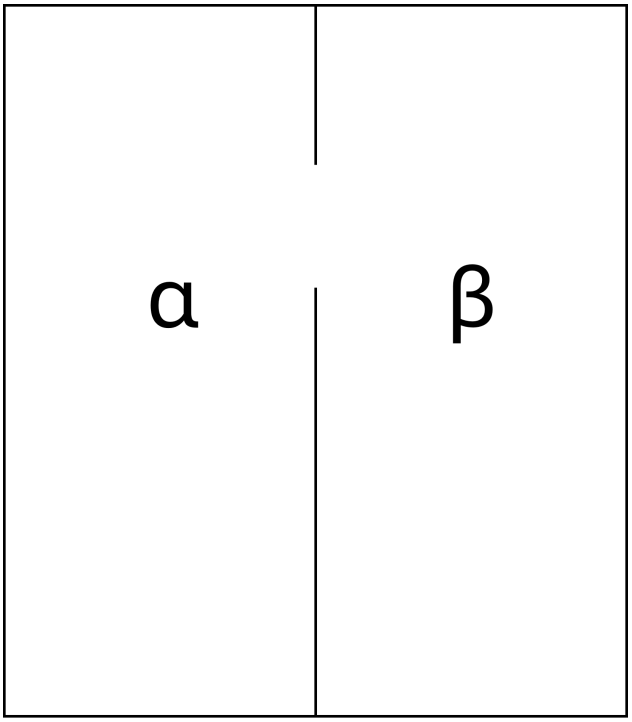

Figure 1.2: Two cavities α and β coupled by a small hole

When light propagates through an aperture that is significantly smaller than its wavelength, the light gets cut-off at the edges. The wave cannot meet the boundary condition requiring the electric field to be zero at the aperture's edges, resulting in diffraction of the light.

Bethe used a quasi-static approximation of Maxwell's equations. It involved a plane wave striking a circular aperture with a diameter smaller than the wavelength, within an infinitely thin, perfect electric conductor film. The plane wave strikes the film perpendicularly, with its electric and magnetic fields aligned parallel to the film's surface. The light that emerges through the circular aperture is approximated as originating from a magnetic dipole. This can be extended for nanoaperture trapping, where the light transmitted through a subwavelength circular aperture can be approximated by emission from a magnetic dipole [10]. The optical transmission is approximated as

$$T = \frac{1}{2}\left(\frac{4Z_0\pi^3}{3\lambda_0^4}\right)\left(\frac{8r^3}{3}H_0\right)^2 \propto \frac{r^6}{\lambda^4} \tag{1.15}$$

where Z_0 is the free-space impedance, λ_0 is the wavelength in free-space, r is the radius of the hole, and H_0 is the magnetic field of the incident wave.

As shown in Figure 1.3, when normalizing based on the area of a circular aperture ($A = \pi r^2$), the transmittance through a subwavelength circular aperture is inversely proportional to the fourth power of the wavelength $\frac{T}{A} \propto \frac{r^4}{\lambda^4}$. If the aperture is enclosed by a dielectric medium with a refractive index n, the wavelength in the medium adjusts to $\lambda = \frac{\lambda_0}{n}$. Consequently, for a given aperture size, a higher optical transmission is anticipated,

$$T \propto \frac{1}{\lambda^4} \propto \frac{n^4}{\lambda_0^4} \tag{1.16}$$

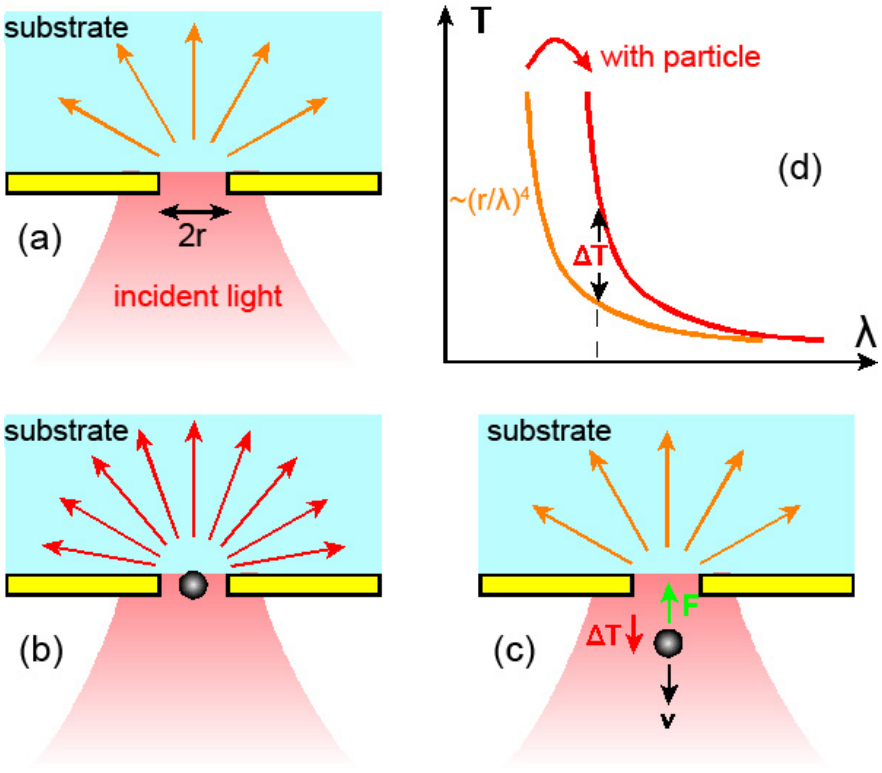

Figure 1.3: Optical transmission through subwavelength aperture: a) without a particle; b) enhanced transmission due to the presence of a dielectric particle; c) if the particle exits the aperture, the reduction in light momentum (ΔT) generates a force (F) that pulls the particle back into the aperture, known as self-induced back action; (d) redshift in the transmission curve caused by the particle entering the aperture, resulting in a change in transmission ΔT. Reproduced from reference [16].

1.2.2 Self-Induced Back-Action

Figure 1.3a illustrates the optical transmission through the circular aperture, which is primarily characterized by light diffraction and exhibits low power. Figure 1.3b shows the situation when a particle enters the trap. The particle has a higher refractive index compared to the medium (water) inside the aperture. This causes dielectric loading (see Equation 1.16), where a substantial increase in optical transmission attributable exclusively to the change in refractive index within the same aperture.

Figure 1.3c presents the scenario where the particle attempts to escape from the aperture. In this case, the transmission through the aperture decreases due to the shift in refractive index. As per Newton's third law, the net momentum of the light alters, leading to an equal and opposite change in momentum. This creates an optical force that pulls the particle back towards the aperture, effectively trapping it. This effect is referred to as the self-induced back-action (SIBA).

1.3 Plasmonics

Plasmonics involves exciting surface plasmons (SPs), which are collective oscillations of free electrons at the boundary between metals and dielectric materials [17]. This phenomenon allows the confinement of electromagnetic fields at the metal's surface, facilitating the manipulation of light beyond its diffraction limit $(\frac{\lambda_0}{2n})^3$, where $n = \sqrt{\epsilon}$ is the refractive index of the surrounding medium [17, 18].

Figure 1.4 shows a sketch of a homogeneous sphere placed into an electrostatic field. The spherical particle with radius a is located at the origin in a uniform static electric field $\mathbf{E} = E_0\hat{\mathbf{z}}$. The surrounding medium is isotropic and non-absorbing with a dielectric constant ϵ_m (e.g. air or water). The field lines are parallel to the z-direction. The dielectric response of the sphere is characterized by the dielectric function of the metal $\epsilon(\omega)$ which is frequency dependent expressed by $\epsilon(\omega) = \epsilon_1(\omega) + i\epsilon_2(\omega)$.

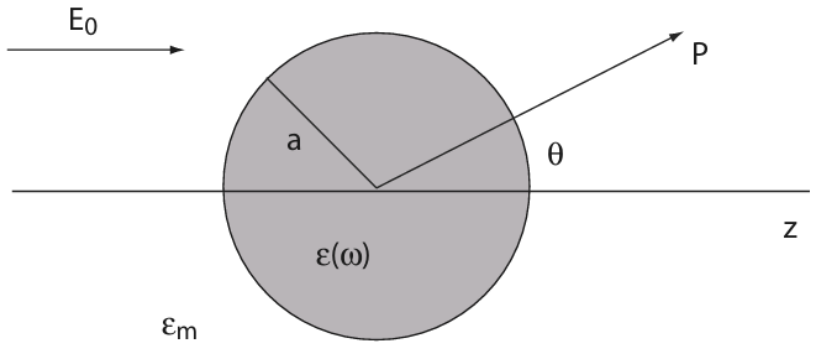

Figure 1.4: Sketch of a homogeneous sphere placed into an electrostatic field. Reproduced from reference [18].

In this case, the particle is smaller than the wavelength of light $a << \lambda$, and the phase of the harmonically oscillating electromagnetic field is constant over the particle's volume. Using a simple quasi-static approximation of the Laplace equation ($\phi = 0$) and solving $E = -\nabla\phi$, the electric field inside and outside the particle is given by [18]

$$\mathbf{E}_{in} = \frac{3\epsilon_m}{\epsilon + 2\epsilon_m} E_0 \tag{1.17}$$

$$\mathbf{E}_{out} = \mathbf{E}_0 + \frac{3\mathbf{n}(\mathbf{n}\cdot\mathbf{p}) - \mathbf{p}}{4\pi\epsilon_0\epsilon_m} \frac{1}{r^3} \tag{1.18}$$

$$\mathbf{p} = 4\pi\epsilon_0\epsilon_m a^3 \frac{\epsilon - \epsilon_m}{\epsilon + 2\epsilon_m} \mathbf{E}_0 \tag{1.19}$$

The applied field induced a dipole moment $\mathbf{p}$ inside the sphere of magnitude proportional to $|\mathbf{E}_0|$. The polarizability α defined via $\mathbf{p} = \epsilon_0\epsilon_m\alpha\mathbf{E}_0$ is,

$$\alpha = 4\pi a^3 \frac{\epsilon - \epsilon_m}{\epsilon + 2\epsilon_m} \tag{1.20}$$

From Equation 1.20, it is evident that the polarizability reaches its maximum when the denominator, $|\epsilon + 2\epsilon_m|$, is minimized. Under these conditions, the particle undergoes field enhancement, known as a localized surface plasmon resonance (LSPR). This phenomenon is shown in Figure 1.5. Structures that support LSPRs exhibit a uniform E_0 when illuminated by light due to their dimensions being significantly smaller than the wavelength of light. In the case of small or slowly varying Im[ϵ] around the resonance simplifies to the Fröhlich condition given by Equation 1.21 [18],

$$\mathrm{Re}[\epsilon(\omega_{\mathrm{sp}})] = -2\epsilon_m \tag{1.21}$$

Here, $\epsilon(\omega)$ is the dielectric function of the metal, and ϵ_m the dielectric constant of the insulating host. Equation 1.21 defines the plasmon frequency ω_{sp} for a spherical nanoparticle in a dielectric medium. At this frequency, surface plasmons are most effectively excited, leading to significant field enhancement and resonance effects observed in LSPR. This condition is essential for applications that utilize the enhanced local fields generated by surface plasmons, such as in sensing, optical trapping and imaging technologies.

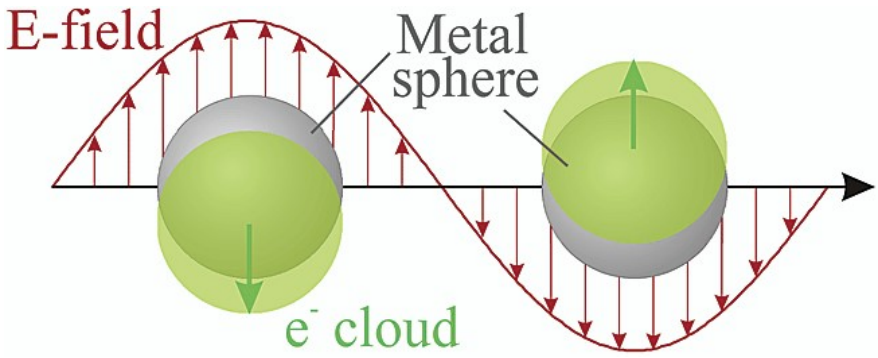

Figure 1.5: Schematic of plasmon oscillation for a sphere, showing the displacement of the conduction electron charge cloud relative to the nuclei. Reproduced from reference [19].

For LSPR, the quality factor Q is given by [20, 21]

$$Q = \frac{\omega(d\epsilon'/d\omega)}{2(\epsilon''(\omega))^2} \tag{1.22}$$

where $\epsilon' = \mathrm{Re}(\epsilon)$ and $\epsilon'' = \mathrm{Im}(\epsilon)$. Thus, Q is larger when $\mathrm{Im}(\epsilon)$ is small which characterises the strength (or damping) and width of the resonance.

1.4 Plasmonic Double Nanohole Optical Trapping

When electromagnetic radiation interacts with a sub-wavelength aperture in a real metal film, it induces coherent, localized oscillations of electron charges, known as localized surface plasmons (LSPs) [22]. This leads to a strong field gradient concentrated within the aperture [23]. A pronounced field gradient within an area smaller than the diffraction limit is ideal for trapping very small particles ($\leq$ 100 nm), thereby minimizing the need for increased optical power [24, 25].

Previously, it has been observed that circular nanohole optical traps generate a larger

optical force than perturbative optical traps [26,27]. Optical trapping with plasmonic double nanohole (DNH) apertures offers more advantages, such as increased cut-off wavelength [28, 29], increased transmission [30], and local field enhancement [31–33].

Figure 1.6 shows the simulated Finite-Difference Time-Domain (FDTD) electric field distribution at the gap of a DNH aperture.

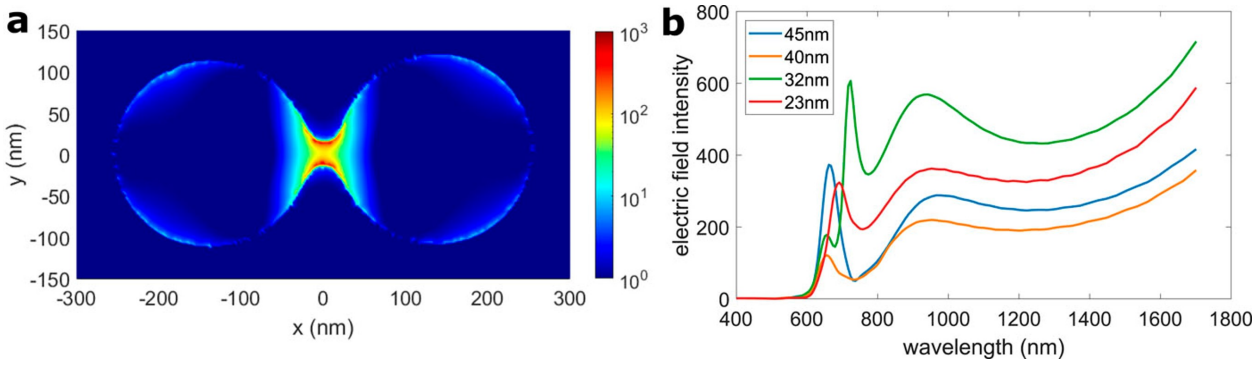

Figure 1.6: FDTD simulation results for electric field intensity: b) visualization of a DNH with a 32 nm gap separation; b) electric field intensity for DNHs with gap separations of 22.7, 32, 40, and 45 nm, normalized to the incident intensity. Reproduced from reference [34].

In this thesis, I fabricated the DNH structure using colloidal lithography following on the method of previous group members [35], and further discussed in Chapter 2.1. The DNH structure is illustrated in Figure 1.7, which has two sharp tips separated by a tiny gap. The geometry of the DNH is characterized by the metal thickness T, the diameter of the circular apertures D, the center-to-center separation distance L, as well as the curvature C and width W of the gap.

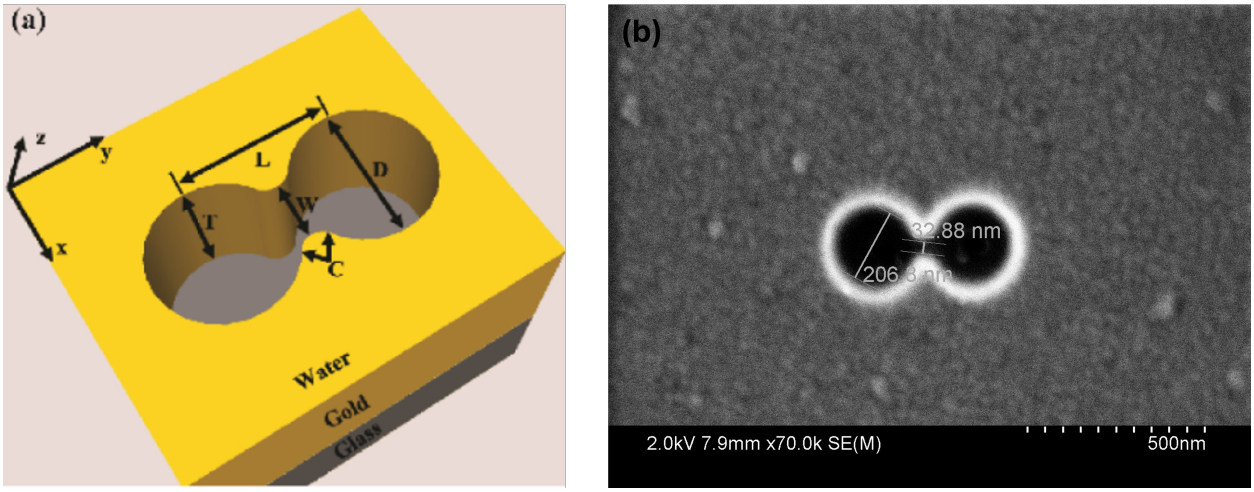

Figure 1.7: Structure of the double nanohole (DNH) for trapping: a) Schematic view of the DNH structure in a metal film. Reproduced from reference [36]; b) Scanning electron microscope (SEM) image of a DNH fabricated in this thesis with $T = 70$ nm, $D = 206.8$ nm, $W = 32.88$ nm, and $L = 239.68$ nm.

1.5 Brownian Motion of Trapped Beads

The Einstein-Ornstein-Uhlenbeck theory outlines the Brownian motion of a spherical bead trapped in a harmonic potential, using three uncoupled Langevin equations—one for each Cartesian coordinate of the bead (x(t), y(t), z(t)) [37,38]. For the x-coordinate, the equation is given by:

$$m\ddot{x}(t) + \gamma_0\dot{x}(t) + \kappa x(t) = \sqrt{2k_BT\gamma_0}\,\eta(t). \tag{1.23}$$

Here, m is the bead's mass, γ_0 is the friction coefficient given by Stokes' law for a spherical particle of diameter R

$$\gamma_0 = 6\pi\rho v R \tag{1.24}$$

where ρv is the liquid's shear viscosity, ρ is the liquid's density, and v is the kinematic viscosity. A correction to the Stokes drag using Faxén's law is used to account for the close proximity between the particle and the wall of the DNH [39, 40]. For a motion parallel to the wall, Equation 1.24 becomes,

$$\gamma = \frac{6\pi\mu r}{[1 - \frac{9}{16}(\frac{r}{h}) + \frac{1}{8}(\frac{r}{h})^3 - \frac{45}{256}(\frac{r}{h})^4 - \frac{1}{16}(\frac{r}{h})^5]} \tag{1.25}$$

where μ the is the dynamic viscosity of the medium which is water given by $\mu = 1.0 \times 10^{-3}$ Ns/m^2 at room temperature, r is the radius of the spherical particle, and h is the

distance from the centre of the particle to the wall. In this work, the spherical particle is a polystyrene (PS) nanosphere with diameter of 20 nm (hence, $r = 10$ nm). Assuming h is 15 nm, solving for γ yields $\gamma = 3.045 \times 10^{-10}$ Ns/m.

The term $-\kappa x(t)$ from Equation 1.23 denotes the harmonic force exerted by the trap, where κ is the force constant or the trap stiffness of the optical trap.

The random thermal forces from the surrounding liquid are modeled by the term $\sqrt{2k_BT\gamma_0}\,\eta(t)$, where $\sqrt{2k_BT\gamma_0}$ is the amplitude of the white-noise random process $\eta(t)$ at absolute temperature T and k_B is the Boltzman constant. The stochastic Gaussian process $\eta(t)$ has a zero mean and a delta function as its auto-correlation function $\langle\eta(t)\rangle = 0$, $\langle\eta(t)\eta(t')\rangle = \delta(t - t')$.

The characteristic time for loss of kinetic energy through friction is $t_{\text{inert}} \equiv m/\gamma_0$, which is shorter than the experimental time resolution at 100 kHz sampling rate. Consequently, the inertial term in Equation 1.23 can be neglected, resulting in:

$$\dot{x}(t) + 2\pi f_c x(t) = (2D)^{1/2}\eta(t). \tag{1.26}$$

where $f_c \equiv \kappa/(2\pi\gamma_0)$ is the corner frequency and $D = k_BT/\gamma_0$ is the diffusion coefficient.

Acquiring a series of the bead position $x(t)$ for a total duration of measurement T_{msr}, and performing a Fourier transform on $x(t)$ and $\eta(t)$ gives:

$$\tilde{x}_k = \int_{-T_{\text{msr}}/2}^{T_{\text{msr}}/2} e^{i2\pi f_k t} x(t)\, dt, \tag{1.27}$$

where $f_k = \frac{k}{T_{\text{msr}}}$ and k is an integer.

The path as a function of noise is given by

$$\tilde{x}_k = \frac{(2D)^{1/2}\tilde{\eta_k}}{2\pi(f_c - if_k)} \tag{1.28}$$

Since the power spectral density (PSD) in Equation 1.30 is a smooth function and does not exhibit any spikes or sudden fluctuations, the leakage term $\dot{x}(t)$ is negligible [37].

Given that the stochastic process $\eta(t)$ has a zero mean, it follows that $\langle\tilde{\eta_k}\rangle = 0$; $\langle\tilde{\eta}_k^*\tilde{\eta_l}\rangle = T_{\text{msr}}\delta_{k,l}$; $\langle|\tilde{\eta}_k|^4\rangle = 2T_{\text{msr}}^2$ This uncorrelated Gaussian process $\eta(t)$ has $(\text{Re }\tilde{\eta_k})_{k=0,1,\ldots}$ and $(\text{Im }\tilde{\eta_k})_{k=0,1,\ldots}$ as uncorrelated random variables with Gaussian distribution. Consequently, $(|\tilde{\eta_k}|^2)_{k=1,2,\ldots}$ are uncorrelated non-negative random variables with exponential distribution. Thus, the experimental values for the power spectrum across different frequencies in the

Brownian motion for $k > 0$ is given by

$$P^{(\mathrm{ex})} \equiv |\tilde{x}_k|^2/T_{msr} = \frac{D/(2\pi^2 T_{msr}|\tilde{x}_k|^2)}{f_c^2 + f_k^2} \tag{1.29}$$

where $P^{(\mathrm{ex})}$ denotes the experimental power spectral values.

The expected value is a Lorentzian given by:

$$P_k \equiv \langle P^{(\mathrm{ex})} \rangle = \frac{D/(2\pi^2)}{f_c^2 + f_k^2} \tag{1.30}$$

Since $P^{(\mathrm{ex})}$ is exponentially distributed, the root-mean square-deviation is equal to its mean:

$$\sigma(P^{(\mathrm{ex})}) = \langle (P^{(\mathrm{ex})} - P_x)^2 \rangle^{1/2} = P_k \tag{1.31}$$

Therefore, two key values that define the dynamics of the laser tweezers, the corner frequency (f_c) and diffusion coefficient (D) which can be found by fitting a Lorentzian to the power spectrum of the bead position $x(t)$. Once f_c is known, one can substitute into $f_c \equiv \kappa/(2\pi\gamma_0)$ and solve for κ to measure the trap stiffness. Additionally, the time constant τ can be calculated from the corner frequency obtained from the PSD by the relation $\tau = \frac{1}{2\pi f_c}$. This time constant describes the duration it takes for the particle to fall into the potential wall as opposed to the viscous drag. Section 3.1 will discuss the analysis of the trapped data obtained from the optical tweezer setup.

1.6 Properties of Gold and Silver

Gold (Au) and silver (Ag) are among the most used metals for plasmonic studies, in the visible and near-infrared (NIR) regions due to their unique optical and thermal properties [18]. Both metals exhibit localized surface plasmon resonance (LSPR) because of their large negative real dielectric constant and small imaginary dielectric constant.

Gold has been the most used for optical trapping because of its good chemical stability and biocompatibility [41]. However, Ag offers better results in terms of sensitivity and exhibits a stronger LSPR across the spectrum from 300 nm to 1200 nm [21, 41]. As shown in Figure 1.8, the quality factor of Ag is also the highest among all noble metals in this range [21].

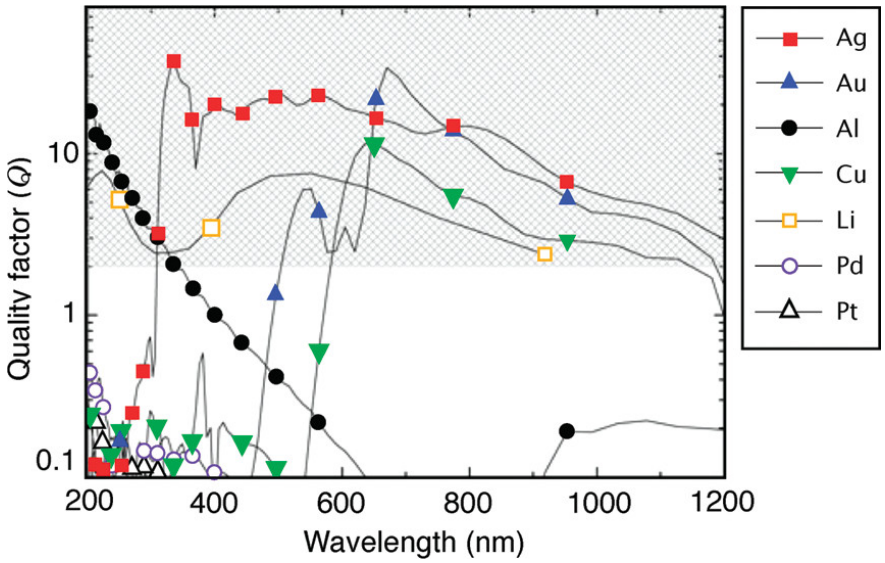

Figure 1.8: The quality factor (Q) of the LSPR at a metal/air interface. A higher Q indicates lower damping and a more pronounced plasmon resonance. The shaded area denotes the range of interest for many plasmonic applications. Reproduced from reference [21].

Interband transitions involving the excitation of electrons from the conduction band to higher energy states, contribute to the damping of surface plasmon (SP) modes [21]. These transitions generally occur at frequencies well above those of localized surface plasmon resonances (LSPRs), as observed with Ag. In contrast, for Au, these transitions restrict LSPR excitation to wavelengths longer than 500 nm.

Figure 1.9 shows a plot of the real ϵ_r and imaginary ϵ_i part of the dielectric function for Ag, Au, and silicon (Si) as a function of wavelength. It is apparent from the plot that Si has large positive values for ϵ_r, and Au is lossier and has a weaker plasmon than Ag because ϵ_i is closer to zero in Ag.

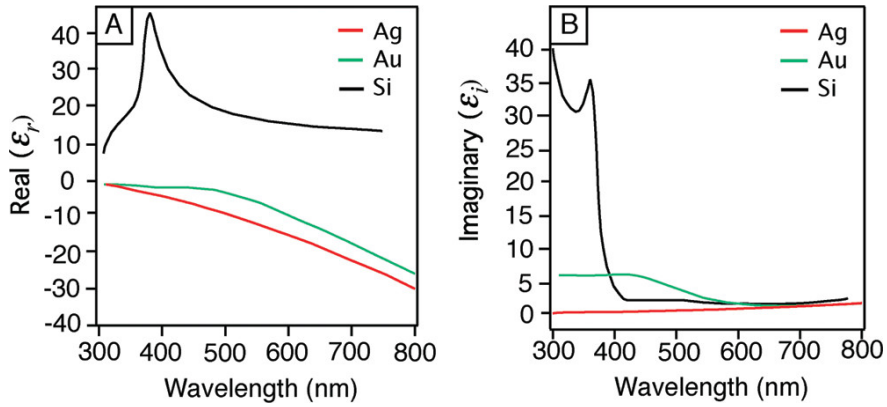

Figure 1.9: A plot showing (A) the real part, ϵ_r, and (B) the imaginary part, ϵ_i, of the dielectric function for Ag, Au, and Si across different wavelengths. Reproduced from reference [21].

Silver possesses the highest electrical and thermal conductivity of all metals, making it an optimal choice for electrical interconnections [21]. However, when exposed to air, Ag reacts with sulfur forming a silver sulfide film on its surface which is typically transparent to visible light. A thin film of silver sulfide can form within a day and may grow to a thickness of 60 Å over the course of a month.

While Au is most commonly used for biosensing because of its oxide-free surface, Ag is mainly used in plasmonic applications outside the human body, such as in plasmonic antennas and circuits for light concentration and guidance [42–45]. In these applications, Ag nanostructures have consistently shown superior performance compared to those made from Au. Previously, in our group we have only used Au for optical trapping [33,35,36,46,47]. This thesis will investigate the optical trapping capabilities of both Au and Ag nanostructures.

1.7 Thiol-Based Self-Assembled Monolayers

Self-assembled monolayers (SAMs) are a class of organic molecules that spontaneously form well-ordered, two-dimensional structures on a substrate [48]. Thiol-based SAMs were used in this thesis because they are the most well studied SAMs to date [49, 50]. The primary driving force for the formation of SAMs is the chemical affinity between the adsorbates and the substrate [48, 51]. A SAM consists of a head group, tail and functional end group. The SAM structure is shown in Figure 1.10.

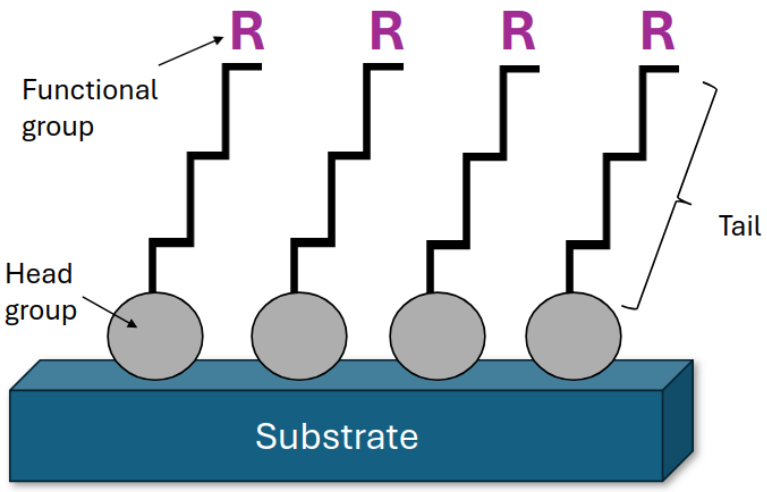

Figure 1.10: Structure of the self-assembled monolayers.

The structure of the adsorbate molecule in thiol-based SAMs is divided into three parts [51]. The first part is the thiol moiety (-SH), also known as the head group. The attachment of the head group to the substrate through chemisorption is the most important process in monolayer formation. The second part is the alkyl chain, referred to as the methylene spacer. Interactions between chains are caused by the van der Waals forces. Although weaker than chemisorption, these forces provide a significant driving force for adsorbate organization. The third part is the terminal function group, or tail group, which is exposed on the outmost surface of the monolayers and exerts the most direct influence.

Prior to the trapping experiments, I formed a monolayer of monodisperse thiol polyethylene glycol (mPEG-thiol) with the head group being the thiol on the surface of the Au or Ag. In this thesis, I used m-dPEG4-thiol ($C_9H_{20}O_4S$) sourced from reference [52]. This compound is described as a monodisperse PEGylation reagent designed to modify gold and silver surfaces or biomolecules with contain free, surface-accessible thiols. The discrete-length PEG (dPEG) spacer has a single molecular weight of 224.32 g/mol, spans 14 atoms (15.8 Å), and features a methyl group at one end and a sulfhydryl group at the other. The sulfhydryl end forms dative bonds with gold and disulfides with free thiols in non-reducing environment. The procedure for preparing the mPEG thiol solution and forming the SAMs is given in Section 2.1.

1.8 Contribution of This Work

Gold nanostructures remain the most used in our group for their application because of their good chemical stability and plasmonics compatibility. However, silver (Ag) offers higher sensitivity and plasmonic resonance among all noble metals. In this thesis, I compare optical trapping on gold (Au) and silver (Ag) nanostructures. Since silver is known to tarnish when exposed to air, I treat the surfaces of both metals with thiol-based self-assembled monolayers (SAMs) and compare these results with those obtained using deionized (DI) water as a control. The objective is to compare and quantify the differences in optical trapping using a double nanohole (DNH) structure in Au and Ag films to trap 20 nm polystyrene (PS) nanospheres in a 32 nm DNH gab size. The remainder of the thesis is organized as follows:

- Chapter 2 describes the fabrication procedure of the DNHs, the scanning electron microscopy (SEM) analysis of the DNH structures, the sample preparation for trapping, the optical tweezer setup, and the data acquisition system.
- Chapter 3 presents the statistical methods, experimental results, analysis of the trapping signal, comparisons, and discussion.
- Chapter 4 concludes the work, presents the limitations of the study, and offers suggestions for future research.

The hypothesis of the study is that optical trapping can be achieved with Ag in a manner similar to Au. Although the optical and chemical properties of Ag may offer advantages, its higher reactivity could lead to increased surface interactions, which might impact trapping performance. Additionally, in the absence of thiol-based SAMs, it is expected that Ag might perform better than Au, potentially resulting in higher trapping force.

Chapter 2

Experiments

2.1 Fabrication

The double nanoholes (DNHs) were fabricated using colloidal lithography following the work of previous group members [35]. A schematic of the fabrication procedure is shown in Figure 2.1.

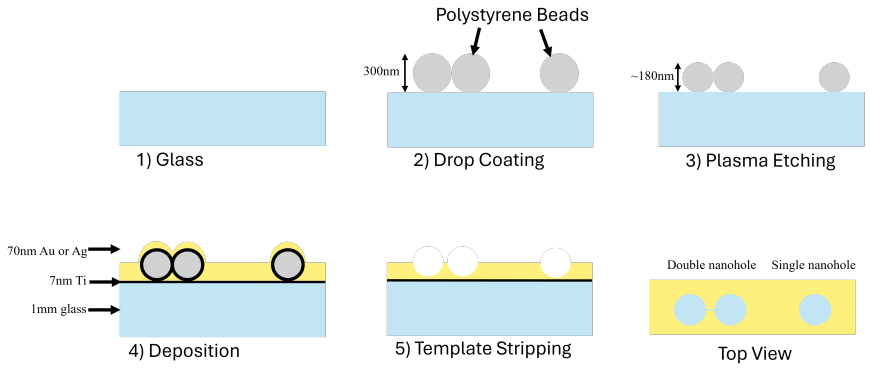

Figure 2.1: Procedure for fabricating double nanoholes using colloidal lithography: 1) clean 1 mm microscopic glass slides, 2) drop-coat 300 nm diameter polystyrene spheres, 3) plasma etching reduces the diameter and gap size of the double nanoholes, 4) deposit a 70 nm thick gold or silver with a 7 nm titanium adhesion layer by sputtering over the slide with the spheres, 5) remove the spheres by sonication to achieve template stripping. The top view shows the fabrication results for both a single and double nanoholes.

The fabrication process began by covering a flat metal block with lens paper. A plain microscope slide (Fisherbrand, $25 \times 75 \times 1$ mm) was placed on the lens paper, and the slide was cut into 2.5 mm $\times$ 2.5 mm pieces using a diamond scribe. I inspected the slides for any debris and gently blew them clean with nitrogen gas. The slides were then placed in a petri dish and plasma-cleaned (Harrick PDC-002) for 15 minutes at high RF powers (45 W), as

shown in Figure 2.2, followed by sonication (Branson 3510) in an ethanol bath for 8 minutes at 40 kHz. After sonication, the slides were rinsed with fresh ethanol and dried with nitrogen gas.

Next, 10 μL of 300 nm polystyrene (PS) beads (Sigma-Aldrich) in 1 ml ethanol were placed in a microcentrifuge tube. Using a pipette, I drop-coated 10 μL of the PS solution onto the glass slides and allowed the slides to rest overnight in a petri dish to let the ethanol evaporate. The solution was applied in a zigzag pattern to prevent the formation of PS bead colonies and ensure even distribution.

Figure 2.2: Harrick (PDC-002) plasma cleaner used for sterilizing the samples as well as for plasma etching.

The following day, I plasma-etched (Harrick PDC-002) at high RF powers. Plasma etching reduces the diameter of the colloidal nanoparticles, allowing for control over the gap size in the DNHs.

The sample was placed in a vacuum chamber, and plasma was generated by applying a radio frequency (RF) electromagnetic field to the electrode. This created reactive plasma by oscillating the electric field and ionizing gas molecules by displacing their electrons [53–56]. The ionized gas then interacted with the sample surface, where the materials on the surface were either broken down and removed by the vacuum system (in the case of plasma cleaning) or etched off the PS nanoparticles (in the case of plasma etching). As a result, exposing the PS nanoparticles to isotropic oxygen plasma for up to 200 seconds reduced their average diameter, leaving some of them connected by small bridges or gaps.

Figure 2.3 shows the Mantis QUBE sputter deposition system used to deposit the metals onto the surface of the glass slides. Sputter deposition is a physical vapor deposition (PVD) technique for creating thin films [56]. Figure 2.4 illustrates this process ,in which ions bombard a target material, ejecting atoms from it. These ejected atoms then travel through the vacuum and are deposited onto a substrate to form a thin film. Argon ions are used to form the plasma, while nitrogen gas is used to vent the chamber allowing the door to open.

Figure 2.3: Mantis QUBE sputter deposition system

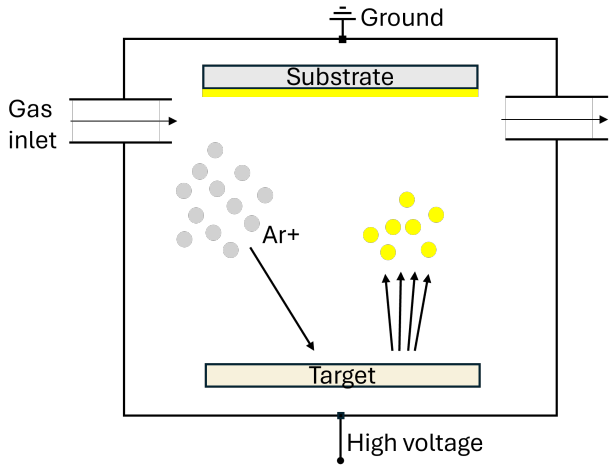

Figure 2.4: Illustration of the sputtering process

I placed six slides at a time inside the chamber (Figure 2.5) and sputtered a 7 nm titanium (Ti) adhesive layer, followed by 70 nm of Au or Ag for the respective films. The Ti acts as an adhesive, attaching either the Au or Ag to the glass slides.

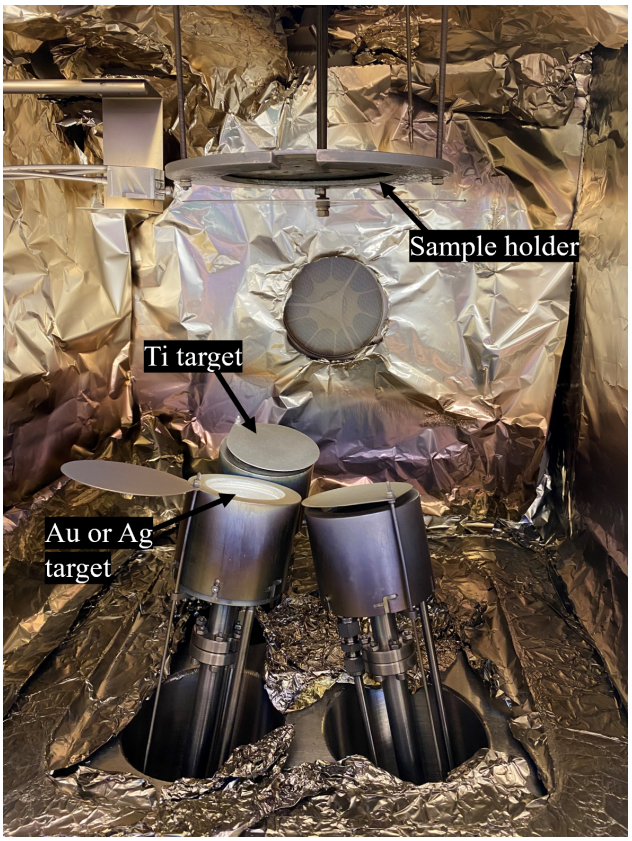

Figure 2.5: Inside the chamber of the Mantis QUBE sputter deposition system.

After sputtering, the samples were placed directly into a bath of ethanol and transported back to the lab in a petri dish to limit exposure to air. The next step is template stripping, where the PS beads (the template) are removed using sonication in a bath of ethanol for 8 minutes. After sonication, the samples are rinsed with fresh ethanol and dried with nitrogen gas.

Following template stripping, I formed a monolayer of mPEG-thiol as described by Section 1.7. I prepared a 5 mM aqueous solution of m-dPEG4-thiol (Sigma-Aldrich, QBD10792), with the chemical formula $C_9H_{20}O_4S$ and a molecular weight 224.32 g/mol. The mass required for molar solution is given by

$$\text{Mass(g)} = \text{Concentration(mol/L)} * \text{Volume(L)} * \text{Molecular Weight(g/mol)} \tag{2.1}$$

To prepare the 5 mM solution, I used 89.729 mg of m-dPEG4-thiol and diluted it in 80 mL of DI water. I then placed the fabricated samples in a petri dish filled with either the aqueous solution of m-dPEG4-thiol (the "experiment" group), or with DI water only (the "control" group). The samples were divided into the following groups: 3 samples of Au-Ti in mPEG thiol, 3 samples of Au-Ti in DI water only, 3 samples of Ag-Ti in mPEG thiol, and 3 samples of Ag-Ti in DI water only.

Each petri dish was flushed with nitrogen, sealed with parafilm, and left in a storage container overnight at room temperature and atmospheric pressure. The samples were left for at least one night to allow the mPEG-thiol monolayer to grow on the surface. The PEG thiol attaches to the metal surface via the sulfur bond, forming a self-assembled monolayer (SAM) [49, 50]. This newly developed surface protects metals such as Ag from tarnishing.

Next day, I took one sample from each group to the scanning electron microscope (SEM) to view the double DNHs and estimate the gap sizes. Prior to SEM imaging or optical trapping, I rinsed the samples thoroughly with DI water and dried them with nitrogen gas to remove any non-chemisorbed PEG thiol molecules.

2.2 Scanning Electron Microscopy

After the samples were fabricated and left overnight in either DI water or mPEG thiol, I used the Hitachi S-4800 field emission scanning electron microscope (SEM) (Figure 2.6) to locate the DNH apertures and estimate the gap sizes of the samples.

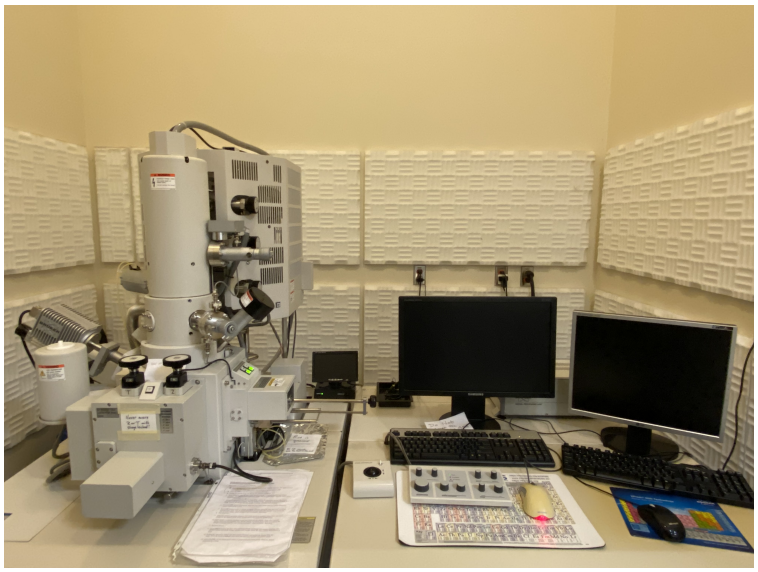

Figure 2.6: Hitachi S-4800 field emission scanning electron microscope.

2.2.1 Principle

Figure 2.7 shows the operating principle of the SEM. The SEM is an instrument that utilizes a finely converged electron beam to scan a sample surface in a vacuum, detecting the information produced from the sample and presenting an image of the surface [57,58]. Irradiating the sample with an electron beam in a vaccum generates secondary electrons, backscattered electrons, characteristic X-rays, and other signals.

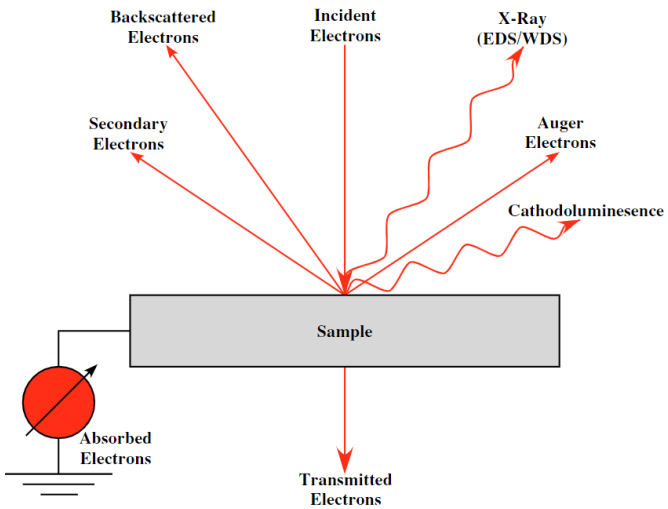

Figure 2.7: Schematic drawing of a scanning electron microscope (SEM) illustrating the various signals produced. Reproduced from reference [58].

Secondary electrons (SE) are generated in proximity to the sample surface, and their detection reflects the fine topographical structure of the sample [57, 58]. Backscattered electrons (BSE) are reflected when they strike the atoms composing the sample. The number of these electrons depends on the compositing of the sample (crystal orientation, average atomic number, etc). The BSE image reflects the compositional distribution on the sample surface. An X-ray detector is used for conducting elemental analysis to determine which elements are present in the sample. Since we are primarily interested in obtaining the topographical information of the sample, I used the secondary electrons detector (SE) when imaging the metals and locating the DNHs.

2.2.2 Plasma Etching Experiment

Without plasma etching, the gap size between the DNHs was approximately $112 - 124$ nm. After etching for 170 seconds, the gap size was reduced to around $18 - 23$ nm, and after 130 seconds of etching, the gap size measured about $30 - 35$ nm. To effectively trap 20 nm PS particles, I aimed for an average gap size of around 32 nm. This controlled reduction of the gap size is crucial for optimizing the trapping capabilities of the nanoholes.

2.2.2.1 Plasma etching for 170 seconds

After 170 seconds of plasma etching, the gap sizes in the DNHs were measured to be $18 - 23$ nm, as shown in Figure 2.8. These samples were subsequently fabricated and shipped to the Nano Surfaces Division at Bruker in Berlin, Germany, for trapping pristine Boron Nitride (BN) nanoflake solution, and to our collaborators at the Okinawa Institute of Science and Technology in Okinawa, Japan, for trapping Bovine Serum Albumin (BSA).

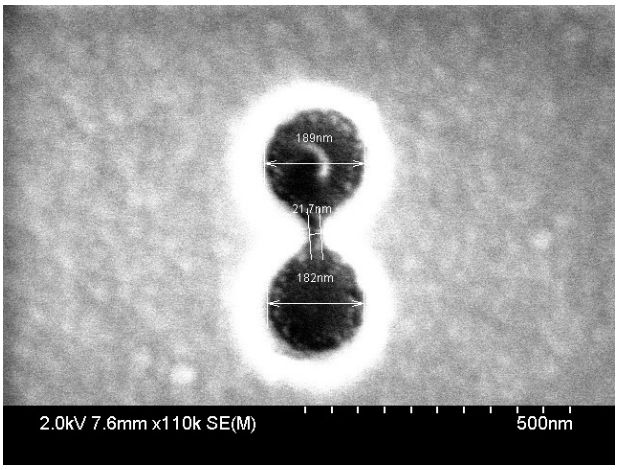

(a) DNH of gap size 21.7 nm and diameters of 182 − 189 nm.

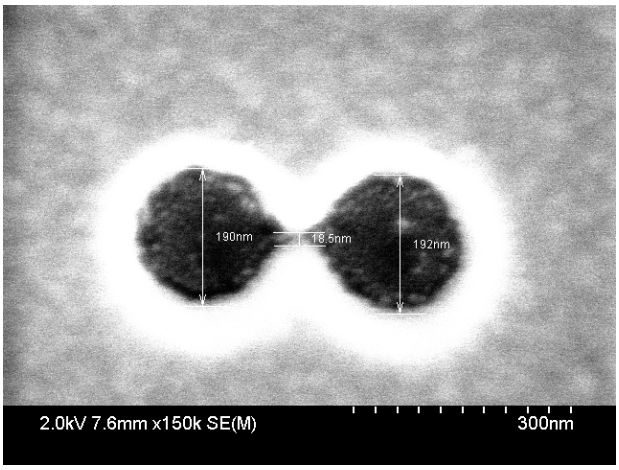

(b) DNH of gap size 18.5 nm and diameters 190− 192 nm.

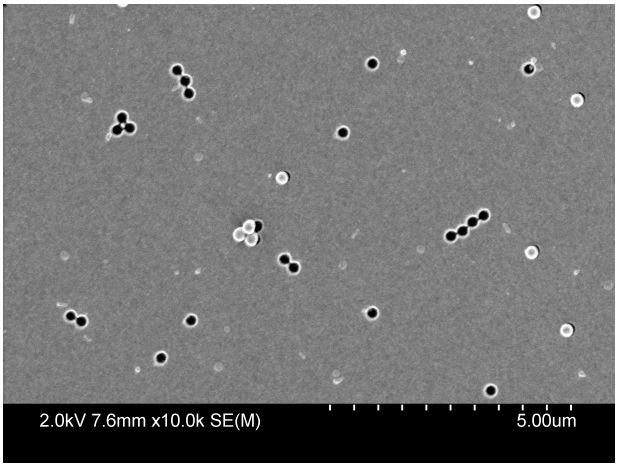

(c) Single, double, triple nanoholes.

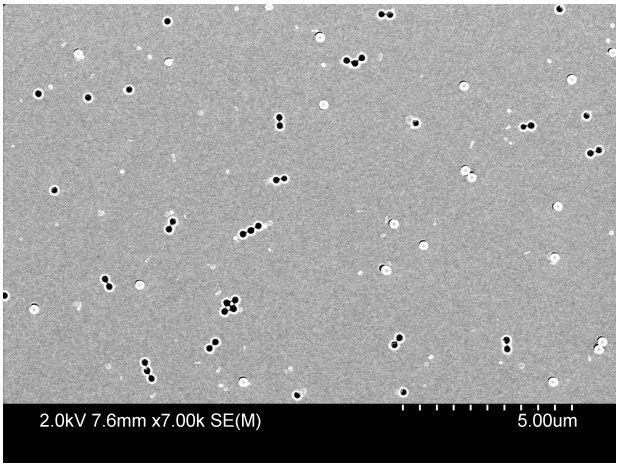

(d) Another region showing various structures.

Figure 2.8: Plasma etching for 170 seconds in 7 nm Ti, 70 nm Au, 8 minutes sonication.

2.2.3 SEM of DNHs for Gold and Silver Used for the Optical Trapping Experiments

Here, I present the results of the DNHs in gold and silver used for the optical trapping experiments in this thesis. Section 2.2.3.1 shows the fabrication results for gold in DI water (Figures 2.9, 2.10) and gold with the mPEG thiol monolayer (Figures 2.11, 2.12). Section 2.2.3.2 presents the corresponding results for silver in DI water (Figures 2.13, 2.14) and silver with the mPEG thiol monolayer (Figures 2.15, 2.16). These results confirm that the fabrication of DNHs in both gold and silver was successful, with an average gap size of approximately 32 nm.

2.2.3.1 Gold

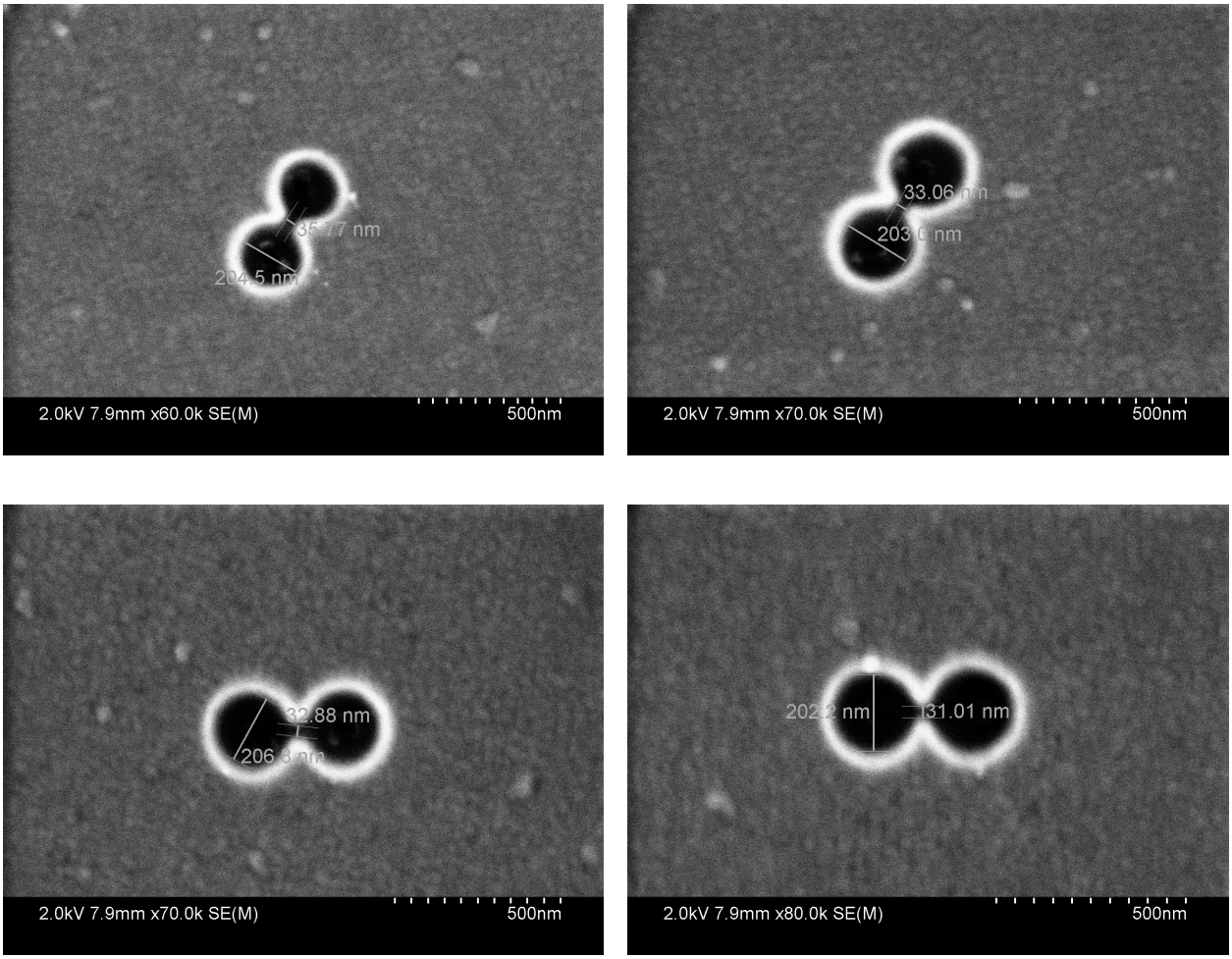

Figure 2.9: Double nanoholes in gold DI water with 130 seconds plasma etching.

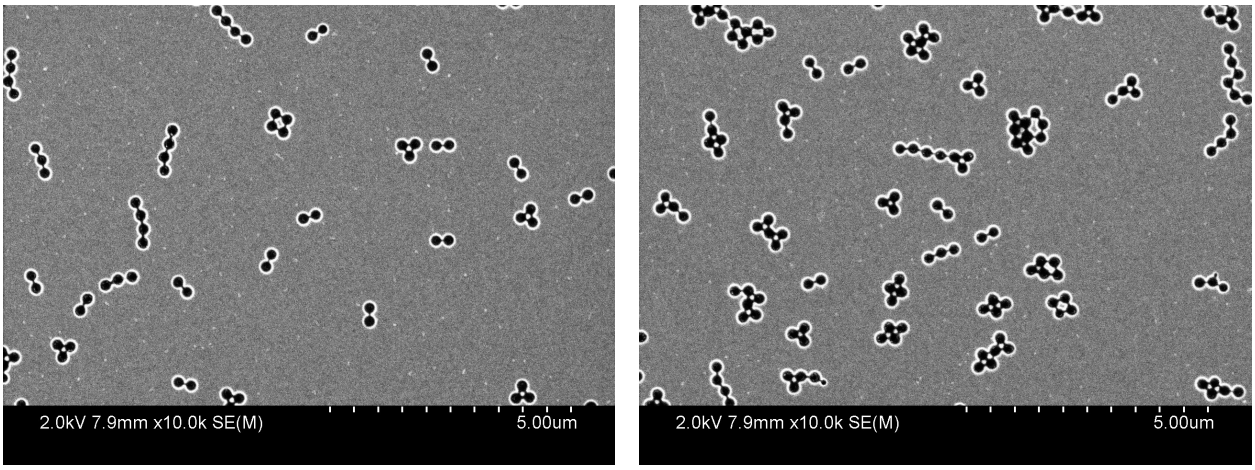

Figure 2.10: Various structures fabricated in gold DI water with 130 seconds plasma etching,

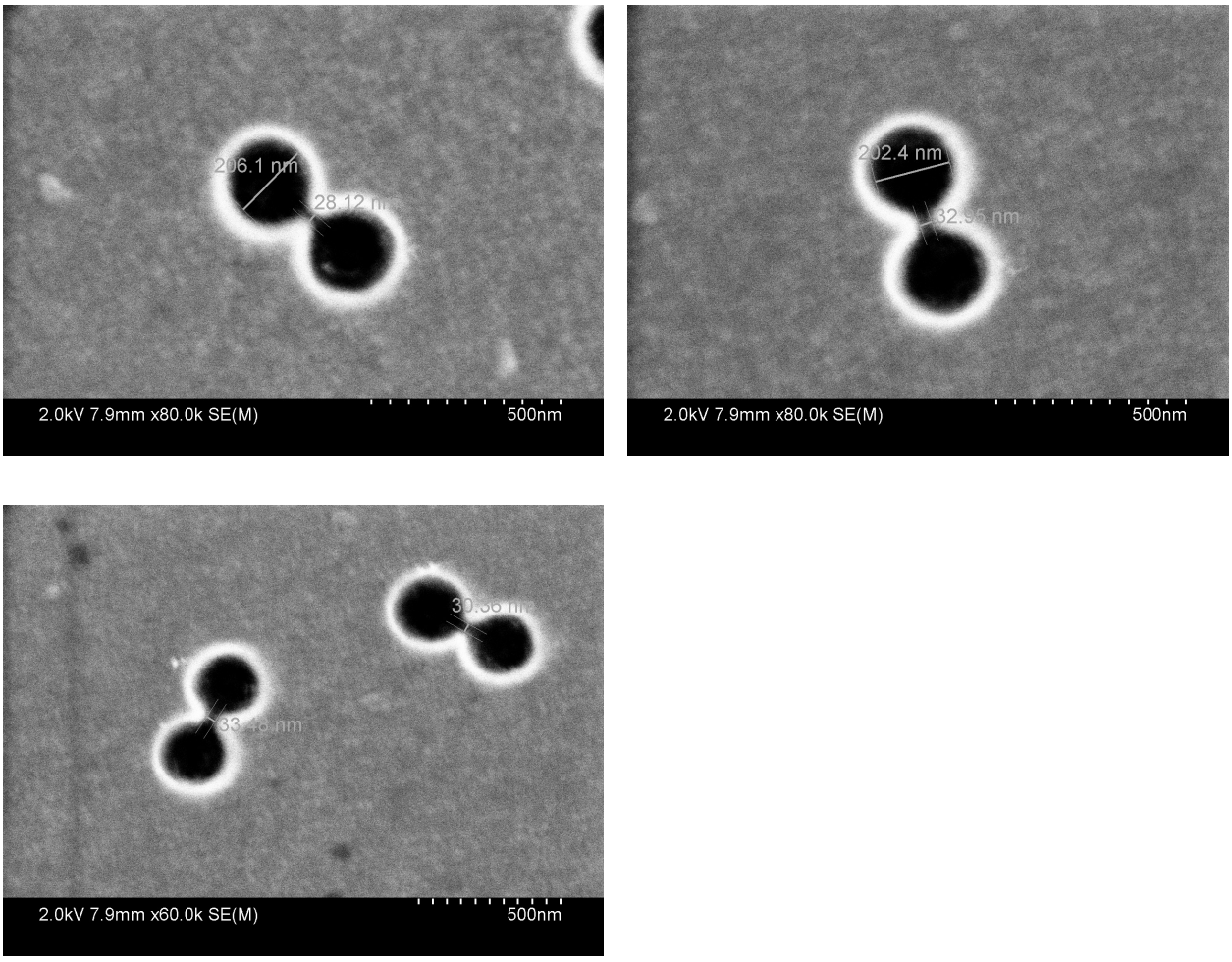

Figure 2.11: Double nanoholes in gold mPEG thiol with 130 seconds plasma etching.

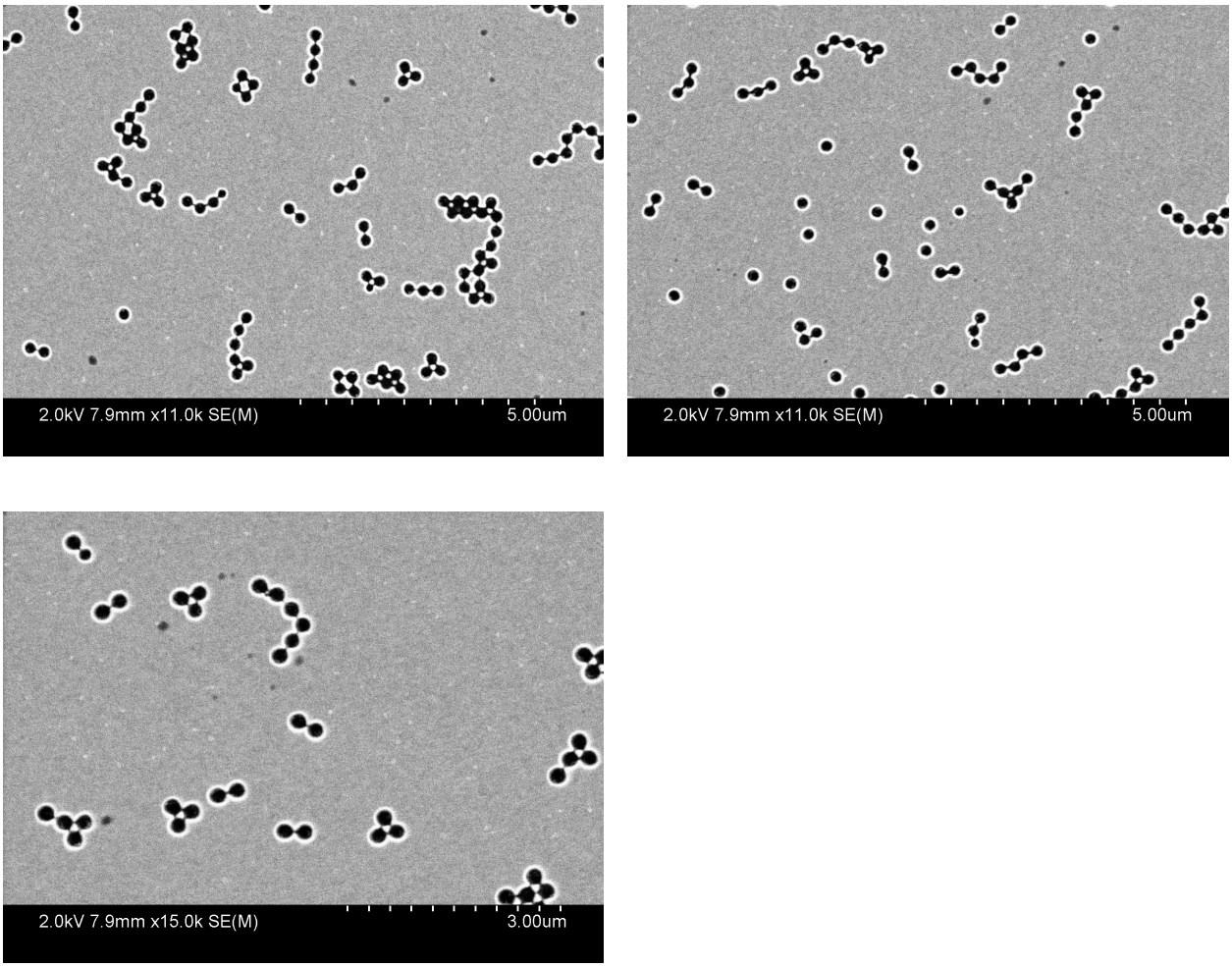

Figure 2.12: Various structures fabricated in gold mPEG thiol with 130 seconds plasma etching.

2.2.3.2 Silver

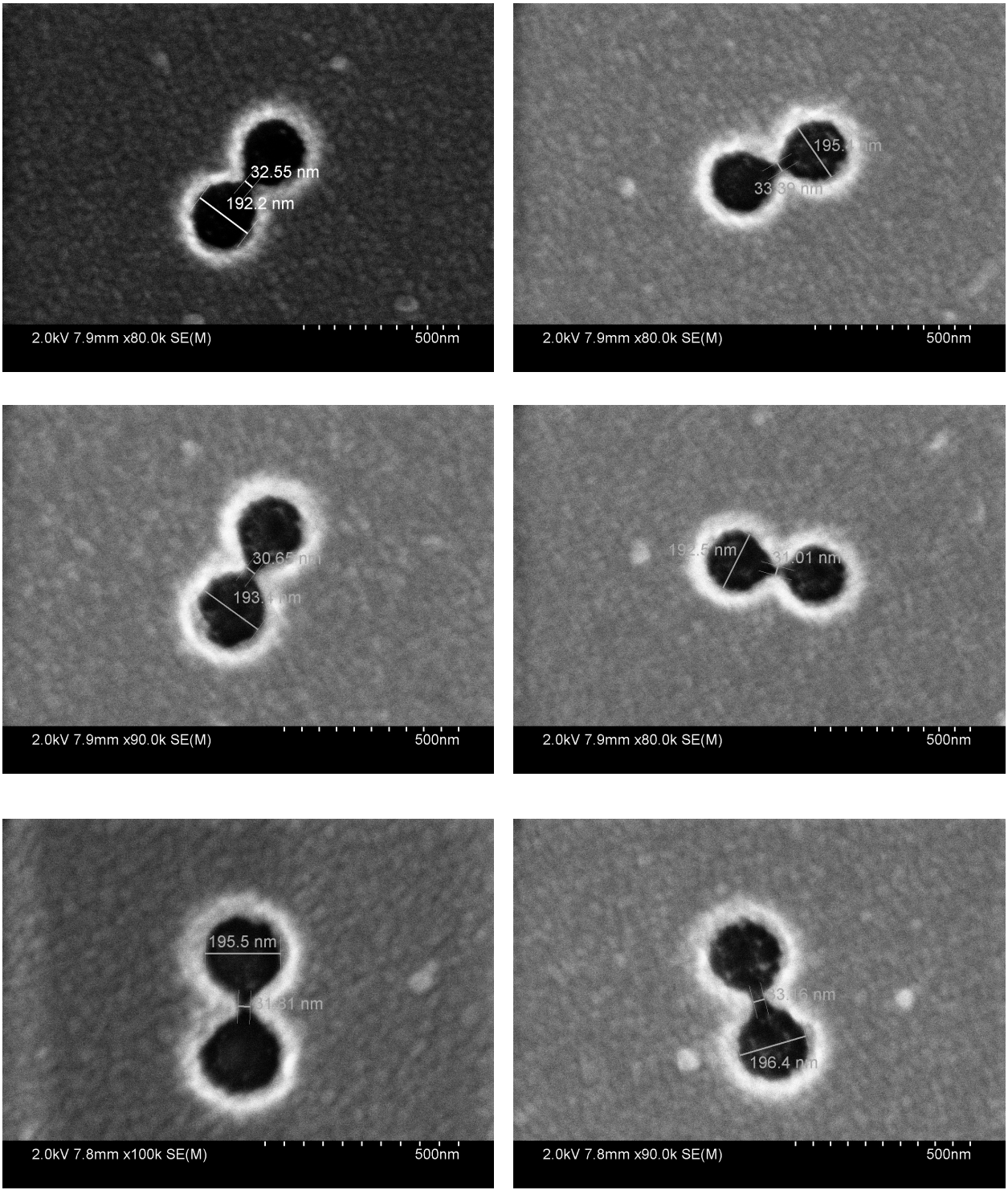

Figure 2.13: Double nanoholes in silver DI water with 130 seconds plasma etching.

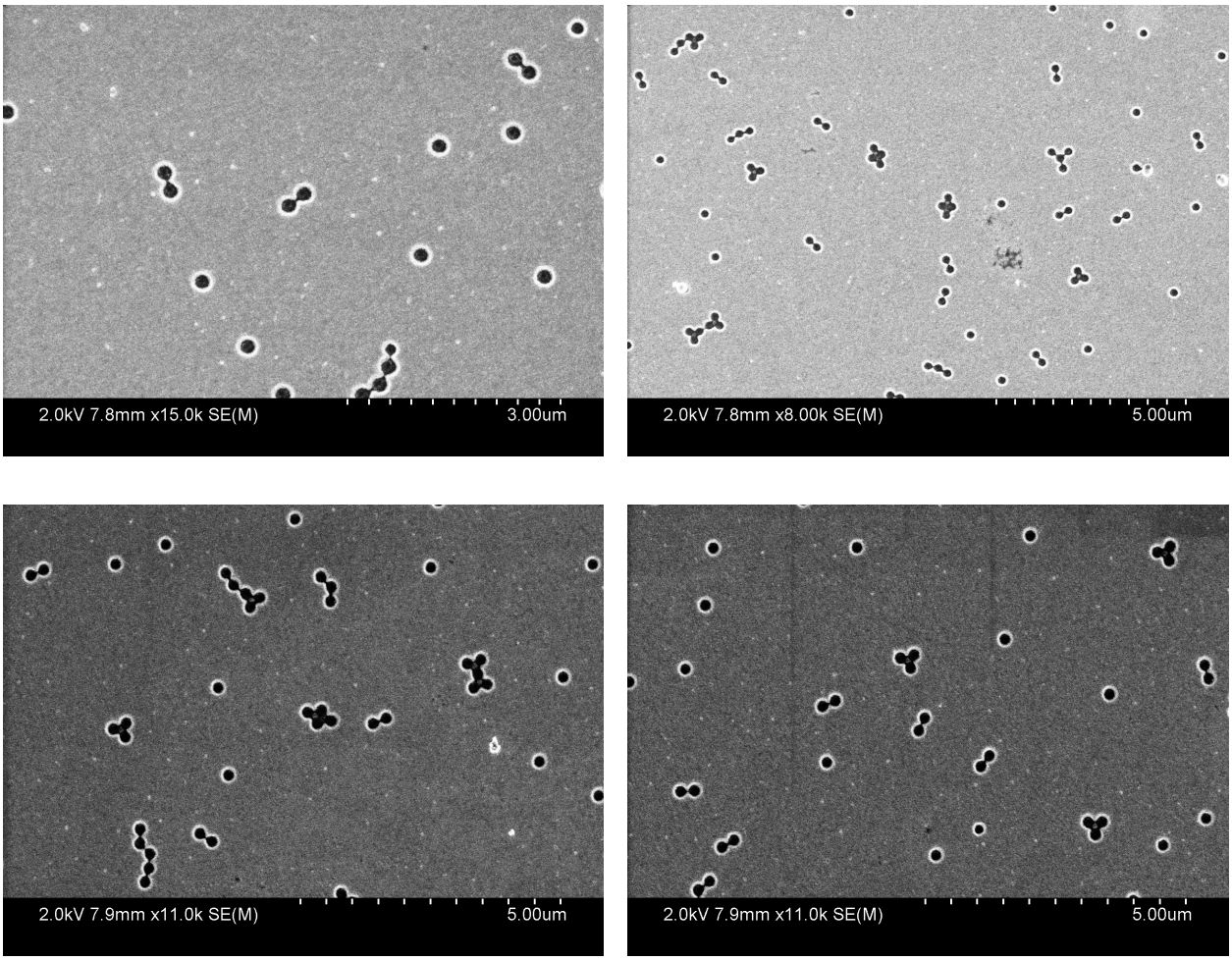

Figure 2.14: Various structures fabricated in silver DI water with 130 seconds plasma etching.

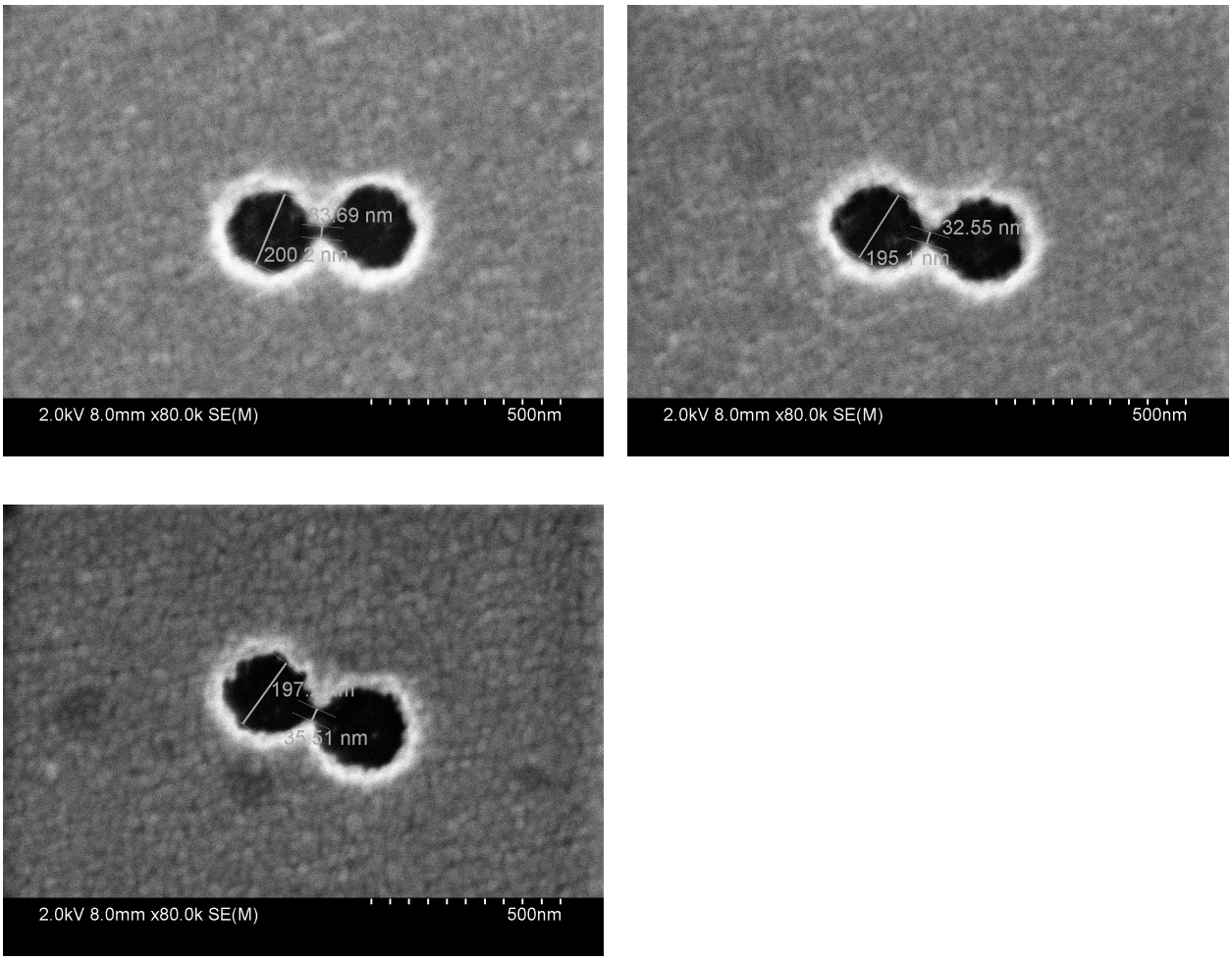

Figure 2.15: Double nanoholes in silver mPEG thiol with 130 seconds plasma etching.

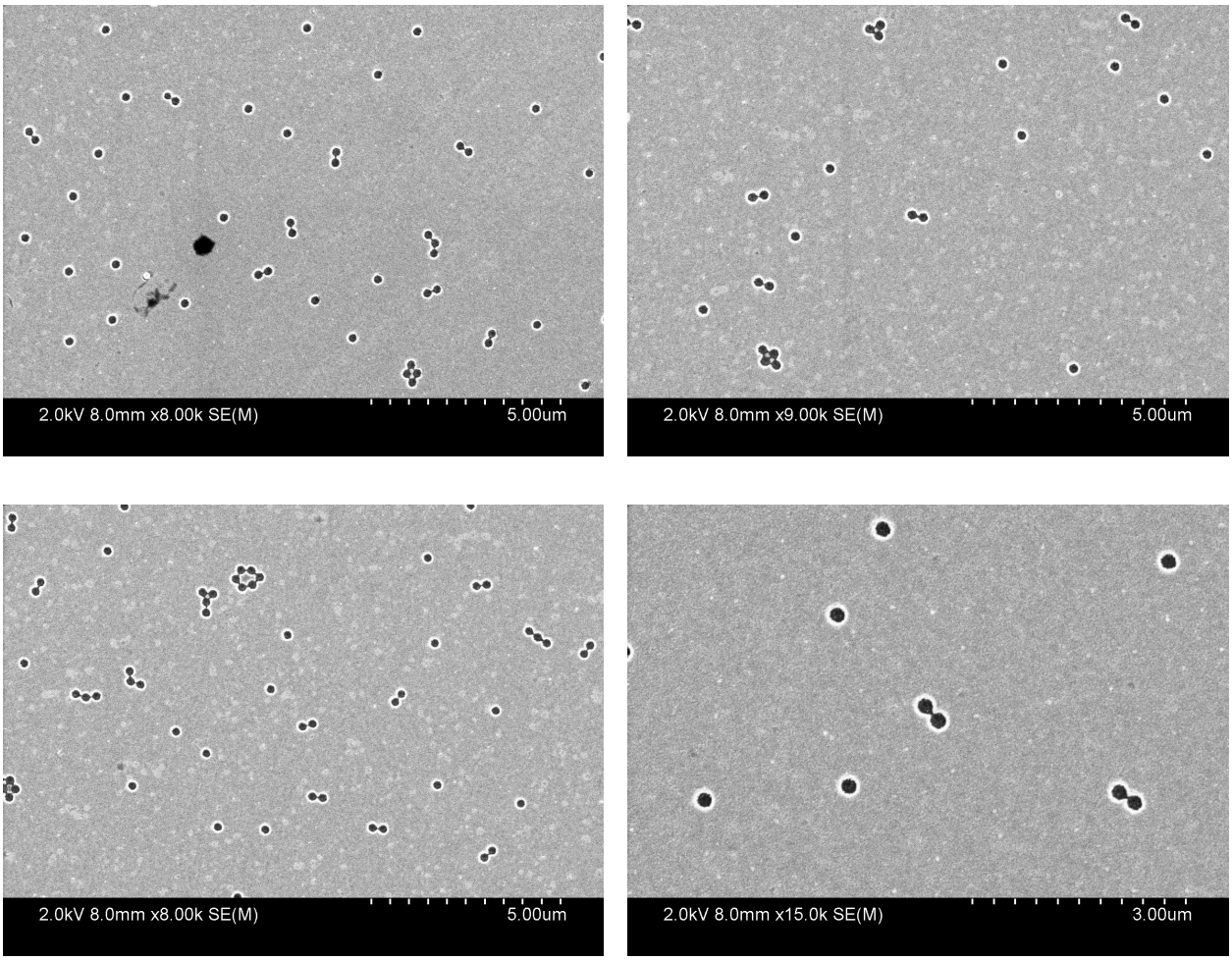

Figure 2.16: Various structures fabricated in silver mPEG thiol with 130 seconds plasma etching.

2.3 Sample Preparation for Trapping

Prior to trapping, the 2.5 cm × 2.5 cm DNH samples were rinsed with DI water to wash off the PEG thiol and dried with nitrogen gas. The samples were then cut into four quadrants, each approximately the same size as the image spacer (1.25 cm × 1.25 cm), to provide a flat surface and ensure that the samples adhere well to the image spacer.

Figure 2.17 illustrates the procedure used to prepare the sample prior to trapping. The trapping solution was prepared using a pipette by diluting 10 μL of 20 nm PS beads (ThermoFisher Scientific, 3020A) into 0.5 ml of DI water.

A metal block with a flat surface was used to hold the DNH sample and a microscope

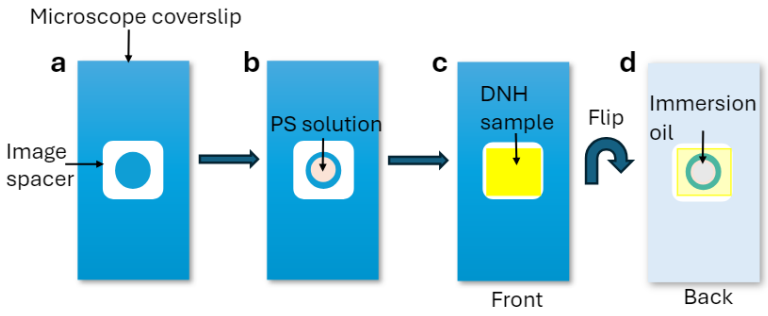

Figure 2.17: Procedure for sample preparation for the optical trapping experiment: (a) the microscope cover glass with the image spacer, (b) 10 μL of 20 nm polystyrene (PS) was dropped and confined within the image spacer, (c) mount the DNH sample onto the image spacer, (d) flip the coverslip and apply immersion oil.

coverslip (Gold Seal, 24 × 60 mm, No. 1. #1419 − 10). A double-sided adhesive chamber spacer (Grace Bio-Labs, 9 mm × 1.12 mm, GBL654008-100EA) was peeled and adhered to the coverlip. Then, 10 μL of trapping solution was confined to the spacer. The DNH sample was mounted onto the spacer, sealing the solution and immersing the DNHs in the PS solution.

Finally, the sample was flipped, and immersion oil was added to the centre of the image spacer. The oil immersion allows the objective to achieve a high numerical aperture (NA), maximizing light collection by the objective lens.

The sample is now ready for transfer to the optical tweezer setup, where it will be positioned on the stage between the objective and condenser.

2.4 Optical Tweezer Setup

Figure 2.18 shows a schematic of the optical tweezer setup used for the trapping experiment. The setup consists of a single-frequency distributed feedback (DFB) diode laser (eagleyard, DFB-0852-00050-BFY02-0002) with a wavelength of 852 nm. The laser is collimated (Thorlabs, PAF-X-7-B), polarized (Thorlabs, LPNIRE100-B), and expanded (Thorlabs, ACN254-050-B and AC254-150-B). To protect the laser diode against optical feedback, an optical isolator (OZ OPTICS LTD. #FOPI-11-11-850-5/125-S-40-3A3A-1-1-30) was installed to prevent disturbances to the emission spectrum.

The laser beam was steered using kinematic mirrors that are highly reflective and silver-coated (Thorlabs, #PF10-03-P01) until it reached the objective. The sample is placed on

a three-axis stage with piezoelectric actuators, which are controlled by the "APT System Software" provided by Thorlabs. The 100× oil immersion Nikon objective lens, with a numerical aperture of 1.25, focuses the laser beam to a spot size of 1.1 μm on the sample. The transmitted light is collected from the sample using a Nikon 10× air condenser with a numerical aperture of 0.25 and detected by an avalanche photodetector (Thorlabs, APD110A). A half-wave plate (HWP) and a linear polarizer (LP) are installed to configure and fine-tune the polarization of the beam on the DNH. Visible light from the LED source illuminates the sample, and the resulting image is captured by a CCD camera with a 1280 × 1024 pixel resolution (Thorlabs, DCU224C).

The camera allows for real-time observation of the DNHs on the sample. The piezoelectric stage is used to align the target DNH to the location of the laser, and the half-wave plate is rotated to align the polarization along the axis of the DNH gap for maximum transmission. After confirming that the aperture is a DNH, I wait for the PS nanospheres to become trapped in the gap.

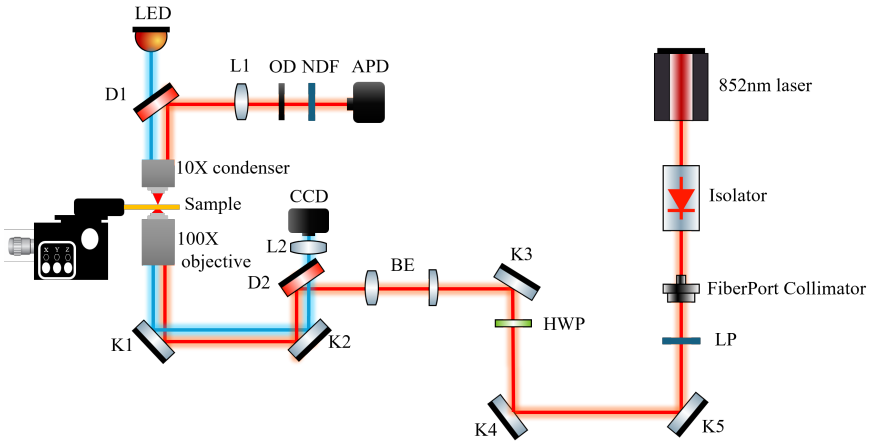

Figure 2.18: Schematics of the 852 nm laser setup used for the trapping experiments showing the various components: linear polarizer (LP), half-wave plate (HWP), kinematic mirrors (K1-K5), beam expander (BE), dichroic mirrors (D1, D2), focusing lens (L1, L2), optical density filter (OD), neutral density filter (NDF), avalanche photodetector (APD), and a charge-coupled device (CCD).

Prior to trapping, the laser power at the objective was measured using a power meter (Thorlabs, S132A) with an uncertainty of ±5%. Figure 2.19 shows the measured laser power at the objective, which is used for trapping.

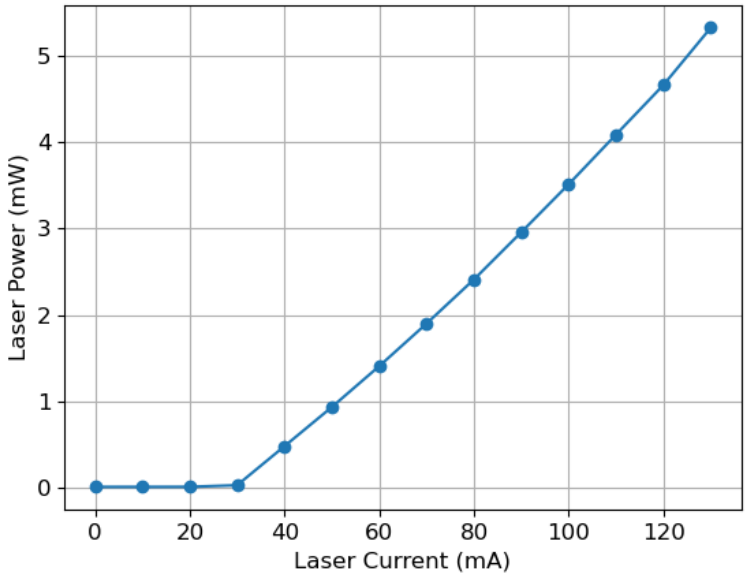

Figure 2.19: Trapping power as measured at the objective prior the trapping experiment.

Laser current (mA)	Laser power (mW)
0	0.01
10	0.01
20	0.01
30	0.03
40	0.48
50	0.94
60	1.41
70	1.90
80	2.41
90	2.96
100	3.51
110	4.09
120	4.66
130	5.32

Table 2.1: Trapping power for the 852 nm laser setup as measured at the objective. The laser driver (Thorlabs, CLD 1015) had a current accuracy of $\pm(0.1\% + 500\ \mu\text{A})$, while the optical power meter (Thorlabs, S132A) had an uncertainty of $\pm 5\%$.

2.5 Data Acquisition System

The transmission through the DNH was measured using an APD. An absorptive neutral density filter (Thorlabs, NE10A-B) was placed in front of the APD to minimize surface reflections within the $650 - 1050$ nm range, thereby reducing the amount of stray light present. And, an optical density filter (Thorlabs, NE06A, 0.6) was used to limit the power incident on the APD.

The signal was acquired using an Advantech USB-4711A-BE, 12-bit USB Multifunction module with the frequency sampling rate set to 100 kHz and a single-ended 3 V mode was configured prior to acquisition. The data was then exported from the Advantech DAQNavi Datalogger software as a text (.txt) file to python for further analysis. Figure 2.20 illustrates the data acquisition system.

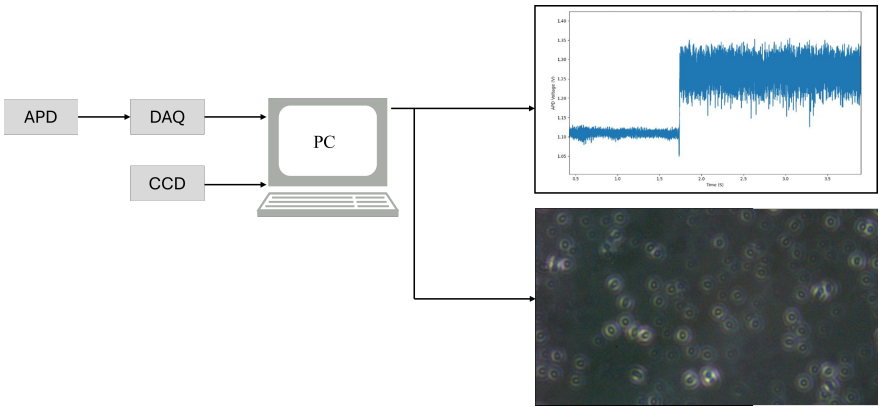

Figure 2.20: The data acquisition system illustrating how the data was acquired for the trapping setup. The trapping data is detected by an avalanche photodetector (APD) and was acquired by a data acquisition (DAQ) device. The sample was imaged by the charge-coupled device (CCD).

Steps:

1. Measure the laser power at the objective; this is the trapping power.
2. Place the sample on the piezoelectric stage.
3. Turn on the LED.
4. Find the DNH on the CCD camera.
5. Turn on the laser.

6. Align the DNH with the laser spot.
7. Wait for the nanoparticle to become trapped in the gap.
8. Record the trapping data from the APD.
9. Export and analysis the data.

Chapter 3

Results and Discussion

In this study, polystyrene (PS) beads (Thermofisher, 3020A) with diameters of 20 nm were used according to the method described in Section 2.3. Polystyrene was chosen due to its dielectric properties, well-defined spherical shape, and small size, making it ideal for optical trapping experiments [59,60]. The beads are low-cost, small enough to be studied, and serve as a proof of concept for developing sensors that could later be adapted for trapping exotic nanoparticles. Experiments in a given system were repeated at least five times, each time with a different bead and a different DNH.

3.1 Statistical Methods

Experimentally, after acquiring the trapped data as a function of time, I estimate the power spectrum density (PSD) using the Welch method. The experimentally obtained PSDs are of the dimension V^2/Hz. The PSD function describes how the signal's average power is distributed across various frequencies. Welch's method employs the Fast Fourier Transform (FFT) to estimate the PSD. It divides the data into overlapping segments, calculates a modified periodogram for each segment, and averages these periodograms to produce the final estimate [61].

Next, the PSD was fitted using a non-linear least squares approach with a Lorentzian function of the form:

$$\frac{A}{f_s^2 + f_c^2}, \tag{3.1}$$

where the corner frequency (f_c) was determined for each spectrum. The frequency corresponding to the maximum curvature of this curve is termed the corner frequency. The sampling frequency f_s is set at 100 kHz, and A is the experimental obtained diffusion constant with dimensions of V^2/s. Normally, the diffusion constant is measured in units of

(length)^2/time, however, experimentally it is determined as a function of voltage from the PSD [62], compared to the units of (arb units)^2/s given by reference [37].

From Section 1.5, the trap stiffness (force constant) was calculated as

$$k = 2\pi\gamma_0 f_c, \tag{3.2}$$

where the friction coefficient $\gamma = 3.045 \times 10^{-10}$ Ns/m. The trap stiffness, k, describes the force field on the trapped particle as it attempts to move away or escape from the trap centre, analogous to the spring constant. The time constant, τ, which describes the decay of the trap was determined via the relation $\tau = \frac{1}{2\pi f_c}$.

Data Analysis Steps:

1. Plot the full trapping signal against time.
2. Apply a low-pass filter (Savitzky-Golay) to the full signal to distinguish between the laser signal and the trapped signal.
3. Select 5 seconds of the trapped data.
4. Set a frequency limit of 10 Hz and estimate the power spectral density (PSD) of the trapped data using Welch's method.
5. Fit a Lorentzian function to the PSD and extract the corner frequency.
6. Calculate the time constant and trap stiffness as a function of laser power.

Examples of Discarded Data:

- Low transmission (around 1 V) indicates a single nanohole.
- Very high transmission (over 2.5 V) indicates a cluster of nanoholes.
- Traps that do not last long (a few milliseconds).
- Erratic data at low trapping powers (approximately ≤ 3 mW).
- The laser beam is over-focused or under-focused (distance from sample to objective is too short or too long).
- Excessive immersion oil causing samples to be sloppy, resulting in unstable signals.
- Construction noise on campus.

3.2 Nanostructures in DI Water

3.2.1 Gold in DI Water

Polystyrene nanospheres with a diameter of 20 nm were used for the trapping experiments using the optical tweezer setup described in Chapter 2.4. This subsection presents the experimental results for the gold-titanium (Au-Ti) DNH in a DI water environment. A DNH structure with an average gap size of around 33.7 nm was fabricated. The SEM images of the DNHs in Au-Ti DI water are shown in Section 2.2.3.1, Figure 2.9.

Figure 3.1 shows the full trapping event in the Au-Ti DI water, where the laser was turned on at $t = 0$ s. The trapping power was held constant at 3.51 mW $\pm$ 5%. The transmission signal through the DNH is measured by using an avalanche photodetector (APD). At $t = 3$ s, the voltage signal indicates the presence of the trapped particle, which remains stable until the laser is turned off at $t = 23$ s, when the particle is released from the trap. The trapped signal shows an increase in the intensity fluctuation of the transmitted signal caused by the Brownian motion of the nanosphere in the DNH optical trap.

Figure 3.2 details the analysis steps of the trapping signal. Figure 3.2a provides a close-up view of the trapping signal from Figure 3.1, highlighting the region of interest. A Savitzky-Golay filter is applied in Figure 3.2b to smooth the signal and identify noise components. A 5-second interval of trapping data is selected in Figure 3.2c for subsequent PSD analysis. The PSD plot in Figure 3.2d displays the fitted Lorentzian curve, which enables the determination of the corner frequency $f_c = 349.1 \pm 1.3$ Hz, the time constant $\tau = 0.000456 \pm 1.71 \times 10^{-6}$ s, and the experimental diffusion constant $A = 0.2930 \pm 0.0017$ V^2/s.

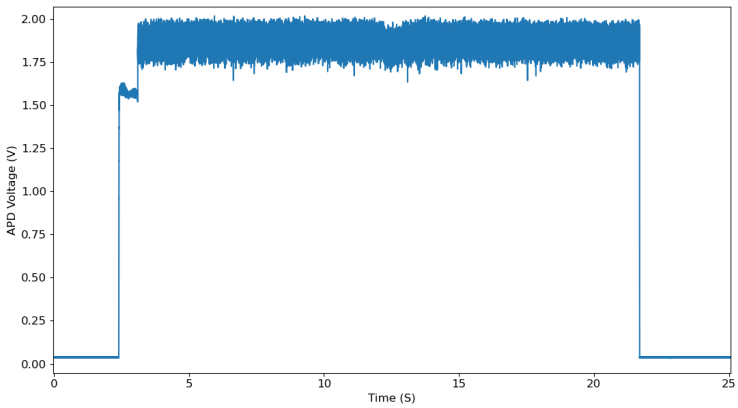

Figure 3.1: Full trapping event in Au-Ti DI water. The laser was turned on at $t = 0$ s and turned off at $t = 23$ s.

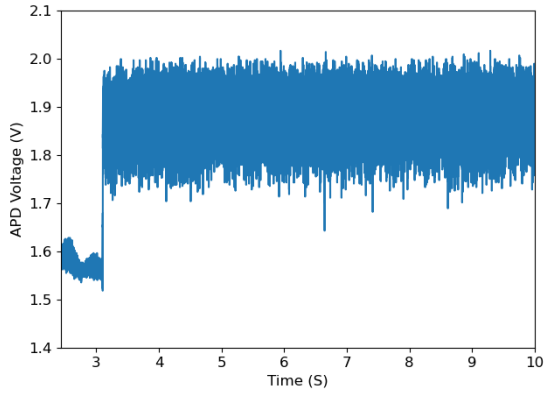

(a) Close-up view from Figure 3.1.

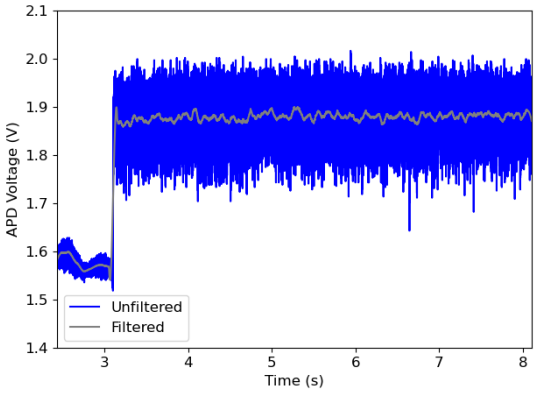

(b) Savitzky-Golay filter.

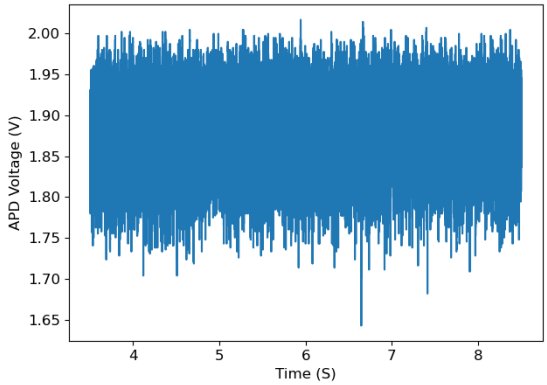

(c) Select 5-seconds of the trapped data.

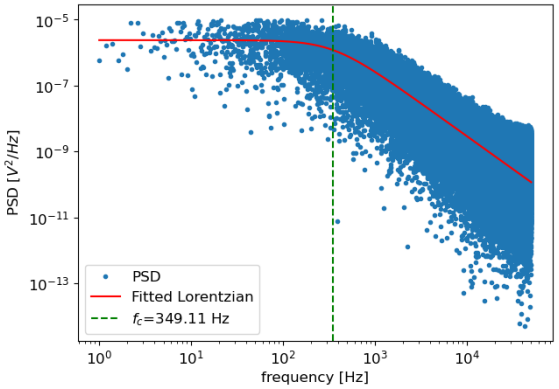

(d) PSD plot with a fitted Lorentzian curve.

Figure 3.2: Analysis of a trapping event for a 20 nm polystyrene bead in a double nanohole (gap size $\approx$ 33.7 nm) in an Au-Ti DI water sample. The laser current was constant at 100 mA (trapping power 3.51 mW $\pm$ 5%).

Figure 3.3 presents histograms of the trapped signal, providing the mean and standard deviation to show the distribution of the signal voltage around the mean position of the trapped particle. A Gaussian probability density function is fitted to the histogram, suggesting that the voltage distribution is slightly skewed from a perfect Gaussian shape.

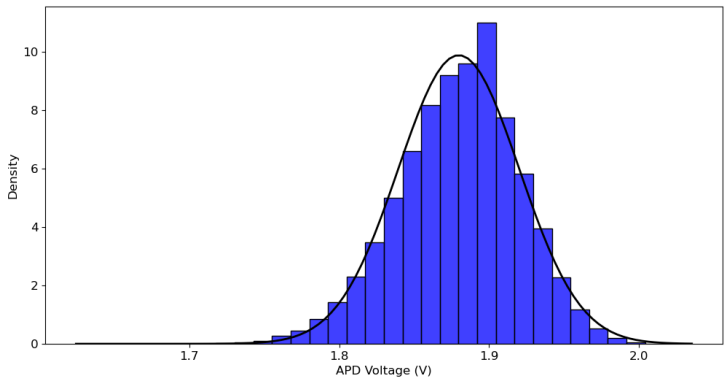

Figure 3.3: Histograms (blue) and Gaussian probability density function (black line) of the trapped signal for Figure 3.2c. The mean is $\mu = 1.88$ V, and standard deviation is $\sigma = 0.04$ V.

A second trapping event is shown in Figure 3.4, with a close-up view shown in Figure 3.4b to emphasize the fluctuation in the trapped signal. These figures confirm the trapping stability observed in the same DNH as Figure 3.1, demonstrating consistent optical trapping performance.

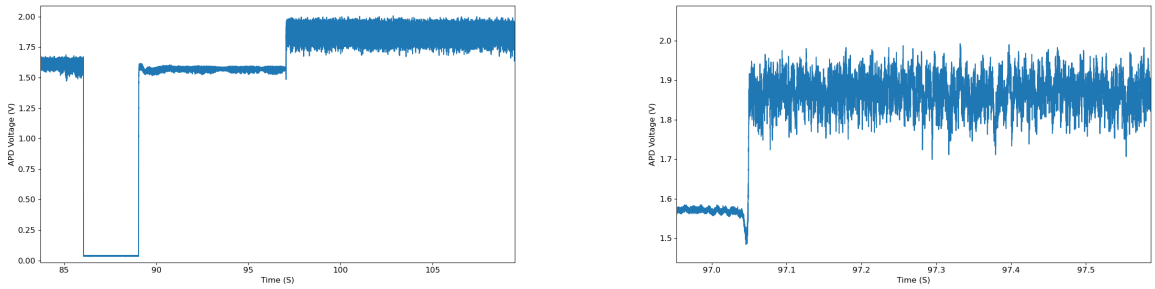

(a) Second trapping signal.

(b) close-up view from Figure 3.4a.

Figure 3.4: Second trap in Au-Ti DI water on the same DNH as Figure 3.1.

I investigated the power dependence of the optical trap, as seen in Figure 3.5. The experiment began with a laser current of 70 mA (corresponding to 1.90 mW $\pm$ 5%) and increased in 10 mA increments, reaching a maximum of 130 mA (5.23 mW $\pm$ 5%). Figure 3.6 indicates that a minimum trapping power of at least 3.51 mW $\pm$ 5% is required for stable trapping.

The power-dependent PSD plots with Lorentzian fits, shown in Figure 3.7, demonstrate how increasing power affects the trapping characteristics. The calculated trap stiffness, κ,

derived from these PSD plots, is plotted as a function of laser power in Figure 3.8. This relationship indicates a linear increase in stiffness with power, improving the trap's ability to hold particles.

Similarly, the inverse of the time constant, τ^{-1}, is plotted against laser power in Figure 3.9, showing a linear dependence. This trend supports the conclusion that power influences trapping stability and increases the trap stiffness. A summary of the results from trapping in Au-Ti DI water at different laser powers is provided in Table 3.1.

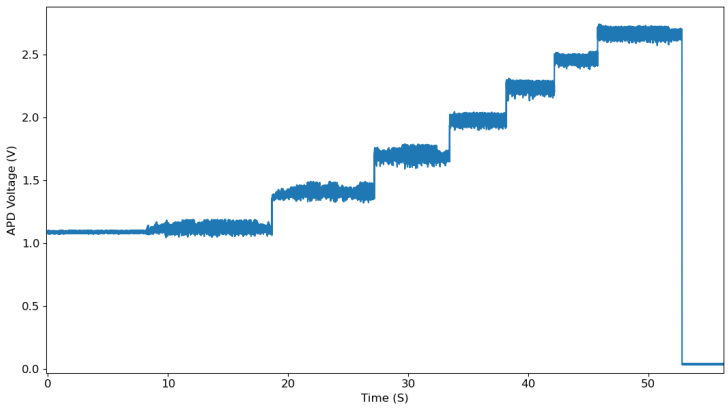

Figure 3.5: Trapping event at different incident trapping laser powers in Au-Ti DI water. The laser was turned on at $t = 0$ s, with a current of 70 mA. The current was then increased in increment of 10 mA during the trap. The laser was turned off at $t = 52$ s.

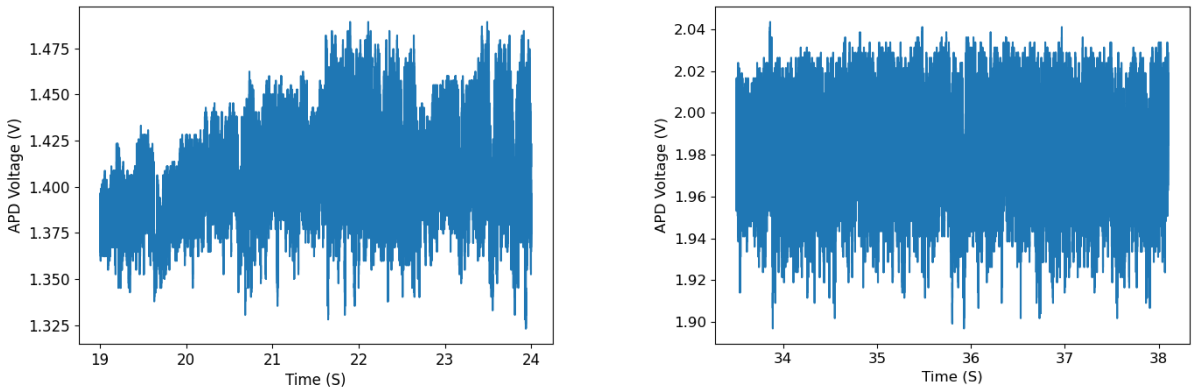

(a) Trapped signal at 80 mA (2.41 mW $\pm$ 5%). (b) Trapped signal at 100 mA (3.51 mW $\pm$ 5%).

Figure 3.6: Comparison of trapping stability at 80 mA and 100 mA in Au-Ti DI water, demonstrating that a current of 100 mA results in a more stable trapping signal. For the original trapping signal, refer to Figure 3.5.

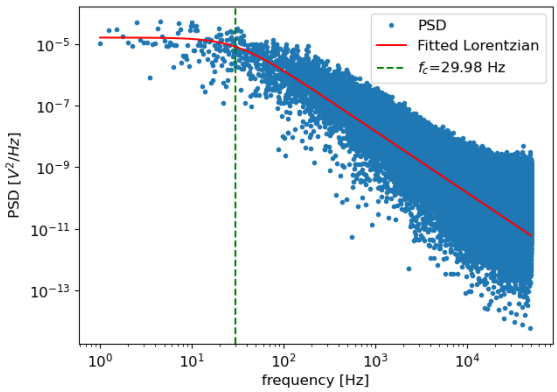

(a) At 90 mA (2.96 mW $\pm$ 5%).

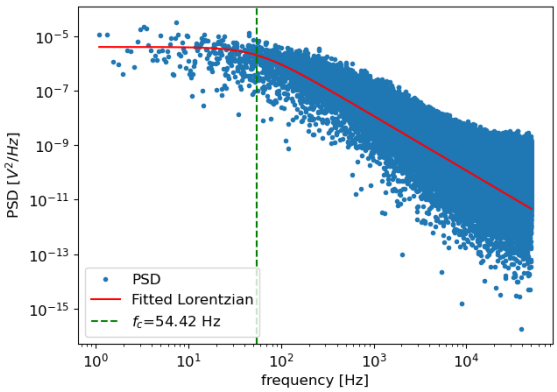

(b) At 100 mA (3.51 mW $\pm$ 5%).

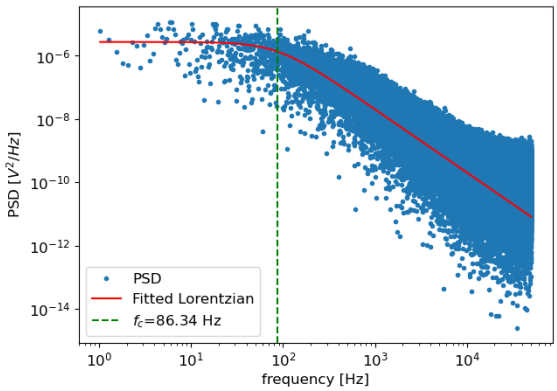

(c) At 110 mA (4.09 mW $\pm$ 5%).

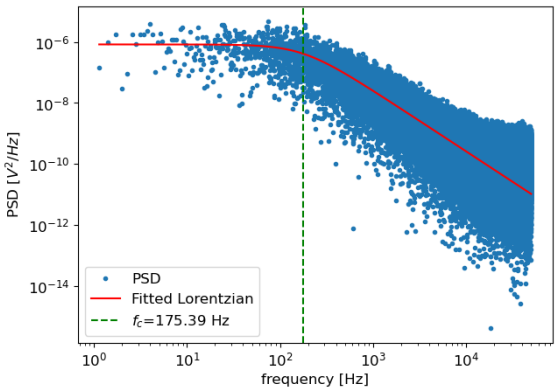

(d) At 120 mA (4.66 mW $\pm$ 5%).

Figure 3.7: The PSD with fitted Lorentzian for different lasers powers in Au-Ti DI water.

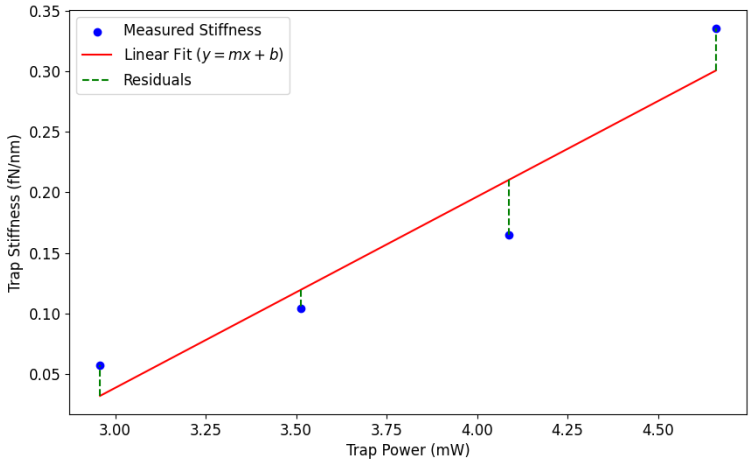

Figure 3.8: Trap stiffness as a function of laser power based on the power spectral density in Au-Ti DI water. A plot of the trap stiffness (blue), linear fit (in red), and the residuals (in green). The slope = 0.15793, R-squared = 0.90711, P-value = 0.04758, standard error = 0.03574.

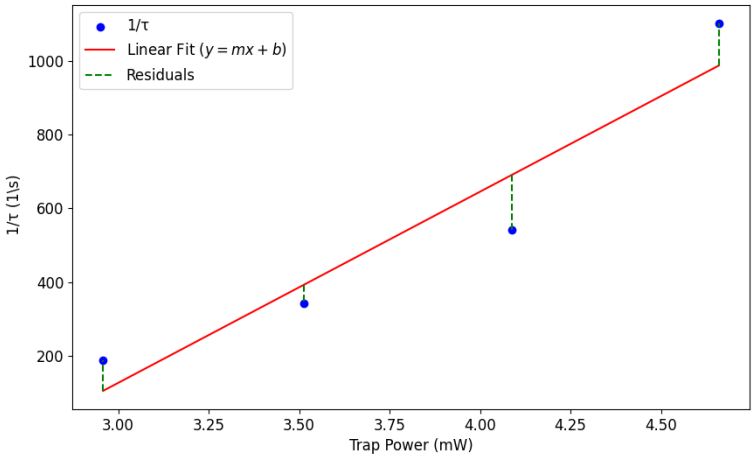

Figure 3.9: Inverse of the time constant as a function of laser power based on the power spectral density in Au-Ti DI water. A plot of the time constant (blue), linear fit (in red), and the residuals (in green). The slope = 518.695, R-squared = 0.90711, P-value = 0.04758, standard error = 117.369.

Laser Current (mA)	Trap Power (mW)	f_c (Hz)	τ (s)	$1/\tau$ (1/s)	κ (fN/nm)
90	2.96	30.0	0.005308	188.384	0.057
100	3.51	54.4	0.002925	341.907	0.104
110	4.09	86.3	0.001843	542.515	0.165
120	4.66	175.4	0.000907	1101.980	0.336

Table 3.1: Summary of trapping results in Au-Ti DI water at varying laser powers.

3.2.2 Silver in DI Water

Trapping of 20 nm polystyrene beads was achieved in silver-titanium (Ag-Ti) DI water samples fabricated with an average DNH gap size of 32.0 nm, as seen in the SEM images shown in Section 2.2.3.2, Figure 2.13. The trapping signal obtained from a Ag-Ti DI water sample at a constant trapping power of 3.51 mW $\pm$ 5% is shown in Figure 3.10a. The laser was turned on at $t = 0$ s, and turned off at $t = 102$ s. Detailed views of the trapping signal at specific time points are provided in Figures 3.10b and 3.10c. The signal in Figure 3.10b was excluded from further analysis since the trap lasted only ≈ 1 second. Therefore, only the signal in Figure 3.10c was analyzed.

Figure 3.11 shows the data analysis steps performed on the signal in Figure 3.10c. Starting with Figure 3.11a, which provides a closer view of the data from Figure 3.10a at $t = 53$ s, the analysis proceeds to Figure 3.11b, where a Savitzky-Golay filter is applied to smooth the signal. Figure 3.11c selects a 5-second interval of the trapped data for PSD estimation. The resulting PSD, with a fitted Lorentzian curve, is shown in Figure 3.11d. The fitted parameters were determined to be $f_c = 107.1 \pm 0.6$ Hz, $\tau = 0.001486 \pm 8.77 \times 10^{-6}$ s, $A = 0.0576 \pm 0.0005$ V^2/s.

Figure 3.12 displays histograms of the trapped signal and a fitted Gaussian probability density function. The analysis yields a mean of $\mu = 1.53$ V, and a standard deviation of $\sigma = 0.03$ V.

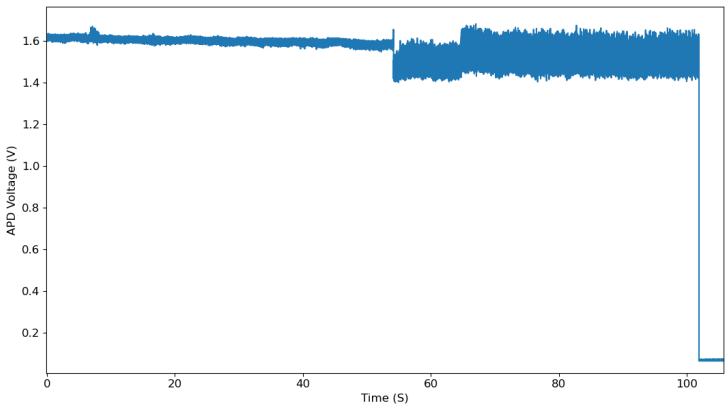

(a) Trapping signal in a Ag-Ti DI water sample. The laser was turned on at $t = 0$ s, and turned off at $t = 102$ s.

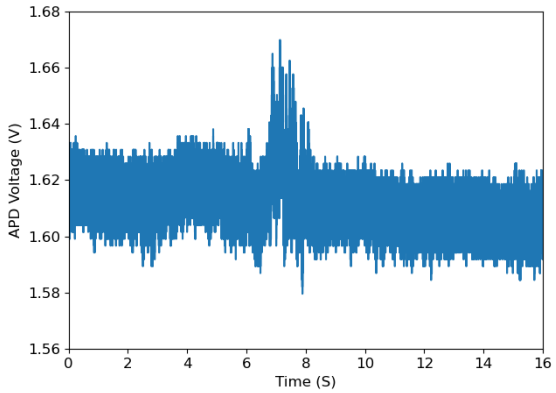

(b) Signal at $t = 8$ s.

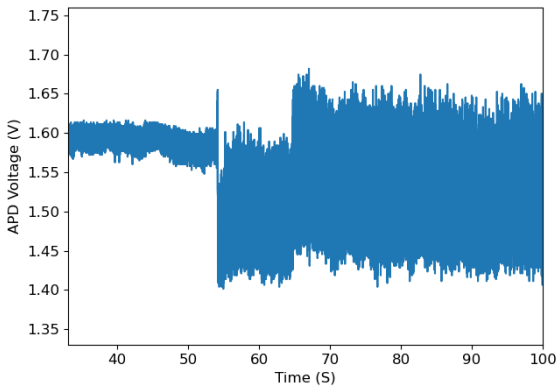

(c) Signal at $t = 53$ s.

Figure 3.10: Trapping signal in Ag-Ti Di water at constant trapping power of 3.51 mW $\pm$ 5% (a), and two zoomed-in views of the signal at two specific times, (b) $t = 8$ s, and (c) $t = 53$ s.

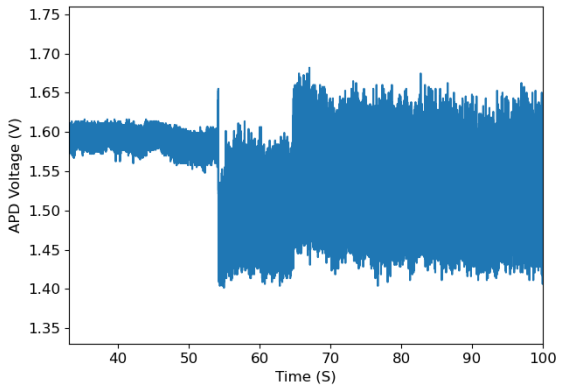

(a) Close-up view from Figure 3.10a.

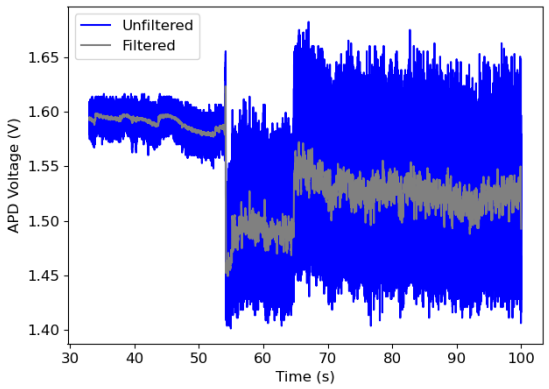

(b) Savitzky-Golay filter.

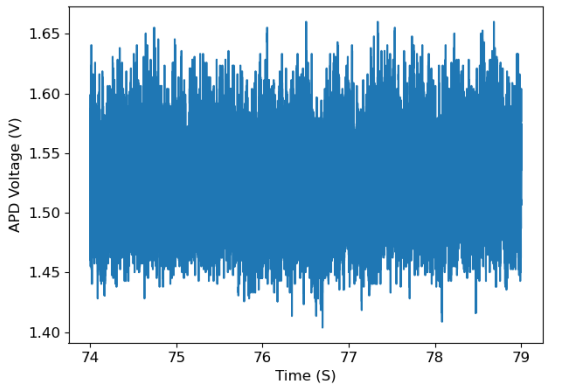

(c) Select 5-seconds of the trapped data.

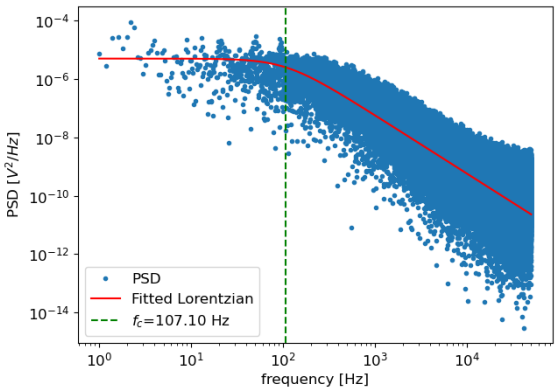

(d) PSD with fitted Lorentzian.

Figure 3.11: Analysis of a trapping event for a 20 nm polystyrene bead in a double nanohole (gap size $\approx$ 32.0 nm) in a Ag-Ti DI water sample. The laser current was constant at 100 mA (trapping power 3.51 mW $\pm$ 5%).

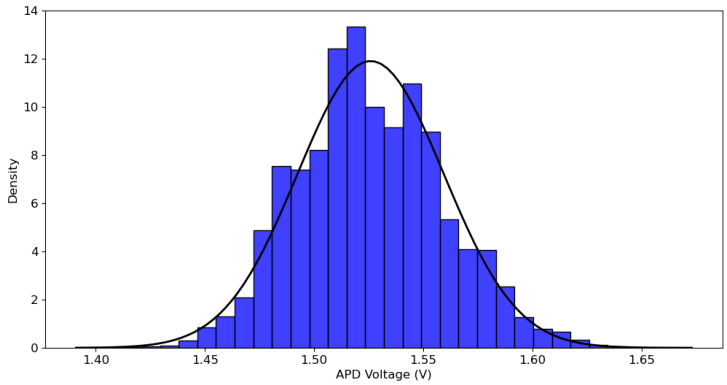

Figure 3.12: Histograms (blue) and Gaussian probability density function (black line) of the trapped signal for Figure 3.11c. The mean is $\mu = 1.53$ V, and standard deviation is $\sigma = 0.03$ V.

When investigating the power dependence of the trap in Figure 3.13, I was unable to trap below 90 mA (or 2.96 mW $\pm$ 5% trapping power). Therefore, I started the trap at 90 mA at $t = 482$ s and increased the laser current in increments of 10 mA while the polystyrene bead was trapped. The laser was then turned off at $t = 559$ s, releasing the particle from the trap. Figure 3.14 shows a zoomed-in section of the trapping signal at 90 mA and applies the Savitzky-Golay filter.

The PSD plots with Lorentzian fits were estimated for each trapping power, as shown in Figure 3.15. The trap stiffness κ and the inverse of time constant τ^{-1} were derived from the Lorentzian fits and plotted as functions of laser power in Figures 3.16, and 3.17, respectively. A linear relationship was found, and the results are summarized in Table 3.2.

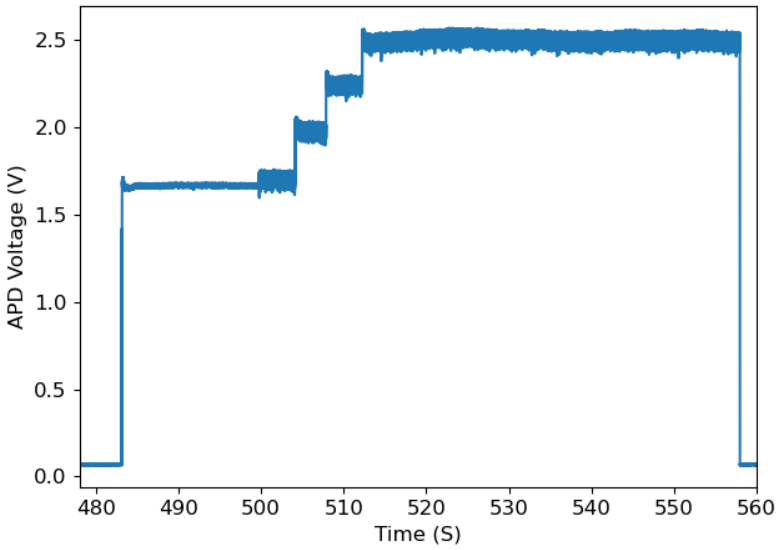

Figure 3.13: Trapping event for different incident trapping laser powers in Ag-Ti DI water. The laser was turned on at $t = 482$ s, with a current 90 mA. The current was then increased in increment of 10 mA during the trap. The laser was turned off at $t = 559$ s.

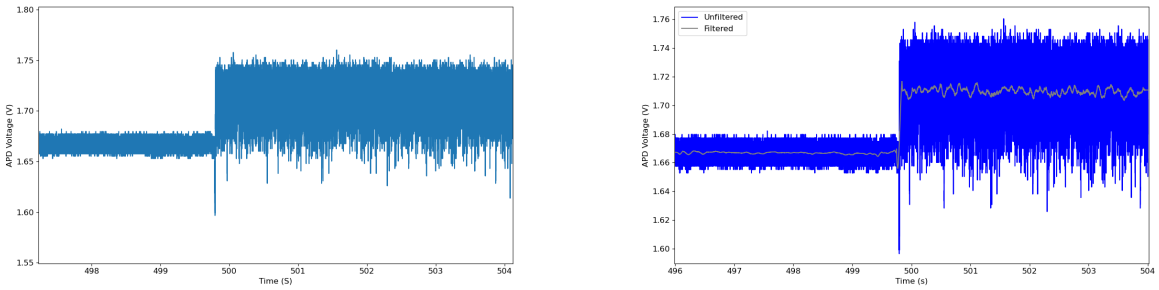

(a) Signal at 90 mA.

(b) Savitzky-Golay filter.

Figure 3.14: Close-up view of the trapping signal at 90 mA (2.96 mW$\pm$5%) from Figure 3.13.

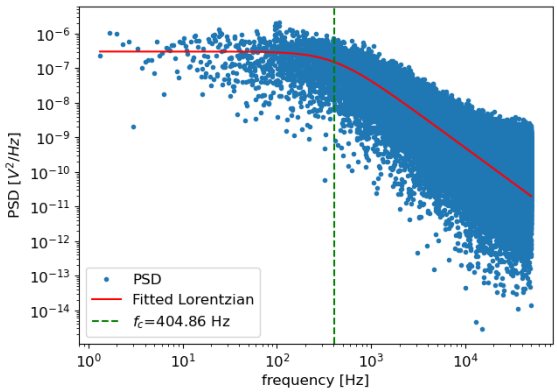

(a) At 90 mA (2.96 mW $\pm$ 5%).

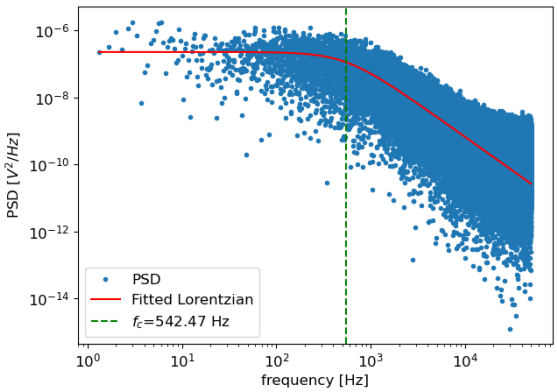

(b) At 100 mA (3.51 mW $\pm$ 5%).

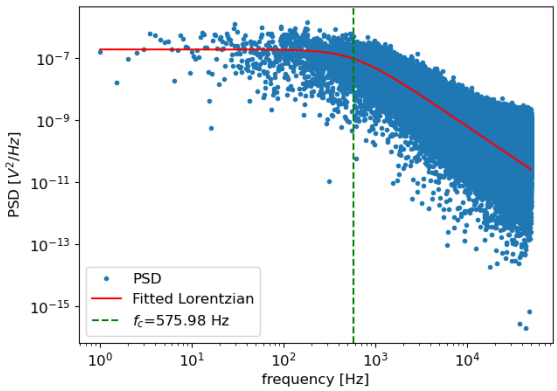

(c) At 110 mA (4.09 mW $\pm$ 5%).

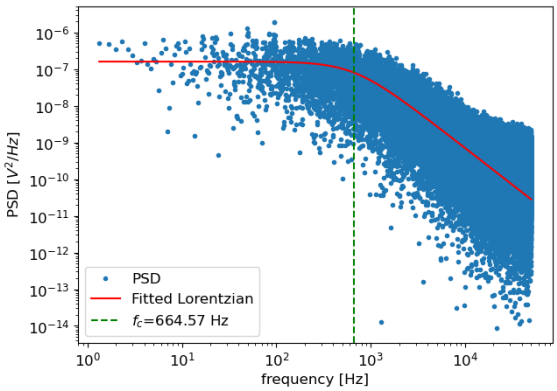

(d) At 120 mA (4.66 mW $\pm$ 5%).

Figure 3.15: The PSD with fitted Lorentzian for different lasers powers in Ag-Ti DI water.

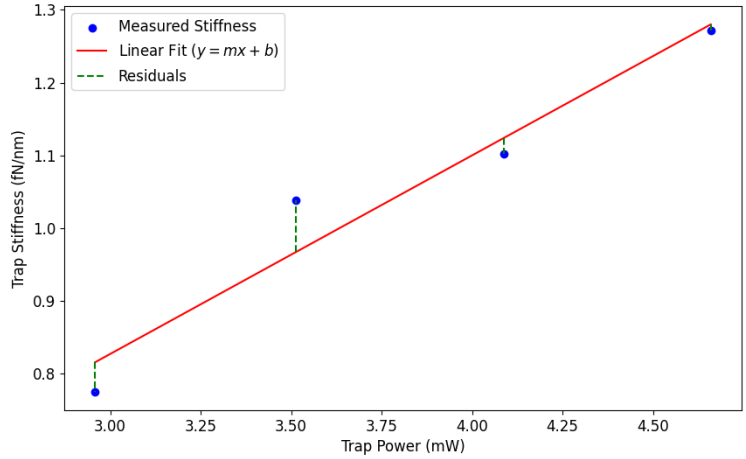

Figure 3.16: Trap stiffness as a function of laser power based on the power spectral density in Ag-Ti DI water. A plot of the trap stiffness (blue), linear fit (in red), and the residuals (in green). The slope = 0.27314, R-squared= 0.94297, P-value = 0.02893, standard error = 0.04750.

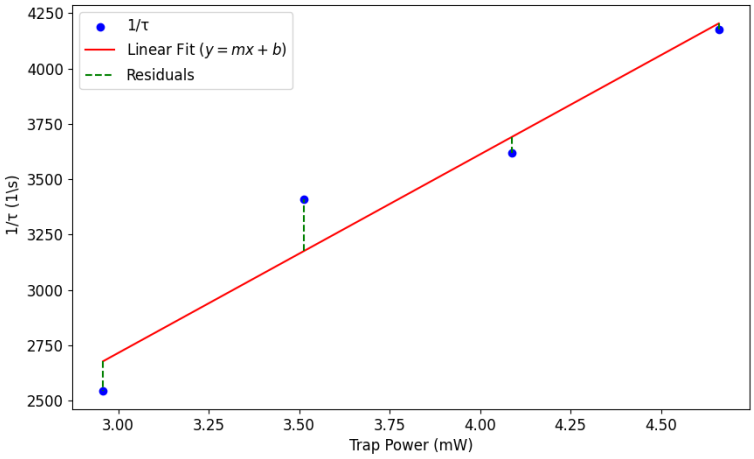

Figure 3.17: Inverse of the time constant as a function of laser power based on the power spectral density in Ag-Ti DI water. A plot of the time constant (blue), linear fit (in red), and the residuals (in green). The slope = 897.099, R-squared = 0.94297, P-value = 0.02893, standard error = 155.996.

Laser Current (mA)	Trap Power (mW)	f_c (Hz)	τ (s)	$1/\tau$ (1/s)	κ (fN/nm)
90	2.96	404.9	0.000393	2543.788	0.775
100	3.51	542.5	0.000293	3408.470	1.038
110	4.09	576.0	0.000276	3618.962	1.102
120	4.66	664.6	0.000239	4175.620	1.271

Table 3.2: Summary of trapping results in Ag-Ti DI water at varying laser powers.

3.2.3 Gold Versus Silver in DI Water

At a constant power (3.51 mW $\pm$ 5%), the results for trapping a 20 nm PS bead in gold and silver nanostructures in DI water are summarized in Table 3.3.

Parameter	Au-Ti in DI water	Ag-Ti in DI water
f_c (Hz)	349.1 ± 1.3	107.1 ± 0.6
τ (s)	$0.000456 \pm 1.71 \times 10^{-6}$	$0.001486 \pm 8.77 \times 10^{-6}$
A (V^2/s)	0.2930 ± 0.0017	0.0576 ± 0.0005

Table 3.3: Comparison of trapping parameters for Au-Ti and Ag-Ti in DI water at constant power (3.51 mW $\pm$ 5%).

Negative traps, characterized by an initial decrease in the signal before it rises, were observed more frequently in silver DNHs compared to gold (see Figure 3.11b). This behaviour may suggest transient release and recapture of particles or fluctuations in the trapping potential.

In a separate experiment, the APD signal was measured while incrementally increasing the laser intensity for a trapped PS bead. The corner frequency, f_c, was recorded at each intensity step, and the summarized results are presented in Table 3.4.

For Au-Ti DI water, the corner frequency showed a significant increase with rising laser power, ranging from $f_c = 30.0$ Hz at 2.96 mW to $f_c = 175.4$ Hz at 4.66 mW. The corresponding trap stiffness (κ) increased from $\kappa = 0.057$ fN/nm to $\kappa = 0.336$ fN/nm, while the time constant (τ) decreased from $\tau = 0.005308$ s to 0.000907 s .

In contrast, Ag-Ti DI water exhibited higher corner frequency values, increasing from $f_c = 404.9$ Hz at 2.96 mW to $f_c = 664.6$ Hz at 4.66 mW. The trap stiffness increased from $\kappa = 0.775$ fN/nm to $\kappa = 1.271$ fN/nm, while the time constant decreased from $\tau = 0.000393$ s to 0.000239 s.

Laser Current (mA)	Trap Power (mW)	Material and Environment	f_c (Hz)	τ (s)	κ (fN/nm)
90	2.96	Au-Ti DI water	30.0	0.005308	0.057
		Ag-Ti DI water	404.9	0.000393	0.775
100	3.51	Au-Ti DI water	54.4	0.002925	0.104
		Ag-Ti DI water	542.5	0.000293	1.038
110	4.09	Au-Ti DI water	86.3	0.001843	0.165
		Ag-Ti DI water	576.0	0.000276	1.102
120	4.66	Au-Ti DI water	175.4	0.000907	0.336
		Ag-Ti DI water	664.6	0.000239	1.271

Table 3.4: Comparison of trapping results for Au-Ti and Ag-Ti in DI water at varying laser powers.

Trapping experiments with Au-Ti DI water demonstrated the capability to maintain a trap with powers as low as 1.90 mW (70 mA). In contrast, the Ag-Ti DI water sample required a minimum power of 2.96 mW (90 mA) for successful trapping. Additionally, as illustrated in Figure 3.6 trapping with powers below 3.51 mW (100 mA) in Au-Ti DI water resulted in an unstable trapping signal. This suggests that while Au-Ti DI water nanostructures can sustain trapping at lower power levels compared to Ag-Ti DI water, maintaining signal stability at these lower power levels is challenging.

3.3 Nanostructures in mPEG Thiol

3.3.1 Gold in mPEG Thiol

Successful trapping of 20 nm PS beads was achieved using Au-Ti nanostructures in mPEG thiol within DNHs of an average gap size of 32.7 nm. SEM images of the Au-Ti mPEG thiol DNHs are presented in Section 2.2.3.1, Figure 2.11. Figure 3.18 shows the full trapping signal for Au-TI mPEG thiol, with the laser turned on at $t = 0$ s and turned off at $t = 175$ s. The trapping laser power was constant at 3.51 mW $\pm$ 5%. A detaieed analysis of this trapping signal is shown in Figure 3.19. Specifically, Figure 3.19a provided a close-up view of the signal from Figure 3.18, indicating the presence of the trapped particle occurs at $t = 8$ s. The Savitzky-Golay filter is applied to the data in Figure 3.19b, aiding in noise reduction and signal smoothing. The selected 5-second interval used for the PSD estimation is shown in Figure 3.19c, with a filtered version presented in Figure 3.19d.

When calculating the PSD and fitting a Lorentzian function, as seen in Figure 3.20, noise contamination was observed near 10^2 Hz. This is due to mechanical noise in the system and

was filtered out prior to fitting by applying a threshold on the y-axis to eliminate values greater than 10^{-5} Hz. Figure 3.20a presents the PSD before applying the threshold, yielding parameters of $f_c = 184.4 \pm 1.3$ Hz, $\tau = 0.000863 \pm 6.11 \times 10^{-6}$ s, and $A = 0.0488 \pm 0.0005$ V^2/s. After applying the noise filter, Figure 3.20b presents refined parameters of $f_c = 195.8 \pm 0.8$ Hz, $\tau = 0.000813 \pm 3.44 \times 10^{-6}$ s, and $A = 0.0482 \pm 0.0003$ V^2/s. This process illustrates the importance of noise filtration for accurate parameter extraction in PSD analysis, which is discussed in more detail in Section 3.4.

Figure 3.21 shows histograms of the trapped data and a fitted Gaussian probability density function. The mean is $\mu = 1.70$ V, and standard deviation is $\sigma = 0.02$ V.

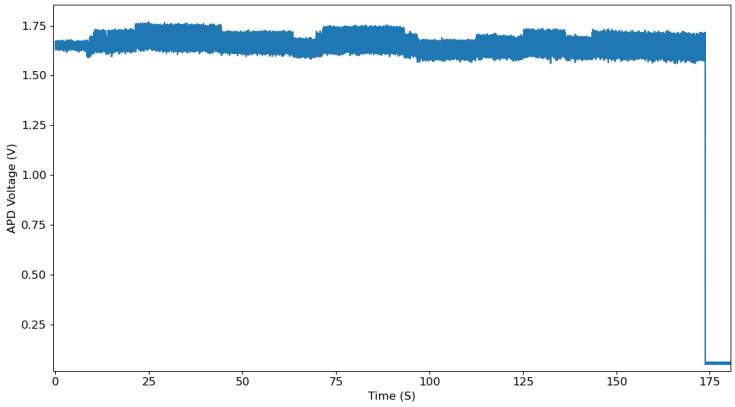

Figure 3.18: Full trapping event in Au-Ti mPEG thiol. The laser was turned on at $t = 0$ s and turned off at $t = 175$ s.

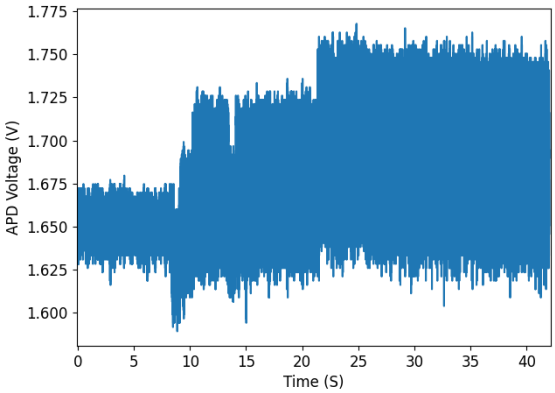

(a) Close-up view from Figure 3.18.

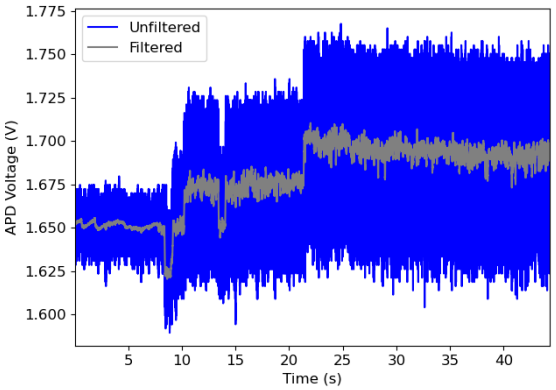

(b) Savitzky-Golay filter.

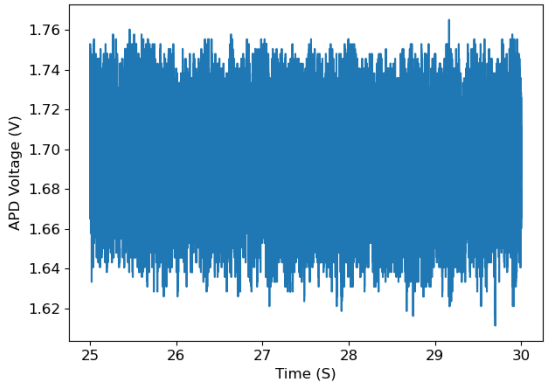

(c) Select 5-seconds of the trapped data.

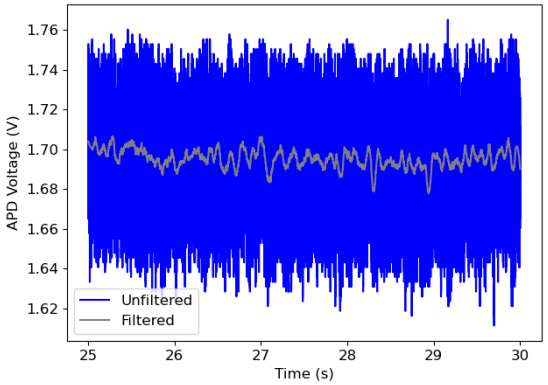

(d) Savitzky-Golay filter on the trapped data.

Figure 3.19: Trapping event of a 20 nm polystyrene bead in a double nanohole of an average gap size of ≈ 32.7 nm in Au-Ti mPEG thiol. The laser current was constant at 100 mA (and trapping power 3.51 mW $\pm$ 5%).

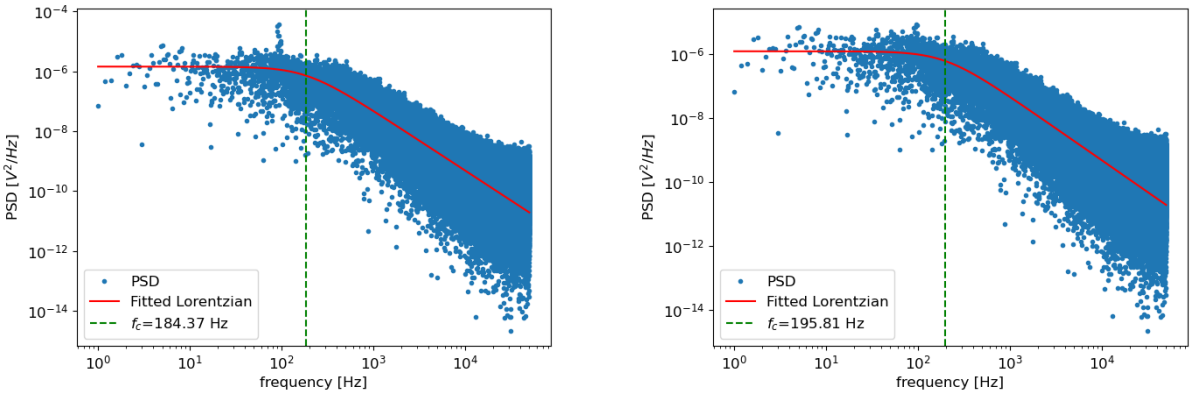

(a) PSD before threshold.

(b) PSD after threshold.

Figure 3.20: Mechanical vibrations observed near $\approx 10^2$ Hz when calculating the PSD and fitting a Lorentzian function from Figure 3.19c in an Au-Ti mPEG thiol sample.

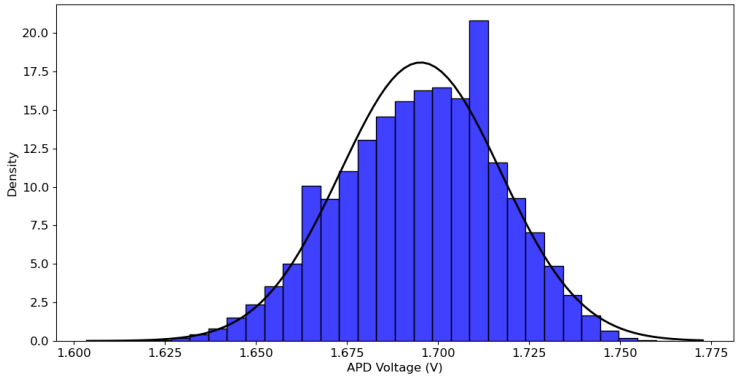

Figure 3.21: Histograms (blue) and Gaussian probability density function (black line) of the trapped signal for Figure 3.19c. The mean is $\mu = 1.70$ V, and standard deviation is $\sigma = 0.02$ V.

A second trapping event is shown in Figure 3.22, with a close-up view in Figure 3.22b, displaying the fluctuation in the trapped signal. This trap was achieved on the same DNH as in Figure 3.18, with the laser turned off at $t = 175$ s and turned on again at $t = 182$ s, resulting in a subsequent trapping event.

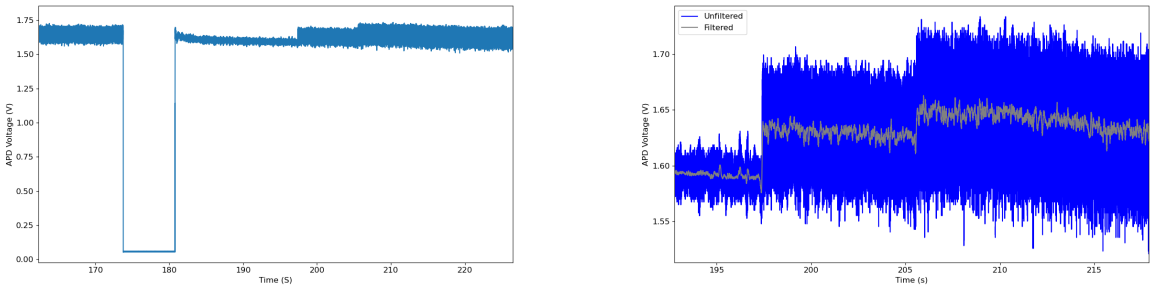

(a) Second trapping signal.

(b) Savitzky-Golay filter.

Figure 3.22: Second trap occurred in Au-Ti mPEG thiol on the same DNH as Figure 3.18, with the laser turned off at $t = 175$ s and turned on again at $t = 182$ s.

To further confirm the signature of the trapping signal in Au-Ti mPEG thiol. I achieve another trap on a different DNH. Figure 3.23 shows the trapping signal when the laser was turned on at $t = 0$ s, and turned off at $t = 107$ s releasing the particle from the trap. Figure 3.24 shows a close-up view of the signal and the steps taken to analyze the trapped data. Unlike the previous trap with the first DNH in Figure 3.20, when calculating the PSD and fitting a Lorentzian in this second DNH, I did not observe a noise contamination near $\approx 10^2 Hz$. The PSD calculation and Lorentzian fitting from Figure 3.25 yielded the following fitted parameters, $f_c = 210.2 \pm 0.8$ Hz, $\tau = 0.000757 \pm 2.90 \times 10^{-6}$ s, $A = 0.1019 \pm 0.0006$ V^2/s. Figure 3.26 shows the histograms of the trapped data with a fitted Gaussian probability density function. The mean is $\mu = 1.84$ V and standard deviation is $\sigma = 0.03$ V.

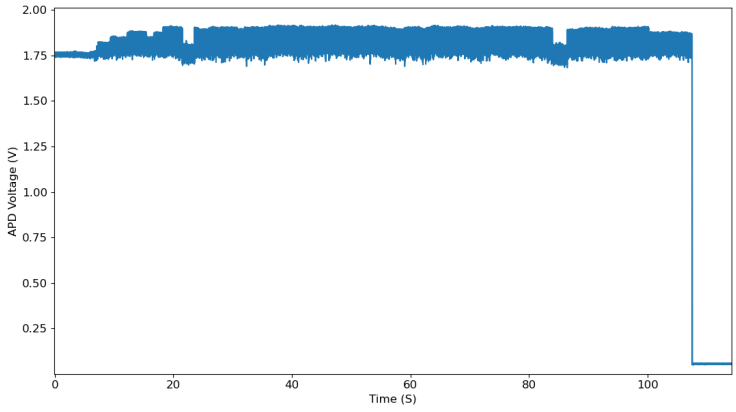

Figure 3.23: Another trap on a second DNH in Au-Ti mPEG thiol. Laser was turned on at $t = 0$ s and then turned off at $t = 107$ s.

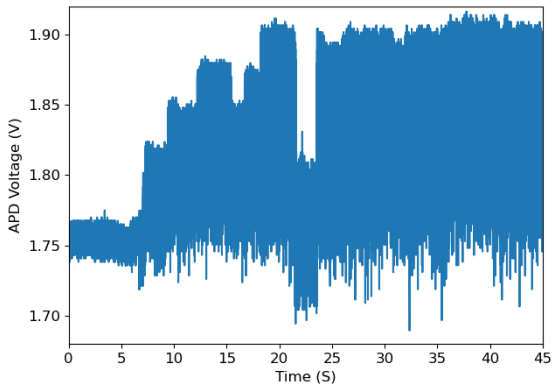

(a) Close-up view from Figure 3.23.

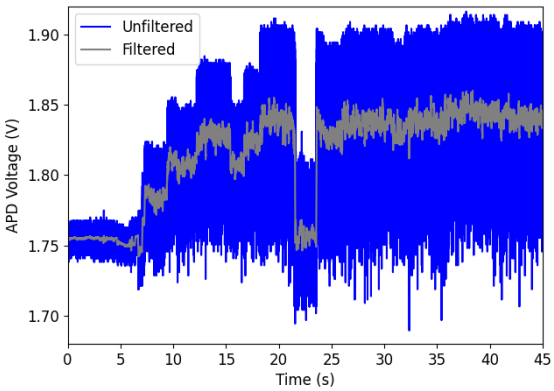

(b) Savitzky-Golay filter.

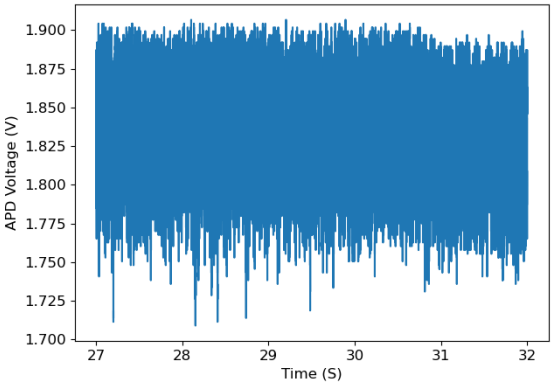

(c) Select 5-seconds of the trapped data.

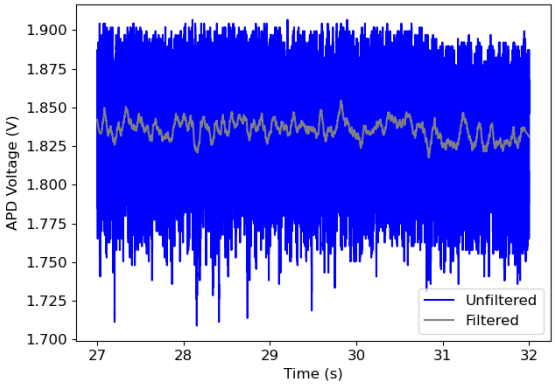

(d) Savitzky-Golay filter of the trapped data.

Figure 3.24: Trapping event of a 20 nm polystyrene bead in a second double nanohole of an average gap size of ≈ 32.7 nm in Au-Ti mPEG thiol. The laser current was constant at 100 mA (trapping power 3.51 mW $\pm$ 5%).

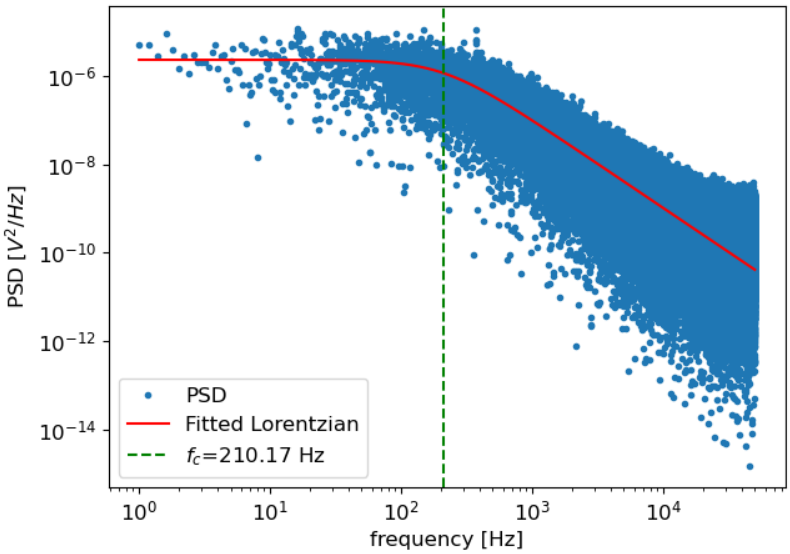

Figure 3.25: The PSD with a fitted Lorentzian for the trapped signal from Figure 3.24c in Au-Ti mPEG thiol.

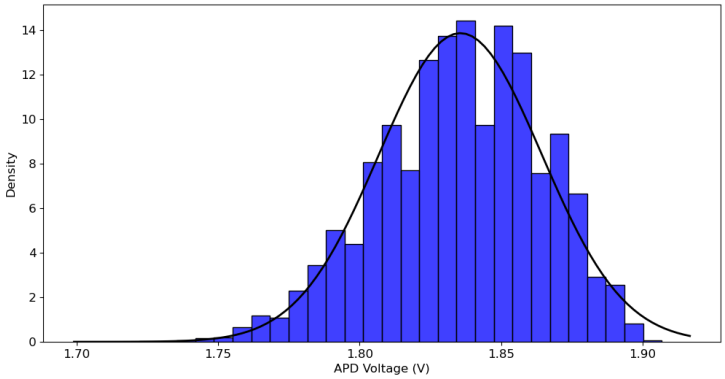

Figure 3.26: Histograms (blue) and Gaussian probability density function (black line) of the trapped signal for Figure 3.24c. The mean is $\mu = 1.84$ V, and standard deviation is $\sigma = 0.03$ V.

Similar to the trapping procedure in the first DNH, I achieved a second trap in the second DNH, as shown in Figure 3.27. The laser was turned off at $t = 107$ s to release the particle and then turned on at $t = 115$ s to re-trap it. This successful re-trapping further confirms the trapping stability of DNHs in the Au-Ti mPEG thiol monolayer.

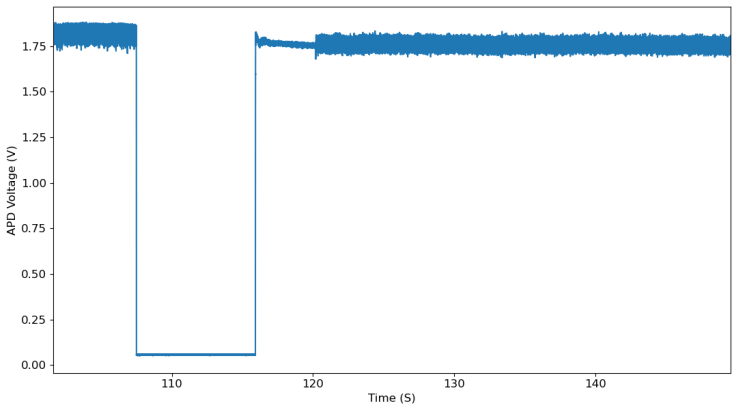

(a) The laser was turned off at $t = 107$ s to untrap the polystyrene bead, and then turned on at $t = 115$ s to trap it for the second time.

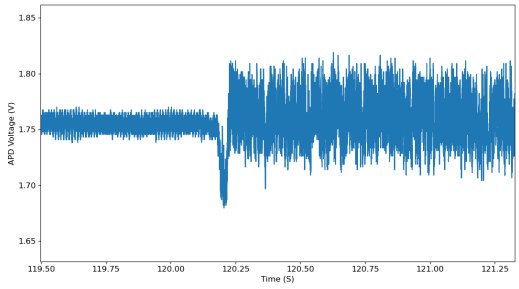

(b) Close-up view of the trap.

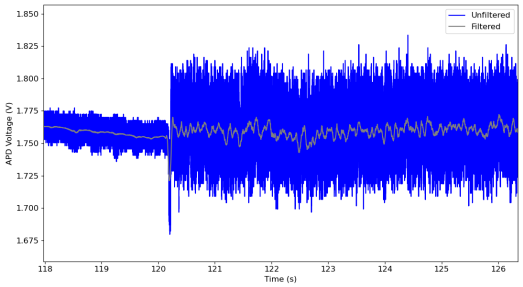

(c) Savitzky-Golay filter applied to the signal.

Figure 3.27: A second trap achieved on a second DNH, same as Figure 3.23, in an Au-Ti mPEG thiol sample.

Figure 3.28 shows the trapping event for different incident trapping laser powers in an Au-Ti mPEG thiol sample, demonstrating the power dependence of the trap. The experiment started at time $t = 0$ s with a laser current of 70 mA (1.90 mW $\pm$ 5% and then incremented the laser current in steps of 10 mA while the particle was getting trapped. The laser was turned off at time $t = 63$ s, releasing the particle from the trap. Figure 3.29 compares the trapping signal when the laser current is set to 70 mA (as shown in Figure 3.29a) and at 100 mA (as shown in Figure 3.29b). This comparison demonstrates that setting the laser current to 100 mA provides a more stable trapping signal.

The PSD with fitted Lorentzian for each trapping power in Au-Ti mPEG thiol is given in Figure 3.30. The trap stiffness as a function of trap power is shown in Figure 3.31, while the inverse of the time constant as a function of trap power is shown in Figure 3.32. A linear relationship is found, suggesting both the trap stiffness and the inverse of time

constant increase with higher laser power, thereby improving the trap's ability to hold the polystyrene bead. The results of trapping in Au-Ti mPEG thiol at increasing laser powers are summarized in Table 3.5.

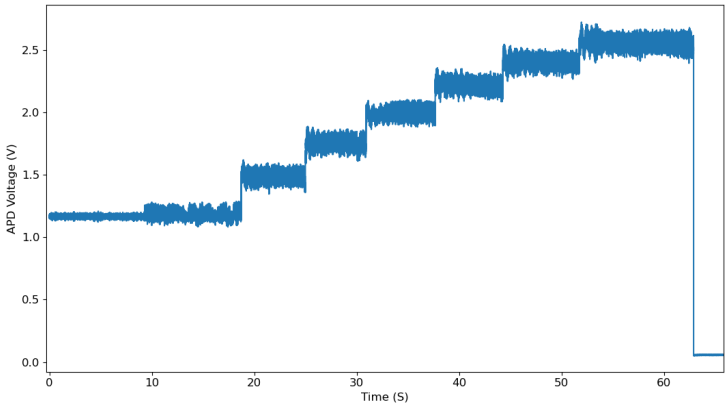

Figure 3.28: Trapping event at different incident trapping laser powers in Au-Ti mPEG thiol. The laser was turned on at $t = 0$ s, with a current of 70 mA. The laser current was then increased in increment of 10 mA during the trap. The laser was turned off at $t = 63$ s.

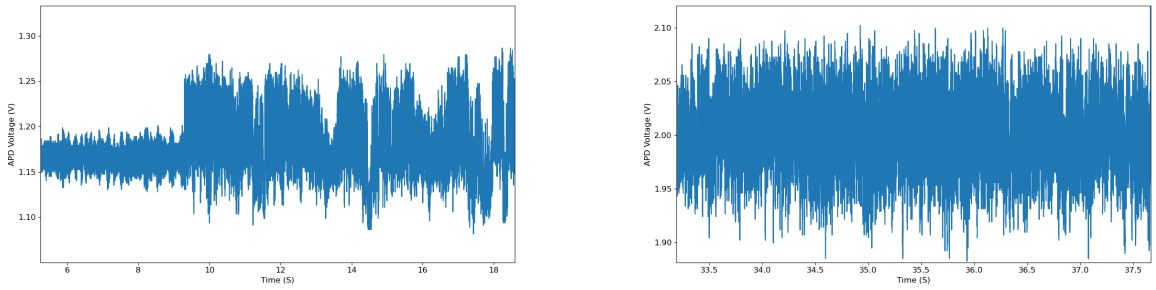

(a) Trapped signal at 70 mA (1.90 mW $\pm$ 5%). (b) Trapped signal at 100 mA (3.51 mW $\pm$ 5%).

Figure 3.29: Comparison of trapping stability at 70 mA and 100 mA in Au-Ti mPEG thiol, demonstrating that a current of 100 mA results is a more stable trapping signal. For the original trapping signal, refer to Figure 3.28.

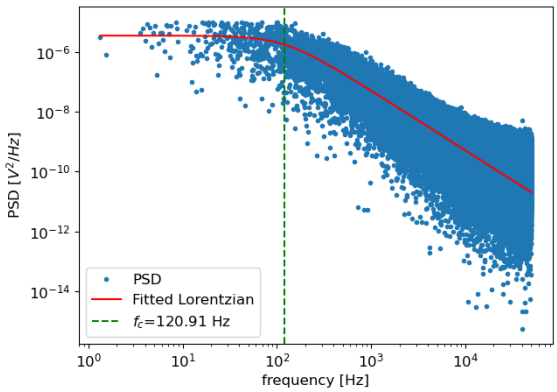

(a) At 90 mA (2.96 mW $\pm$ 5%).

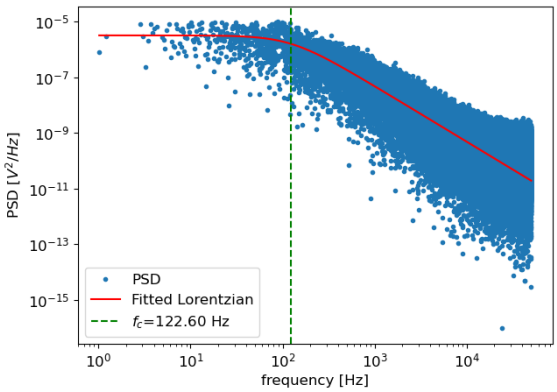

(b) At 100 mA (3.51 mW $\pm$ 5%).

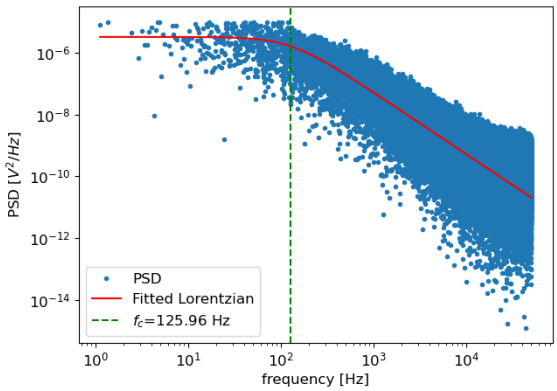

(c) At 110 mA (4.09 mW $\pm$ 5%).

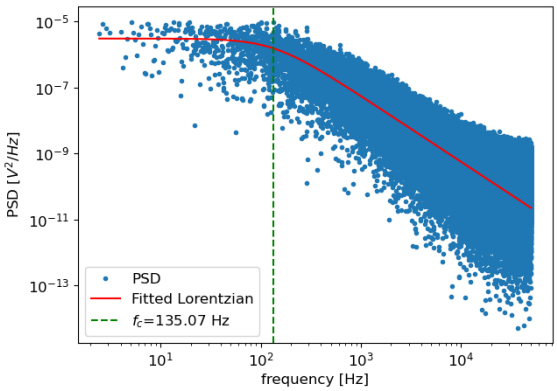

(d) At 120 mA (4.66 mW $\pm$ 5%).

Figure 3.30: The PSD with fitted Lorentzian for different lasers powers in Au-Ti mPEG thiol.

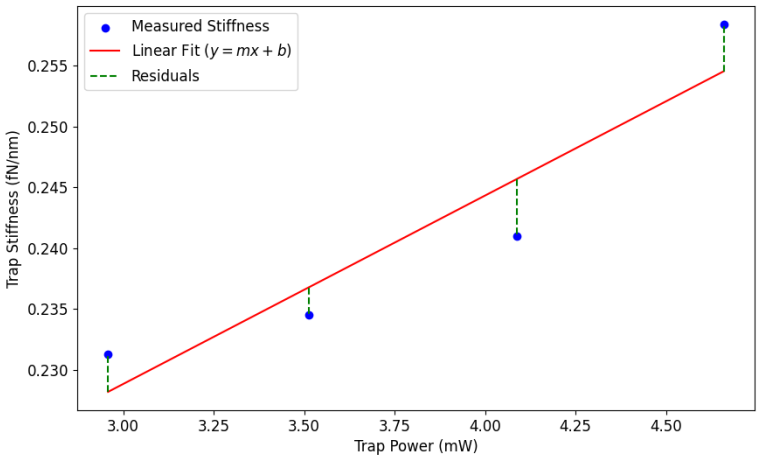

Figure 3.31: Trap stiffness as a function of laser power based on the power spectral density in Au-Ti mPEG thiol. A plot of the trap stiffness (blue), linear fit (in red), and the residuals (in green). The slope = 0.01548, R-squared = 0.88242, P-value = 0.06063, standard error = 0.00400.

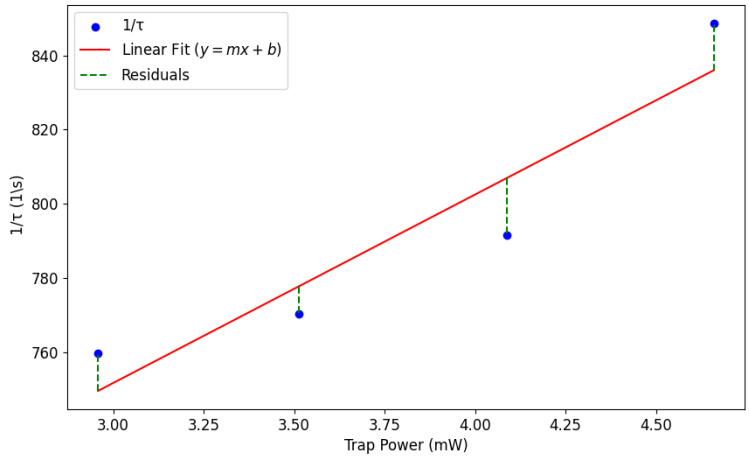

Figure 3.32: Inverse of the time constant as a function of laser power based on the power spectral density in Au-Ti mPEG thiol. A plot of the time constant (blue), linear fit (in red), and the residuals (in green). The slope = 50.8392, R-squared = 0.88242, P-value = 0.06063, standard error = 13.1226.

Laser Current (mA)	Trap Power (mW)	f_c (Hz)	τ (s)	$1/\tau$ (1/s)	κ (fN/nm)
90	2.96	120.9	0.001316	759.669	0.231
100	3.51	122.6	0.001298	770.309	0.235
110	4.09	126.0	0.001263	791.458	0.241
120	4.66	135.1	0.001178	848.673	0.258

Table 3.5: Summary of trapping results in Au-Ti mPEG thiol at varying laser powers.

3.3.2 Silver in mPEG Thiol

Trapping of a 20 nm polystyrene bead was successfully achieved in an Ag-Ti mPEG thiol sample with a DNH of an average gap size of 33.9 nm. The SEM of the DNH structure is shown in Section 2.2.3.2, Figure 2.15. The trapping signal at a constant laser power of 3.51 mW $\pm$ 5% is presented in Figure 3.33, with Figure 3.34 illustrating the steps taken to analysis the trapping signal. Figure 3.34a shows a close-up view of the signal, while Figure 3.34b applies a Savitzky-Golay filter to smooth data and identify noise components. Figure 3.34c show a selected 5-second time interval of the trapped data, used for subsequent PSD analysis. Figure 3.34d shows the same 5-second time interval after applying the Savitzky-Golay filter. The resulting PSD with the fitted Lorentzian function is shown in Figure 3.35 , with fitted parameters of $f_c = 34.0 \pm 0.1$ Hz, $\tau = 0.004680 \pm 1.82 \times 10^{-5}$ s, and $A = 0.0194 \pm 0.0001$ V^2/s. Figure 3.36 shows the histograms of the trapped data, with a fitted Gaussian probability density function. The mean is $\mu = 2.09$ V, and standard deviation is $\sigma = 0.03$ V.

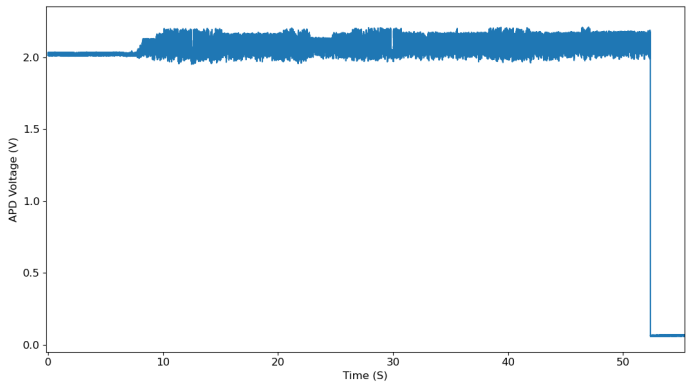

Figure 3.33: Full trapping event in Ag-Ti mPEG thiol. The laser was turned on at $t = 0$ s and then turned off at $t = 53$ s.

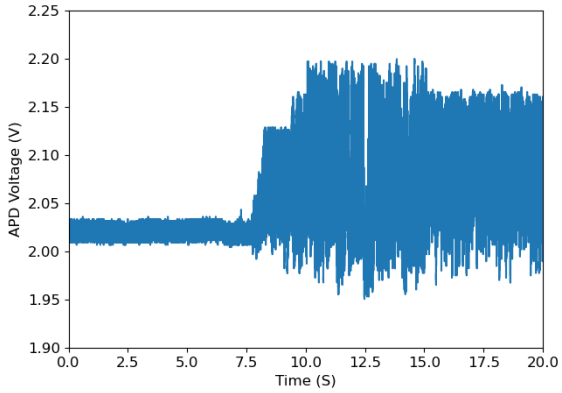

(a) Close-up view from Figure 3.33.

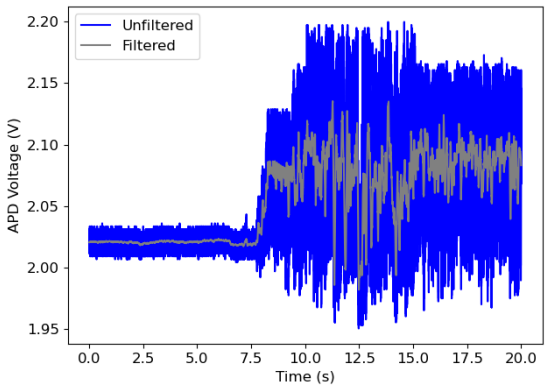

(b) Savitzky-Golay filter.

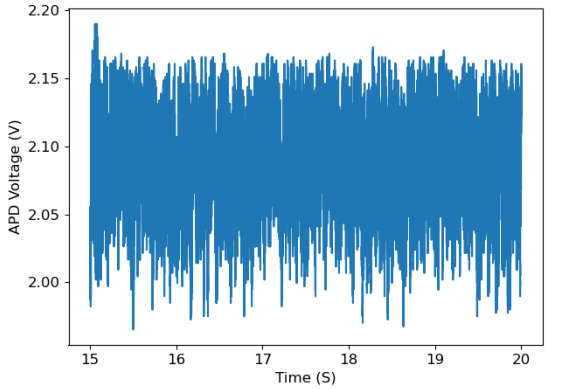

(c) Select 5-seconds of the trapped data.

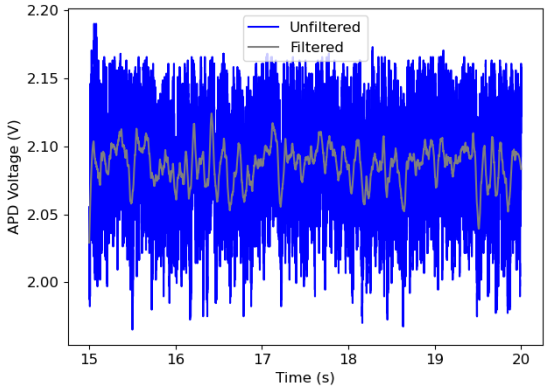

(d) Savitzky-Golay filter on the trapped data.

Figure 3.34: Trapping event of a 20 nm polystyrene bead in a double nanohole of an average gap size of ≈ 33.9 nm in Ag-Ti mPEG thiol. The laser current was constant at 100 mA (and trapping power 3.51 mW $\pm$ 5%).

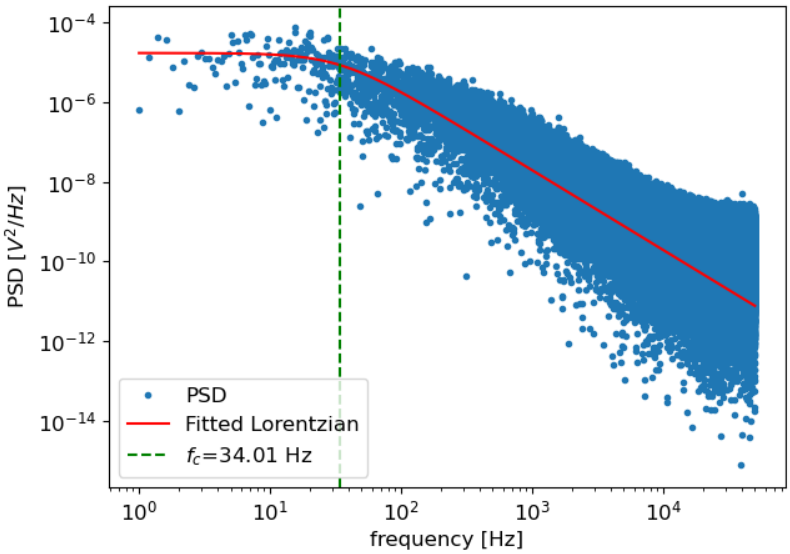

Figure 3.35: The PSD with a fitted Lorentzian for the trapped signal from Figure 3.34c in Ag-Ti mPEG thiol.

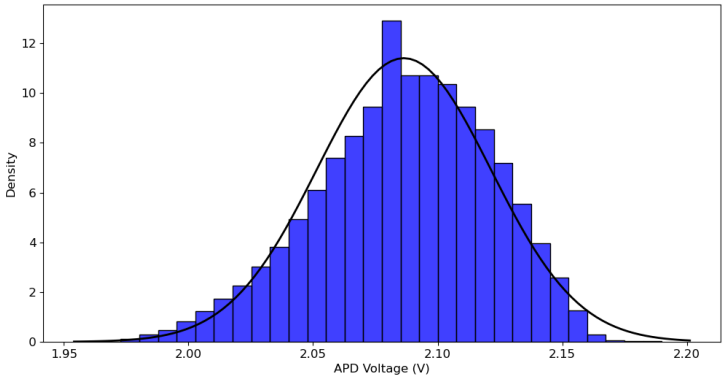

Figure 3.36: Histograms (blue) and Gaussian probability density function (black line) of the trapped signal for Figure 3.34c. The mean is $\mu = 2.09$ V, and standard deviation is $\sigma = 0.03$ V.

A second trapping event is shown in Figure 3.37, achieved using the same DNH as in Figure 3.33. The laser was turned off at $t = 53$ s to release the particle from the trap and then turned on again at $t = 56.5$ s, successfully re-trapping it. This confirm the ability of the DNH in the Ag-Ti mPEG thiol monolayer to reliably to trap 20 nm polystyrene nanospheres.

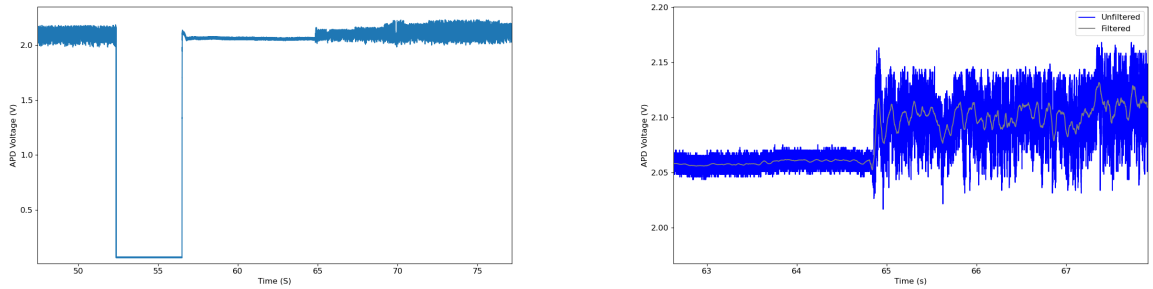

(a) Second trapping signal.

(b) Close-up view with Savitzky-Golay filter.

Figure 3.37: Second trap occurred on the same DNH as Figure 3.33 when turning the laser off at $t = 53$ s and then turning it on shortly after at $t = 56.5$ s.

I investigated the power dependence of the trap, as seen in Figure 3.38. Unlike the case with Ag-Ti DI water (Figure 3.13), trapping was achievable at laser currents below 90 mA (2.96 mW $\pm$ 5%) in the Ag-Ti mPEG thiol sample. The lowest possible trapping power was taken when the laser current was at 80 mA (2.41 mW$\pm$5%). As demonstrated in Figure 3.38, the laser was turned on at $t = 0$ s with a laser current of 80 mA, which was incremented in steps of 10 mA. The laser was turned off at $t = 77$ s after reaching 120 mA, releasing the particle from the trap. The PSD with a fitted Lorentzian for each trapping power is given in Figure 3.39. For consistency, the PSD analysis was limited to data from 90 mA and above. The trap stiffness and the inverse of the time constant as a function of power are plotted in Figures 3.40 and 3.41, respectively. A linear relationship is found, and the results are summarized in Table 3.6.

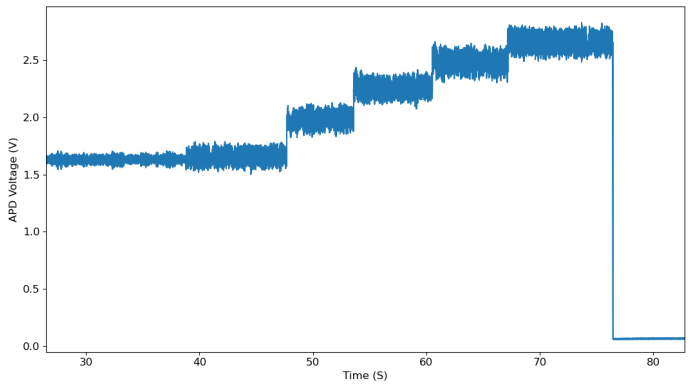

Figure 3.38: Trapping event at different incident laser powers in Ag-Ti mPEG thiol. The laser was turned on at $t = 0$ s, with a current of 80 mA (2.411 mW). the laser current was then increased in increment of 10 mA. The laser was turned off at $t = 77$ s.

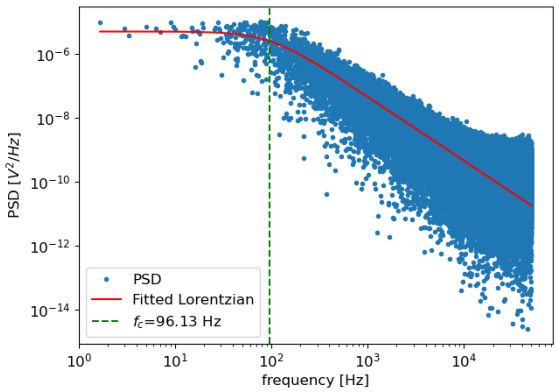

(a) At 90 mA (2.96 mW $\pm$ 5%).

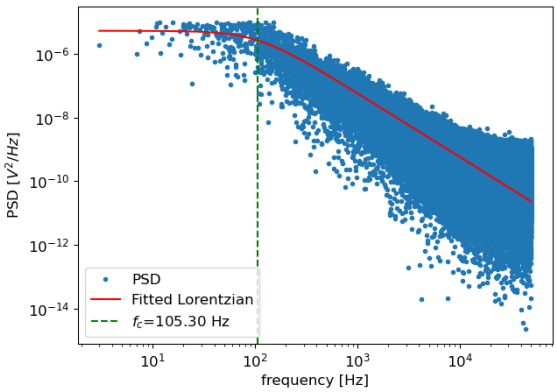

(b) At 100 mA (3.51 mW $\pm$ 5%).

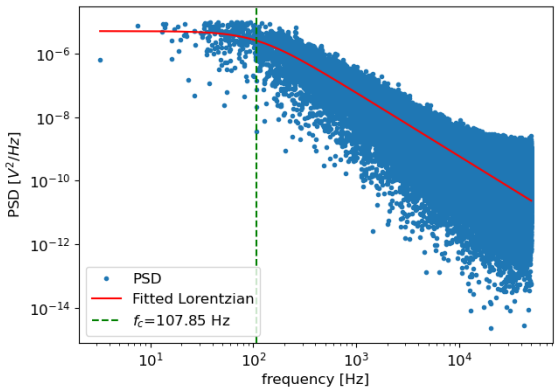

(c) At 110 mW (4.09 mW $\pm$ 5%)

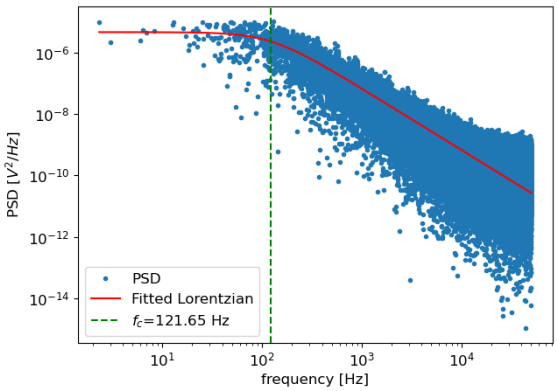

(d) At 120 mA (4.66 mW $\pm$ 5%).

Figure 3.39: The PSD with fitted Lorentzian for different lasers powers in Ag-Ti mPEG thiol.

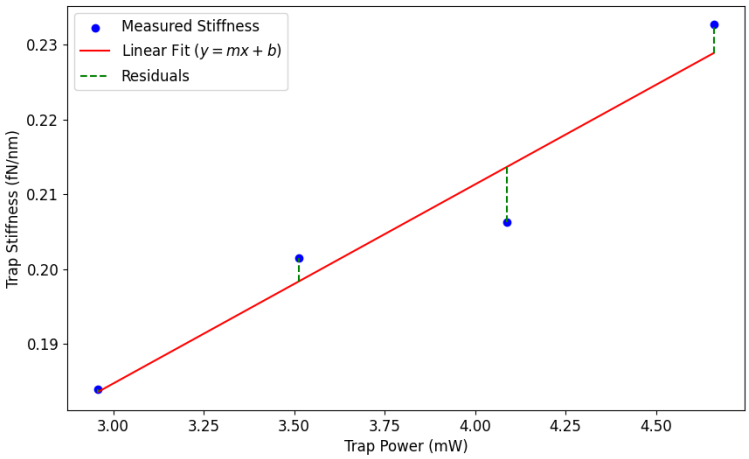

Figure 3.40: Trap stiffness as a function of laser power based on the power spectral density in Ag-Ti mPEG thiol. A plot of the trap stiffness (blue), linear fit (in red), and the residuals (in green). The slope = 0.026646, R-squared = 0.93616, P-value = 0.03245, standard error = 0.00492.

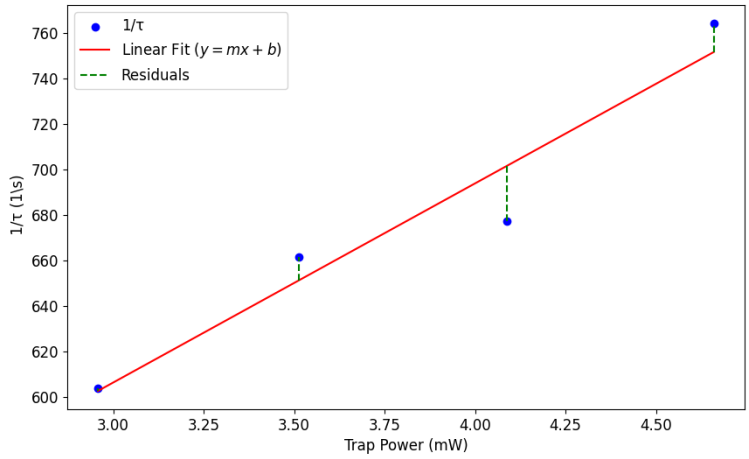

Figure 3.41: Inverse of the time constant as a function of laser power based on the power spectral density in Ag-Ti mPEG thiol. A plot of the time constant (blue), linear fit (in red), and the residuals (in green). The slope = 87.5136, R-squared = 0.9361560, P-value = 0.03245, standard error = 16.1598.

Laser Current (mA)	Trap Power (mW)	f_c (Hz)	τ (s)	$1/\tau$ (1/s)	κ (fN/nm)
90	2.958	96.1	0.001656	603.972	0.184
100	3.512	105.3	0.001511	661.627	0.201
110	4.087	107.9	0.001476	677.617	0.206
120	4.66	121.7	0.001308	764.365	0.233

Table 3.6: Summary of trapping results in Ag-Ti DI mPEG thiol at varying laser powers.

3.3.3 Gold Versus Silver in mPEG Thiol

The results for trapping a 20 nm polystyrene bead in gold and silver within the mPEG thiol monolayer at a constant laser trapping power of 3.51 mW $\pm 5\%$ are summarized in Table 3.7.

Parameter	Au-Ti in mPEG thiol	Ag-Ti in mPEG thiol
f_c (Hz)	210.2 ± 0.8	34.0 ± 0.1
τ (s)	$0.000757 \pm 2.90 \times 10^{-6}$,	$0.004680 \pm 1.82 \times 10^{-5}$
A (V^2/s)	0.1019 ± 0.0006	0.0194 ± 0.0001

Table 3.7: Comparison of trapping parameters for Au-Ti and Ag-Ti in mPEG thiol at constant power (3.512 mW).

The trapping signal exhibited a step-like behavior in Au-Ti mPEG thiol, as seen in Figures 3.19b, 3.22b, 3.24b. This behaviour could be attributed to interactions between the trapped particle and the surface or the particle is becoming temporarily immobilized before being released.

The power dependence of the trap was further investigated by incrementally increasing the incident laser power while the nanoparticle remained trapped. The findings are summarized in Table 3.8.

For Au-Ti mPEG thiol, the corner frequency increased from $f_c = 120.91$ Hz at 2.985 mW to $f_c = 135.07$ Hz at 4.66 mW. The trap stiffness increased from $\kappa = 0.23130$ fN/nm at 2.985 mW to $\kappa = 0.25840$ fN/nm at 4.66 mW, while the time constant decreased from $\tau = 0.001316$ s to $\tau = 0.001178$ s. Similarly, Ag-Ti mPEG thiol also showed an increase in trap stiffness. The corner frequencies increased from $f_c = 96.13$ Hz at 2.985 mW to $f_c = 121.65$ Hz at 4.66 mW. Trap stiffness increased from $\kappa = 0.18389$ fN/nm at 2.958 mW to $\kappa = 0.23272$ fN/nm at 4.66 mW, while the time constant decreased from $\kappa = 0.001656$ s to $\kappa = 0.001308$ s. Although both systems showed a notable increase in trap stiffness with

higher laser, the overall stiffness values were lower in Ag-Ti mPEG thiol compared to Au-Ti mPEG thiol.

Unlike in Au-Ti mPEG thiol, where trapping was achievable at 70 mA (1.901 mW), trapping in Ag-Ti mPEG thiol. was not possible below 80 mA (2.411 mW). However, as shown in Figure 3.29, trapping at 100 mA (3.512 mW) produced a more stable signal compared to 70 mA (1.90 mW) .

Laser Current (mA)	Trap Power (mW)	Material and Environment	f_c (Hz)	τ (s)	κ (fN/nm)
90	2.96	Au-Ti mPEG thiol	120.9	0.001316	0.231
		Ag-Ti mPEG thiol	96.1	0.001656	0.184
100	3.51	Au-Ti mPEG thiol	122.6	0.001298	0.235
		Ag-Ti mPEG thiol	105.3	0.001511	0.201
110	4.09	Au-Ti mPEG thiol	126.0	0.001263	0.241
		Ag-Ti mPEG thiol	107.9	0.001476	0.206
120	4.66	Au-Ti mPEG thiol	135.1	0.001178	0.258
		Ag-Ti mPEG thiol	121.7	0.001308	0.233

Table 3.8: Comparison of trapping results for Au-Ti and Ag-Ti in mPEG thiol at varying laser powers.

3.4 Comparisons

The primary objective of this thesis was to investigate the effectiveness of silver nanostructures in trapping nanoparticles compared to gold nanostructures. This section compares and discusses the experimental results obtained for trapping 20 nm polystyrene (PS) beads in DNH structures fabricated using colloidal lithography in four different environments: Au-Ti DI water, Au-Ti mPEG thiol, Ag-Ti DI water, Ag-Ti mPEG thiol. The key findings include the trapping dynamics, power dependence, and comparisons of trap characteristics across these environments.

The transmission through the DNH aperture is related to the position of the nanoparticle in the aperture, and the Brownian motion fluctuation of this transmission can be used to calculate the trap stiffness. The values of trap stiffness were found using power spectrum density analysis in this work. A linear dependence of the time decay and the trap stiffness as a function of the laser powers was found due to the increase in the strength of the trapping potential. This has been shown for conventional optical tweezers [63].

Tables 3.4 and 3.8 compared the trapping results and the trap stiffness calculations for the four environments. For 4.66 mW (120 mA) incident laser power, the Ag-Ti DI water exhibited higher corner frequency values and consequently higher trap stiffness across all systems indicating stronger force. The trap stiffness was calculated to be around 1.271 fN/nm, while the Au-Ti DI water was 0.336 fN/nm for the same laser power. For Ag-Ti mPEG thiol, the trap stiffness resulted in a lower trap stiffness value of 0.233 fN/nm, while the Au-Ti mPEG thiol gave a value of 0.258 fN/nm.

Even though it is known that silver tarnishes when exposed to air, it was observed that both Ag-Ti DI water and Ag-Ti mPEG thiol maintained their trapping capability for up to 7 days following fabrication. This finding supports the potential use of silver in long-term experiments or applications where repeated use is necessary.

In Sections 3.2.3 and 3.3.3, I presented a comparison of the results from two separate experiments. First, I trapped the PS bead in a DNH at a constant laser power. I obtained the trapping signal, estimated the PSD, fitted a Lorentzian, and extracted the corner frequency. In the second experiment with a different DNH, the signal was measured as the laser intensity was incrementally increased for the trapped particle. This approach led to multiple trapping events at each power. For each trapping laser power, the PSDs were estimated, Lorentzian fits were applied, and the corner frequencies were extracted.

However, the two measurements gave different corner frequency values for the same system. For instance, in Au-Ti DI water while increasing the laser power during the trap, I obtained a value of $f_c = 54.4$ Hz at 100 mA (3.51 mW). In contrast, at a constant power, the value was $f_c = 349.1$ Hz. This discrepancy could be attributed to experimental artifacts. The samples were fabricated on day 1, SEM images were taken on day 2, and then the trapping experiments were conducted over the subsequent five days. The laser power was measured only once, on day 2, before the trapping experiments as was shown in Section 2.4, Figure 2.19. and Table 2.1. Additionally, environmental influences may have caused misalignment in the optical tweezer setup.

Occasionally, large external noise, such as mechanical vibrations, was detected when calculating the PSD. The noise appeared in all four systems and consistently manifested as a peak near 100 Hz. This peak was filtered out prior to fitting a Lorentzian and extracting the corner frequency. Similar mechanical noise have been reported in other works, including those by [64] and [65], where the noise peak was also removed prior to fitting.

In comparison to the trap stiffness calculation for trapping 20 nm PS nanospheres using a DNH optical tweezer, as found by previous group members [40], the authors measured the dynamics of 20 nm PS nanoparticles in a DNH trap to determine the trap stiffness at various

laser powers. The DNHs were fabricated using a focused ion beam (FIB) on commercially available gold metal coated test slides (EMF Corp.) with a 5 nm Ti adhesion layer followed by 100 nm gold layer. The DNHs had a gap of $\approx$ 28 nm. They used a modified Thorlabs optical tweezer kit (OTKB) with a silicon avalanche photodiode (APD, bandwidth 50 MHz) and 820 nm laser diode (Sacher Lasertechnik) to focus onto the DNH using a 100$\times$ oil immersion objective (1.25 numerical aperture) with polarization aligned along the axis of the DNH gap using a half-wave plate for maximum transmission through the DNH. Then, the trapping data was analyzed using the autocorrelation analysis of Brownian fluctuations and the trapping transient analysis. They found a trap stiffness value of around $\kappa \approx 0.2$ fN/nm for 2 mW of power with the stiffness increasing linearly with laser power.

In this thesis, I fabricated the DNHs using colloidal lithography as was shown in Section 2.1. I sputtered 7 nm Ti followed by 70 nm gold or silver layer on a plain microscope slide (Fisherbrand, $25\times75\times1$ mm). The DNHs had a gap size average of 32 nm as was shown in Section 2.2.3. Section 2.4 showed the optical tweezer setup. I used a modified Thorlabs optical tweezer kit (OTKB) with a silicon avalanche photodetector (Thorlabs APD110A) with similar bandwidth to reference [40]. However, the laser used in this thesis was 852 nm laser diode (eagleyard) to focus on the DNH using the objective. I analyzed the data using the power spectrum density theory of the Brownian motion. In the case of Au-TI DI water environment, the trap stiffness value increased linearly with laser power from $\kappa = 0.057$ to 0.336 fN/nm which is within range of the predicted values of reference [40].

Gold DNHs have only been previously used for optical trapping. In this work, I demonstrated the feasibility of creating silver DNH substrates for trapping PS nanospheres. I successfully trapped the nanoparticles and measured the trap stiffness up to 7 days post-fabrication, thereby assessing their usefulness for plasmonic applications, such as plasmonic antennas and circuits for concentrating and guiding light. Silver-based nanostructures have consistently shown superior performance compared to Au-based counterparts in the literature as was discussed in Section 1.6.

Chapter 4

Conclusion and Outlook

This thesis investigated the optical trapping capability of silver and gold nanostructures, for trapping 20 nm polystyrene (PS) beads on double nanohole (DNH) apertures across different environments: Au-Ti DI water, Au-Ti mPEG thiol, Ag-Ti DI water, and Ag-Ti mPEG thiol. The primary objective was to assess the effectiveness of Ag nanostructures in comparison to Au, evaluating parameters such as trap stiffness, corner frequency, and time constant under varying laser powers.

I successfully fabricated the Au and Ag DNH apertures using colloidal lithography. SEM imaging of the apertures showed an average gap size of $\approx$ 32 nm. I was able to trap 20 nm PS nanospheres in all tested materials and environments. The Ag-Ti DI water environment exhibited a higher corner frequency value of 664.6 Hz and consequently trap stiffness of 1.271 fN/nm at 4.66 mW $\pm$ 5%, compared to 175.4 Hz and 0.336 fN/nm in Au-Ti DI water. The surrounding medium might have influenced trapping performance, with mPEG thiol environments resulting in lower trap stiffness for both gold and silver. A linear relationship between trap stiffness and laser power was observed, indicating that increasing power enhances trapping strength resulting in a large optical force holding the particle in the trap. Silver provides a strong optical response and is low-cost. In this thesis, I showed that trapping PS nanospheres on both Au and Ag DNHs was achievable up to 7 days post-fabrication, indicating the potential of using silver nanostructures for large-scale applications.

There are limitations faced when conducting this study. The laser power was measured only once on day 2 of the experiment. Environmental influences may have caused misalignment in the optical tweezer setup, and mechanical vibrations were occasionally detected when calculating the PSD. The data acquisition system used also had a limited frequency resolution of 100 kHz. A faster sampling rate will improve the dynamic response of the trapped signal. Frequent calibration of laser power, addressing vibration and environmental

factors could likewise lead to a better understanding of the experimental outcomes.

Several future experiments could further improve the DNH optical tweezer system as a tool for nanoparticles trapping. Integrating a spectrometer into the optical tweezer setup would enable the measurement of the nanoparticle spectrum during trapping. Analyzing recorded videos of nanoparticle movement within the DNH could help trace the movement of the nanoparticle within the trap and quantify the motion dynamics. Using techniques such as atomic force microscopy (AFM) to visualize and measure the thickness of the monolayer formed on the surfaces of both Au and Ag, would also be valuable. Additionally, investigating other materials with plasmonic properties, such as aluminum (Al), copper (Cu), or magnesium (Mg) could reveal new opportunities for optimizing trapping performance and exploring different plasmonic responses.

Bibliography

[1] Ashkin, A. Acceleration and Trapping of Particles by Radiation Pressure. *Physical review letters* **24**, 156–159 (1970).

[2] Ashkin, A. & Dziedzic, J. M. Optical Levitation by Radiation Pressure. *Applied Physics Letters* **19**, 283–285 (1971).

[3] Ashkin, A. & Dziedzic, J. M. Optical Levitation of Liquid Drops by Radiation Pressure. *Science* **187**, 1073–1075 (1975).

[4] Ashkin, A. Trapping of Atoms by Resonance Radiation Pressure. *Phys. Rev. Lett.* **40**, 729–732 (1978).

[5] Ashkin, A., Dziedzic, J. M., Bjorkholm, J. E. & Chu, S. Observation of a single-beam gradient force optical trap for dielectric particles. *Opt. Lett.* **11**, 288–290 (1986).

[6] Ashkin, A. History of optical trapping and manipulation of small-neutral particle, atoms, and molecules. *IEEE journal of selected topics in quantum electronics* **6**, 841–856 (2000).

[7] Grier, D. G. A revolution in optical manipulation. *Nature (London)* **424**, 810–816 (2003).

[8] Neuman, K. C. & Block, S. M. Optical trapping. *Review of Scientific Instruments* **75**, 2787–2809 (2004).

[9] Harada, Y. & Asakura, T. Radiation forces on a dielectric sphere in the Rayleigh scattering regime. *Optics Communications* **124**, 529–541 (1996).

[10] Jackson, J. D. *Classical electrodynamics* (Wiley, New York, 1975 - 1975), 2d ed. edn.

[11] Wordemann, M. *Structured Light Fields: Applications in Optical Trapping, Manipulation, and Organisation*. Springer Theses (Springer-Verlag, Berlin, Heidelberg, 2012), 1. aufl. edn.

[12] Yang, A. H. J., Lerdsuchatawanich, T. & Erickson, D. Forces and Transport Velocities for a Particle in a Slot Waveguide. *Nano letters* **9**, 1182–1188 (2009).

[13] Saleh, A. A. E. & Dionne, J. A. Toward Efficient Optical Trapping of Sub-10-nm Particles with Coaxial Plasmonic Apertures. *Nano letters* **12**, 5581–5586 (2012).

[14] Nieminen, T. A., Knöner, G., Heckenberg, N. R. & Rubinsztein-Dunlop, H. Physics of Optical Tweezers. In *Methods in Cell Biology*, vol. 82 of *Methods in Cell Biology*, 207–236 (Elsevier Science & Technology, SAN DIEGO, 2007).

[15] Bethe, H. A. Theory of Diffraction by Small Holes. *Physical review* **66**, 163–182 (1944).

[16] Bergeron, J., Zehtabi-Oskuie, A., Ghaffari, S., Pang, Y. & Gordon, R. Optical Trapping of Nanoparticles. *Journal of visualized experiments* e4424– (2013).

[17] Wei, H. & Xu, H. Plasmonics in composite nanostructures. *Materials Today* **17**, 372–380 (2014).

[18] Maier, S. A. *Plasmonics: fundamentals and applications* (Springer, New York, 2007), 1st ed. 2007. edn.

[19] Kelly, K. L., Coronado, E., Zhao, L. L. & Schatz, G. C. The Optical Properties of Metal Nanoparticles: The Influence of Size, Shape, and Dielectric Environment. *The Journal of Physical Chemistry B* **107**, 668–677 (2003).

[20] Le Ru, E. C. & Etchegoin, P. G. P. G. *Principles of surface-enhanced Raman spectroscopy: and related plasmonic effects* (Elsevier, Amsterdam;, 2009), 1st ed. edn.

[21] Rycenga, M. *et al.* Controlling the Synthesis and Assembly of Silver Nanostructures for Plasmonic Applications. *Chemical reviews* **111**, 3669–3712 (2011).

[22] Chen, Y. & Ming, H. Review of surface plasmon resonance and localized surface plasmon resonance sensor. *Photonic sensors (Berlin)* **2**, 37–49 (2012).

[23] Khademi, A., Dewolf, T. & Gordon, R. Quantum plasmonic epsilon near zero: field enhancement and cloaking. *Opt. Express* **26**, 15656–15664 (2018).

[24] Novotny, L., Bian, R. X. & Xie, X. S. Theory of Nanometric Optical Tweezers. *Phys. Rev. Lett.* **79**, 645–648 (1997).

[25] Okamoto, K. & Kawata, S. Radiation Force Exerted on Subwavelength Particles near a Nanoaperture. *Phys. Rev. Lett.* **83**, 4534–4537 (1999).

[26] Quidant, R., Juan, M. L., Gordon, R., Pang, Y. & Eftekhari, F. Self-induced back-action optical trapping of dielectric nanoparticles. *Nature physics* **5**, 915–919 (2009).

[27] Kwak, E.-S. *et al.* Optical Trapping with Integrated Near-Field Apertures. *The journal of physical chemistry. B* **108**, 13607–13612 (2004).

[28] Gordon, R. & Brolo, A. G. Increased cut-off wavelength for a subwavelength hole in a real metal. *Opt. Express* **13**, 1933–1938 (2005).

[29] Gordon, R., Kumar, L. & Brolo, A. Resonant light transmission through a nanohole in a metal film. *IEEE transactions on nanotechnology* **5**, 291–294 (2006).

[30] Kumar, L., Lesuffleur, A., Hughes, M. & Gordon, R. Double nanohole apex-enhanced transmission in metal films. *Applied physics. B, Lasers and optics* **84**, 25–28 (2006).

[31] Kumar, L. & Gordon, R. Localized field enhancement in metal films using an overlapping double-hole nanostructure. In *2006 Conference on Lasers and Electro-Optics and 2006 Quantum Electronics and Laser Science Conference*, 1–2 (IEEE, 2006).

[32] Onuta, T.-D., Waegele, M., DuFort, C. C., Schaich, W. L. & Dragnea, B. Optical Field Enhancement at Cusps between Adjacent Nanoapertures. *Nano letters* **7**, 557–564 (2007).

[33] Pang, Y. & Gordon, R. Optical Trapping of 12 nm Dielectric Spheres Using Double-Nanoholes in a Gold Film. *Nano letters* **11**, 3763–3767 (2011).

[34] Sharifi, Z. *et al.* Isolating and enhancing single-photon emitters for 1550nm quantum light sources using double nanohole optical tweezers. *The Journal of chemical physics* **154**, 184204–184204 (2021).

[35] Ravindranath, A. L., Shariatdoust, M. S., Mathew, S. & Gordon, R. Colloidal lithography double-nanohole optical trapping of nanoparticles and proteins. *Opt. Express* **27**, 16184–16194 (2019).

[36] Chen, Y., Kotnala, A., Yu, L., Zhang, J. & Gordon, R. Wedge and gap plasmonic resonances in double nanoholes. *Opt. Express* **23**, 30227–30236 (2015).

[37] Berg-Sørensen, K. & Flyvbjerg, H. Power spectrum analysis for optical tweezers. *Review of scientific instruments* **75**, 594–612 (2004).

[38] Berg-Sørensen, K., Peterman, E. J. G., Weber, T., Schmidt, C. F. & Flyvbjerg, H. Power spectrum analysis for optical tweezers. II: Laser wavelength dependence of parasitic filtering, and how to achieve high bandwidth. *Review of scientific instruments* **77**, 063106–063106–10 (2006).

[39] Saffman, P. G. Low Reynolds Number Hydrodynamics. By J. HAPPEL & HOWARD BRENNER. Prentice-Hall, 1965. 553 pp. £6. *Journal of Fluid Mechanics* **28**, 826–828 (1967).

[40] Kotnala, A. & Gordon, R. Quantification of High-Efficiency Trapping of Nanoparticles in a Double Nanohole Optical Tweezer. *Nano letters* **14**, 853–856 (2014).

[41] Loiseau, A. *et al.* Silver-Based Plasmonic Nanoparticles for and Their Use in Biosensing. *Biosensors (Basel)* **9**, 78 (2019).

[42] Rivas, L., Sanchez-Cortes, S., Garcia-Ramos, J. & Morcillo, G. Mixed silver/gold colloids: a study of their formation, morphology, and surface-enhanced Raman activity. *Langmuir* **16**, 9722–9728 (2000).

[43] Lee, K.-S. & El-Sayed, M. A. Gold and silver nanoparticles in sensing and imaging: sensitivity of plasmon response to size, shape, and metal composition. *The Journal of Physical Chemistry B* **110**, 19220–19225 (2006).

[44] Yoon, I. *et al.* Single nanowire on a film as an efficient SERS-active platform. *Journal of the American Chemical Society* **131**, 758–762 (2009).

[45] Rycenga, M. *et al.* Probing the surface-enhanced Raman scattering properties of Au–Ag nanocages at two different excitation wavelengths. *Physical Chemistry Chemical Physics* **11**, 5903–5908 (2009).

[46] Hajisalem, G. *et al.* Accessible high-performance double nanohole tweezers. *Opt. Express* **30**, 3760–3769 (2022).

[47] Babaei, E., Wright, D. & Gordon, R. Fringe Dielectrophoresis Nanoaperture Optical Trapping with Order of Magnitude Speed-Up for Unmodified Proteins. *Nano letters* **23**, 2877–2882 (2023).

[48] Ulman, A. Formation and Structure of Self-Assembled Monolayers. *Chemical reviews* **96**, 1533–1554 (1996).

[49] Lu, H. B., Campbell, C. T. & Castner, D. G. Attachment of Functionalized Poly(ethylene glycol) Films to Gold Surfaces. *Langmuir* **16**, 1711–1718 (2000).

[50] Inkpen, M. S. *et al.* Non-chemisorbed gold–sulfur binding prevails in self-assembled monolayers. *Nature chemistry* **11**, 351–358 (2019).

[51] Colorado, R. & Lee, T. Thiol-based Self-assembled Monolayers: Formation and Organization. In Buschow, K. J. *et al.* (eds.) *Encyclopedia of Materials: Science and Technology*, 9332–9344 (Elsevier, Oxford, 2001).

[52] Sigma-Aldrich. QBD10792: m-dPEG4-thiol (2024). URL https://www.sigmaaldrich.com. Accessed: 2024-11-13.

[53] Lotito, V. & Zambelli, T. Playing with sizes and shapes of colloidal particles via dry etching methods. *Advances in Colloid and Interface Science* **299**, 102538 (2022).

[54] Plettl, A. *et al.* Non-Close-Packed Crystals from Self-Assembled Polystyrene Spheres by Isotropic Plasma Etching: Adding Flexibility to Colloid Lithography. *Advanced functional materials* **19**, 3279–3284 (2009).

[55] Doering, R. & Nishi, Y. *Handbook of semiconductor manufacturing technology* (CRC Press, Boca Raton, 2008), 2nd ed. edn.

[56] Lieberman, M. A. M. A. & Lichtenberg, A. J. *Principles of plasma discharges and materials processing* (Wiley, New York, 1994 - 1994).

[57] Hitachi High-Technologies Corporation. *Hitachi: Let's Familiarize Ourselves with the SEM* (2016). Printed in Japan (H) HTD-E167T 2016.3.

[58] Brandon, D., Kaplan, W. D. & Brandon, D. G. *Microstructural Characterization of Materials*. Quantitative software engineering series Microstructural characterization of materials (Wiley, Hoboken, 2008), 2nd ed. edn.

[59] Malagnino, N., Pesce, G., Sasso, A. & Arimondo, E. Measurements of trapping efficiency and stiffness in optical tweezers. *Optics Communications* **214**, 15–24 (2002).

[60] Chen, H. *et al.* Influence of slow light effect on trapping force in optical tweezers. *Opt. Lett.* **47**, 710–713 (2022).

[61] Welch, P. The use of fast Fourier transform for the estimation of power spectra: A method based on time averaging over short, modified periodograms. *IEEE transactions on audio and electroacoustics* **15**, 70–73 (1967).

[62] Jun, Y., Tripathy, S. K., Narayanareddy, B. R., Mattson-Hoss, M. K. & Gross, S. P. Calibration of Optical Tweezers for InVivo Force Measurements: How do Different Approaches Compare? *Biophysical Journal* **107**, 1474–1484 (2014).

[63] Shindel, M. M., Swan, J. W. & Furst, E. M. Calibration of an optical tweezer microrheometer by sequential impulse response. *Rheologica acta* **52**, 455–465 (2013).

[64] Deng, Y., Bechhoefer, J. & Forde, N. R. Brownian motion in a modulated optical trap. *Journal of optics. A, Pure and applied optics* **9**, S256–S263 (2007).

[65] van der Horst, A. & Forde, N. R. Power spectral analysis for optical trap stiffness calibration from high-speed camera position detection with limited bandwidth. *Opt. Express* **18**, 7670–7677 (2010).